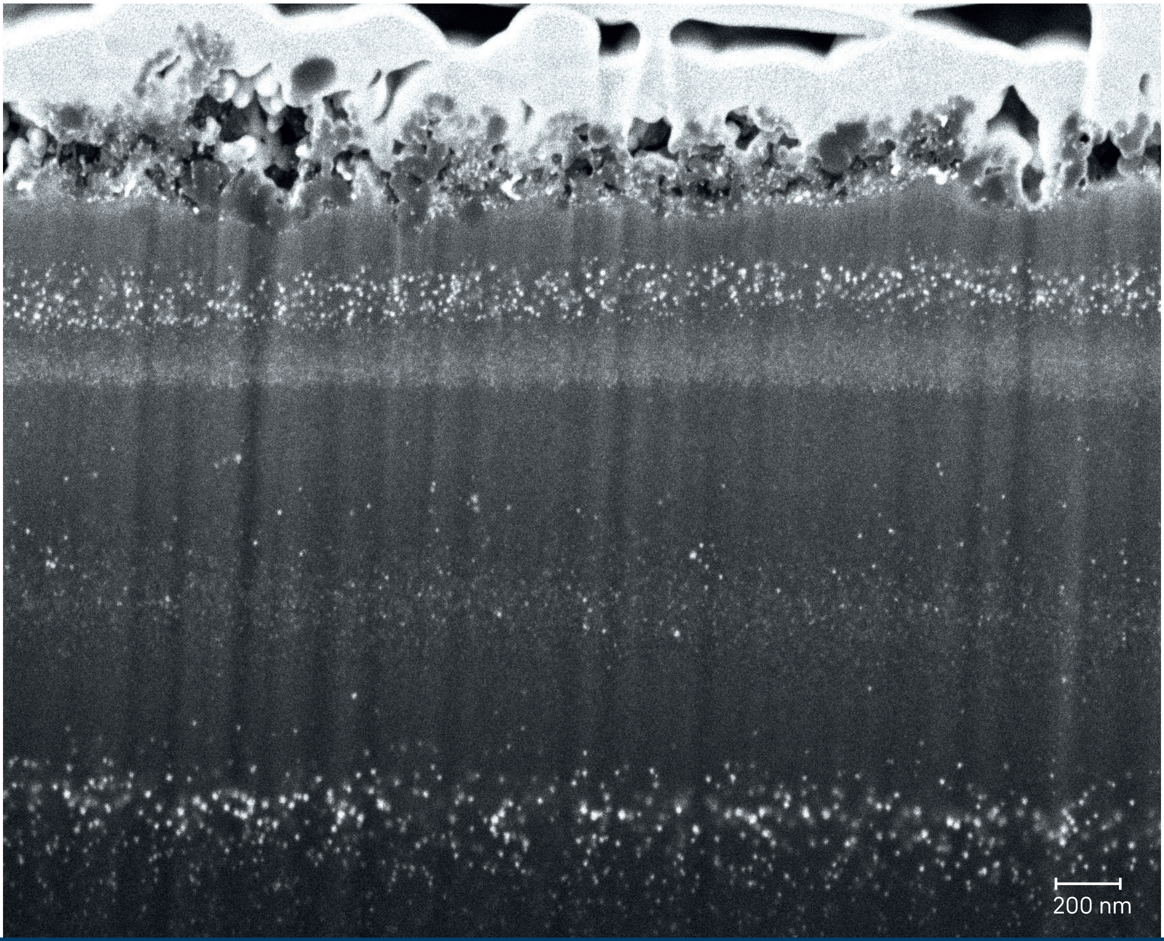

Morphology and Degradation of High Temperature Polymer Electrolyte Fuel Cell Electrodes

Shuai Liu

Energie & Umwelt / Energy & Environment
Band / Volume 479
ISBN 978-3-95806-436-2

Mitglied der Helmholtz-Gemeinschaft

JÜLICH
Forschungszentrum

Schriften des Forschungszentrums Jülich
Reihe Energie & Umwelt / Energy & Environment Band / Volume 479

Forschungszentrum Jülich GmbH
Institut für Energie- und Klimaforschung
Elektrochemische Verfahrenstechnik (IEK-3)

Morphology and Degradation of High Temperature Polymer Electrolyte Fuel Cell Electrodes

Shuai Liu

Schriften des Forschungszentrums Jülich
Reihe Energie & Umwelt / Energy & Environment Band / Volume 479

ISSN 1866-1793 ISBN 978-3-95806-436-2

Bibliografische Information der Deutschen Nationalbibliothek.
Die Deutsche Nationalbibliothek verzeichnet diese Publikation in der
Deutschen Nationalbibliografie; detaillierte Bibliografische Daten
sind im Internet über http://dnb.d-nb.de abrufbar.

Herausgeber und Vertrieb: Forschungszentrum Jülich GmbH
Zentralbibliothek, Verlag
52425 Jülich
Tel.: +49 2461 61-5368
Fax: +49 2461 61-6103
zb-publikation@fz-juelich.de
www.fz-juelich.de/zb

Umschlaggestaltung: Grafische Medien, Forschungszentrum Jülich GmbH

Druck: Grafische Medien, Forschungszentrum Jülich GmbH

Schriften des Forschungszentrums Jülich
Reihe Energie & Umwelt / Energy & Environment, Band / Volume 479

D 82 (Diss. RWTH Aachen University, 2019)

ISSN 1866-1793
ISBN 978-3-95806-436-2

Vollständig frei verfügbar über das Publikationsportal des Forschungszentrums Jülich (JuSER)
unter www.fz-juelich.de/zb/openaccess.

Morphology and Degradation of High Temperature Polymer Electrolyte Fuel Cell Electrodes

Abstract

The polybenzimidazole-based high-temperature polymer electrolyte fuel (HT-PEFC) has become a major topic in the clean energy field in recent years due to the appealing advantages, e.g., improved electrochemical kinetics and enhanced tolerance to carbon monoxide. However, the introduction of phosphoric acid (PA) in the membrane electrode assembly (MEA) leads to several issues, e.g., phosphate contaminations, accelerated Pt corrosion, and PA leaching. What is more, compared to classic PEFCs, the required higher Pt loading is another factor that impedes the commercialization of HT-PEFCs.

The dissertation focuses on the electrochemical processes in the MEA, especially on the cathode side, to investigate the relations among the parameters of the MEA as well as study the degradation mechanism under different operating conditions.

Various types of gas diffusion electrodes are fabricated by using different methods and recipes. Electron characterizations and electrochemical measurements demonstrate that the electrodes with more regular cracks and less PTFE agglomerations perform better. The PTFE binder plays a role in adjusting the PA distribution in the MEA and 10-25 wt.% PTFE is the advised content in the cathode catalyst layer (CCL). In addition, the interactions of another three parameters in MEAs (i.e., Pt loading, thickness of CCL, and PA doping level) are investigated by using the design of experiment (DoE) method. The results propose a direction for the preparation of MEAs: a relatively high PA doping level and a low ratio of Pt/C catalyst are beneficial to improve the Pt utilization efficiency in HT-PEFCs.

The degradation in HT-PEFCs is another emphasis of this dissertation. Five stressors that include high temperature, open circuit voltage, thermal cycling, low-load cycling and high-load cycling are applied to the above optimized MEAs. A Pt band is unexpectedly visualized in the membrane of an MEA only run a standardized break-in procedure by using the focused ion beam milling technique. This concretely proves the corrosive environment in HT-PEFCs. The Pt band formation is explicitly influenced by the operating conditions. The OCV and low-load cycling stressors cause the largest amount of Pt loss into the membrane, indicating that the high potential is the most pronounced factor in Pt corrosion. During the aging tests, the membrane degradation and PA leaching only have minor effects on the performance loss, while the main cause is the degradation of the Pt/C catalyst.

Morphologie und Degradation von Hochtemperatur-Polymerelektrolyt-Brennstoffzellen-Elektroden

Kurzfassung

Hochtemperatur-Polymerelektrolytbrennstoffzellen (HT-PEFC), basierend auf phosphorsäurebeladenen Polybenzimidazol-Membranen, haben in den letzten Jahren eine erhöhte Aufmerksamkeit erlangt. Aufgrund ihrer erhöhten Betriebstemperatur von typischerweise 160°C haben sie eine hohe Toleranz gegenüber Kohlenmonoxid. Darüber hinaus ist ein komplexes Wassermanagement im Vergleich zu Niedertemperatur-Polymerelektrolytbrennstoffzellen (NT-PEFC) nicht notwendig. Weiterhin gestaltet sich die Kühlung aufgrund der hohen Temperaturdifferenz zwischen Zelle und Umgebung vergleichsweise einfach. Aus der Phosphorsäure in der Zelle resultieren jedoch einige Nachteile wie beispielsweise Phosphatverunreinigungen, beschleunigte Pt-Korrosion und Auswaschung der Phosphorsäure aus der Membran. Darüber hinaus ist im Vergleich zu NT-PEFCs die erforderliche höhere Pt-Beladung ein Faktor, der die Kommerzialisierung von HT-PEFCs behindert.

Die hier vorliegende Dissertation befasst sich mit elektrochemischen Prozessen in der Membran-Elektroden-Einheit (MEA). Der Einfluss der Elektrodenmorphologie, insbesondere der kathodenseitigen Elektrode, auf das Leistungs- und Alterungsverhalten steht im Vordergrund.

Gasdiffusionselektroden werden unter Verwendung verschiedener Verfahren und Rezepturen hergestellt. Elektrochemische Messungen zeigen, dass die Elektroden mit regelmäßigeren Rissen und geringer PTFE-Agglomerationen zu einer hohen Zellleistung führen. PTFE beeinflusst die Phosphorsäureverteilung in den Elektroden und es stellt sich heraus, dass 10-25 Gew .-% PTFE der empfohlene PTFE-Gehalt in der Kathodenkatalysatorschicht ist. Zusätzlich werden Einflüsse von drei weiteren MEA Herstellparametern auf das Leistungsverhalten von Zellen unter Verwendung der Design-of-Experiment (DoE) -Methode untersucht. Konkret sind diese Parameter die Pt-Beladung, die Dicke der Katalysatorschicht und die Phosphorsäurebeladung der MEA. Beispielsweise sind ein hoher Phosphorsäure-Beladungsgrad und ein niedriges von Pt / C Verhältnis des geträgerten Katalysators vorteilhaft, um die Pt-Nutzung in HT-PEFCs zu erhöhen.

Das HT-PEFC Alterungsverhalten ist ein weiterer Schwerpunkt dieser Dissertation. Erhöhte Betriebstemperatur, Betrieb ohne Last (OCV), periodischer Temperaturwechsel und Lastwechsel bei niedriger beziehungsweise bei hoher Last, werden systematisch auf ihren Alterungseinfluss untersucht. Hierbei zeigt sich auch, dass in der Membran ein Pt-Band sichtbar wird. Zellmessungen und anschließende FIB- SEM-Analysen der MEA zeigen, dass sowohl die Position als auch die Intensität des Pt-Bandes von den Betriebsbedingungen abhängt. Der OCV-Betrieb und die Wechselbeanspruchungen bei niedriger Last verursachen den größten Pt-Verlust in den Elektroden. Gleichzeitig sind die höchsten Pt-Konzentrationen in der Membran beobachtbar. Dies weist darauf hin, dass das hohe Potenzial der dominierende Faktor für die Pt-Korrosion ist. Membrandegradation beziehungsweise Phosphorsäureverlust haben nur geringe Auswirkungen auf das Leistungsverhalten. Die Hauptdegradationsursache ist in allen untersuchten Fällen dem Katalysator zuzuschreiben.

Contents

1. Introduction

1.1. Working principle of HT-PEFCs

High-temperature polymer electrolyte fuel cells (HT-PEFCs) are operated from 140 ℃ up to 200 ℃ [1]. Due to the enhanced temperatures, HT-PEFCs exhibit improved tolerance to impurities, easier heat rejection and easier water management, compared to classic polymer electrolyte fuel cells (usually below 80 ℃) [2-4]. As a promising fuel cell generation, it is of great significance to investigate and develop the technology of HT-PEFCs.

The schematic working principles are shown in Figure 1.1A. The core part of HT-PEFCs is the membrane electrode assembly (MEA), including an anode, membrane, and cathode. Hydrogen is fed into the anode side and air/oxygen is supplied into the cathode side. The anode and cathode are separated by a proton exchange membrane (PBI membrane) that is doped with phosphoric acid as the electrolyte. By using platinum at both electrodes as the catalyst, the chemical energy is converted into electrical energy.

The reactions occurring at the electrodes are shown below:

Anode:

$$H_2 \rightarrow 2H^+ + 2e^- \tag{1.1}$$

Cathode:

$$2H^+ + \tfrac{1}{2}O_2 + 2e^- \rightarrow H_2O\ (g) \tag{1.2}$$

Overall:

$$H_2 + \frac{1}{2}O_2 \rightarrow H_2O\ (g) \tag{1.3}$$

At the anode, hydrogen is oxidized to protons on the surface of the Pt/C catalyst. Then, the produced protons transfer through the PBI membrane, with the chemical structure of PBI shown on the right side of Figure 1.1A [5]. It is widely accepted that the Grotthuss mechanism is the main mechanism for proton transport. The PBI polymer chain traps PA molecules that are bonded with the nitrogen atoms. Also, during the doping process, additional PA molecules are absorbed in the PBI membrane as free acid. The protons transfer through the membrane by the formation and cleavage of bonds with PA, which is called as the hopping mechanism [5-7]. After the transport process, the oxygen reduction reaction (ORR) occurs at the cathode catalyst layer. As the ORR reaction is orders of magnitude slower than the hydrogen oxidation reaction, the cathode side determines the overall cell performance [8]. Figure 1.1B shows a cross-sectional SEM image of a cathode sample, which consists of three parts, i.e., the catalyst layer, gas diffusion layer (GDL), and microporous layer (MPL). The oxygen passes through the GDL and MPL, and reaches the cathode catalyst layer. The protons transfer through the PA doped PBI membrane to the cathode side. Electrons produced at the anode pass through an outer route of a load and flow back to the cathode. The ORR process takes place at the triple phase boundary (TPB), which is formed by three phases: catalysts, ion conductors, and gaseous reactants. The amount and condition of TPB determine the efficiency of the cathodes and performance of HT-PEFCs [9]. The GDL serves as a gas diffusion media and support structure for MEAs, which mainly consists of carbon cloths and non-wetting polymers such as polytetrafluoroethylene (PTFE) [10]. In classic PEFCs, Gostick et al. reported that water percolation through the MPL improves water management in MEAs [11]. In HT-PEFCs, the water management problem has been simplified due to the elevated temperatures; hence, the role of the MPL is unclear and remains still an important research topic. Lobato et al. reported that the MPL improves the adhesion of the electrode different layers and increases the electrochemically active surface area [12]. Further investigation and optimization of the MPL are important to improve the performance of HT-PEFCs.

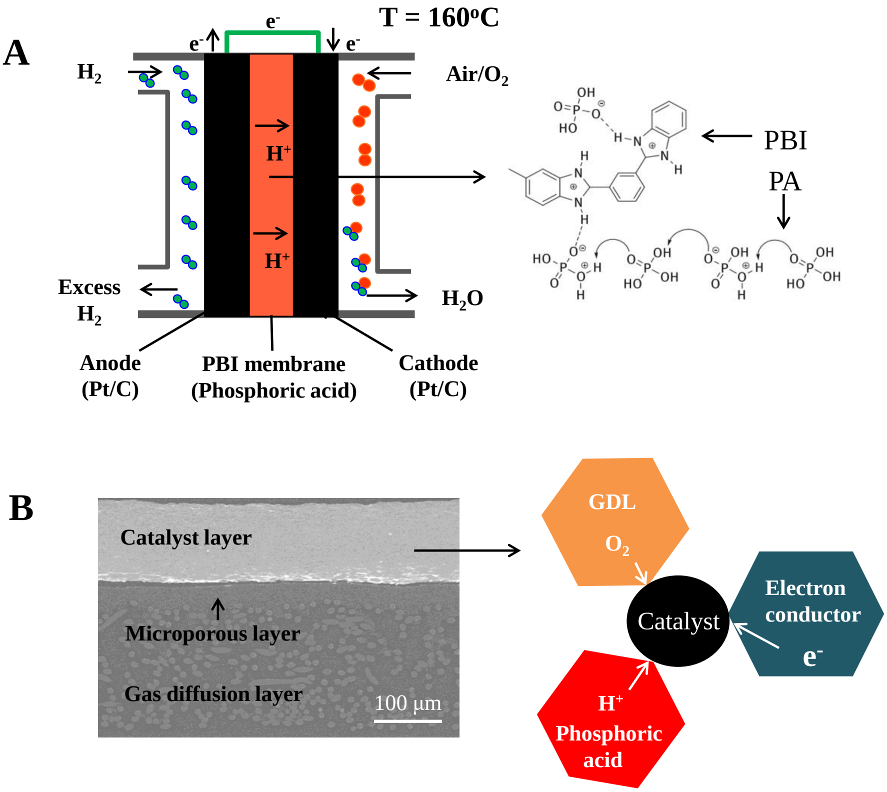

Figure 1.1: (A) Schematic working principle of HT-PEFCs (left) and chemical structure of the repeating units of PBI [5] (right); (B) cross-sectional SEM image of a cathode sample.

1.2. Literature review

For a two-step reaction that takes place on an adsorbed intermediate, like the hydrogen oxidation reaction or oxygen reduction reaction, the adsorption energy should not be too high or too low. If the energy is too high, the reaction rate is slow and limited. Also, the low adsorption energy can lead to a slow reaction rate according to the Sabatier's principle [13, 14]. Trassati's volcano plots provide information about the hydrogen evolution and oxygen reduction reactions in acid solutions on different substrates, and Pt exhibits a proper adsorption energy and the maximum exchange current density for the reactions that occur on both sides of HT-PEFCs [14, 15]. Based on the electrochemical principle, Pt is widely applied as the catalyst at both anodes and cathodes. However, the cost of Pt catalysts is the main hindrance to the commercial production of PEFC vehicles, which accounts for more than half of the total stack [16].

To reduce the cost and improve the activity of catalysts to the ORR in HT-PEFCs, non-noble metal and platinum alloys catalysts have been studied by several authors. Schenk et al. applied platinum-cobalt catalysts (Pt-Co) to HT-PEFCs, and the results show that the Pt-Co/C based HT-PEFCs exhibit an equal performance to a commercially available Pt/C based HT-PEFC during 600 h operation at a constant load [17]. Li et al. reported a nonprecious metal catalyst that is synthesized from polyaniline (PANI), iron, and carbon. The prepared Fe-based catalysts can tolerate the poisoning of phosphate ions and show better performance to ORR [18]. Parrondo et al. prepared platinum supported over tin oxide and Vulcan carbon (Pt/SnOx/C) catalysts and used them for HT-PEFCs. The authors state that the 7 wt.% SnO in $Pt/SnO_2/C$ catalyst demonstrates the highest catalytic activities towards ORR, with the HT-PEFC's voltage of 0.58 V at a current density of 200 mA cm^{-2} [19]. Wang et al. synthesized Pd-composite $Nb_{0.06}Ti_{0.94}O_2$ material and employed it as the catalyst supports for Pt-Pd alloy catalysts. The novel catalyst exhibits a higher activity towards ORR, but lower electrochemical stability compared to the commercial Pt/C catalyst [20].

Optimizations of the electrode morphology, especially for the cathode catalyst layer (CCL), by using different preparation methods, supports, binders, etc., are effective ways to reduce the Pt loading and improve HT-PEFCs' performance. Martin et al. applied the electrospraying deposition technique to prepare electrodes with a Pt loading of only 0.1 mg cm^{-2}, which yield a maximum performance of 420 mW cm^{-2} in HT-PEFCs [21]. Felix et al. reported the gas diffusion electrodes fabricated by an electrophoretic deposition method, and the prepared electrodes show excellent performance in HT-PEFCs, with a peak power increase of about 73% compared to the electrode prepared by a hand sprayed method [22]. A well-designed support can help disperse Pt in the catalyst layer, thus reduce electrical resistance and improve HT-PEFCs' performance. Du et al. prepared a novel CNT/CC (carbon nanotubes directly grown on a carbon cloth) support. Compared to the normal carbon support, the new support significantly improves the maximum power density from 468 mW cm^{-2} to 643 mW cm^{-2} in HT-PEFCs with a lower Pt loading [23]. Huang et al. reported a novel TiO_2-supported Pt electrocatalyst in PEFCs, which shows enhanced stability due to lower corrosion resistance of the TiO_2 support and improved performance due to the low mass transport resistance in the CCL [24].

What is more, binders are normally added to the catalyst layer to improve the electrode structure and performance. In the early HT-PEFCs, polybenzimidazole (PBI) as an amorphous basic polymer is the most commonly used binder in the catalyst layer due to the high thermal stability and easy reaction with PA [25, 26]. However, additional PBI polymer in the catalyst layer could cause an increased mass transport resistance due to the film formed on the Pt/C catalyst and the PA flooding effect [27]. Yusof et al. reported that electrodes with excessive PBI ionomer exhibit lower power density, as a large amount of polymer is covered on the catalyst particle [28]. Su et al. compared the performance of gas diffusion electrodes (GDEs) with different kinds of binders, including PBI, polytetrafluoroethylene (PTFE), polyvinylidene difluoride (PVDF), and Nafion [29]. The results demonstrate that the GDEs with PTFE and PVDF have better electrochemical performance and stability. The high hydrophobicity is one of the most important properties of PTFE, which obviously affects HT-PEFCs' performance from three aspects: 1) PA flooding effect is alleviated, thus leading to an enhancement of gas transport [1, 30]; 2) there is no interaction with the phosphoric acid, resulting in a high kinetic overpotential [31]; 3) there is significant impacts on PA leaching of MEAs [32]. Another influential property of PTFE is the non-conductivity, which 1) decreases the electronic conductivity of GDEs; 2) blocks the active sites and therefore decreases the active area of the catalyst particles [33]; affects the mechanical stability of GDEs [34]. Su et al. fabricated a novel GDE by using PTFE and PVDF together in the catalyst layer [35]. PVDF with good affinity is added in the inner catalyst layer to enhance the electrode kinetics and PTFE is added in the second layer of the catalyst layer to reduce the mass transport resistance and PA leaching [35]. Moreover, the content of PTFE has a strong impact on the performance of GDEs. Jeong et al. reported that GDEs with a content of 20 wt.% PTFE have optimal pore structures and exhibit the best electrochemical performance [36]. Avcioglu et al. noted that even low amount of PTFE in GDEs could reduce the Pt utilization and lead to lower performance [37]. Martin et al. reported that the absence of PTFE is beneficial for HT-PEFCs' performance, particularly under high load operations [38].

As mentioned above, compared to classic PEFCs, HT-PEFCs exhibit an enhanced rate of degradation in MEAs. Until now, massive works have reported to focus on the degradation of HT-PEFCs, including catalyst degradation [39-41], carbon corrosion [41-43], PA leaching [44-46], and membrane degradation [47, 48].

Catalyst degradation is one of the most important issues due to the higher operating temperatures and more acidic environment [49]. Meyers et al. proposed a three-step dissolution model based on the oxidation and dissolution of the Pt/C catalyst in PEFCs [50]:

Pt dissolution:

$$\mathrm{Pt} = \mathrm{Pt}^{2+} + 2e^{-} \tag{1.4}$$

Pt oxide film formation:

$$\mathrm{Pt} + \mathrm{H_2O} = \mathrm{PtO} + 2\mathrm{H}^{+} + 2e^{-} \tag{1.5}$$

Pt oxide dissolution:

$$\mathrm{PtO} + 2\mathrm{H}^{+} = \mathrm{Pt}^{2+} + \mathrm{H_2O} \tag{1.6}$$

The formed Pt ions could 1) re-deposit onto large Pt particles (Ostwald ripening) [51]; 2) migrate into the membrane due to a concentration difference, resulting in a Pt band [52]. The Pt precipitation in the membrane has been widely studied in classic PEFCs. Yoda et al. observed Pt band in the Nafion®112 electrolyte membrane after a daily start and stop operation [53]. Bi et al. reported the Pt band formation in the Nafion membrane after a potential-cycling test under hydrogen/air conditions [54]. Ohma et al. found that membrane degradation is enhanced by the Pt band formation [52]. Macauley et al. reported a contradictory result, which shows that the formation of Pt band enhances the membrane durability in PEFCs [55]. Zhang et al. investigated the Pt precipitation at open-circuit voltage conditions, and proposed a model to describe the location of the Pt band in the Nafion membrane. The equation is shown below [56]:

$$\delta_{Pt} = \frac{K_{H_2} P_{H_2} \delta_m}{K_{H_2} P_{H_2} + 2K_{O_2} P_{O_2}} \tag{1.7}$$

where δ_{Pt} is the location of the Pt band, δ_m the thickness of the membrane, K the membrane gas permeability, and P the gas partial pressure.

In HT-PEFCs, the Pt migration and precipitation have not been widely studied. In 2016, Rau et al. firstly reported the Pt band formation in the PBI-based membrane [57]. Hengge et al. observed a band of Pt and Pt/Ru nanoparticles in the PBI membrane after a long-term operation in HT-PEFCs; the authors state that the Pt band may benefit HT-PEFCs' performance by acting as an active barrier for cross-leaking H_2 and O_2 [58]. In our previous work, a Pt band was visualized in the PBI-based membrane, with the MEA initially activated by a standardized break-in procedure (run at 200 mA cm^{-2} for 70 h), indicating the accelerated degradation rate of the cathode catalyst layer in HT-PEFCs [59].

The membrane degradation is considered to be closely related to the formation of peroxide (H_2O_2) at both the anode and cathode. The formed H_2O_2 particles diffuse into the membrane and further consumed by the Fenton reactions, leading to the formation of intermediate radical species that are detrimental to the membrane [60]. The reaction equations are shown below:

Anode: Chen et al. [61] and Yu et al. [62]

$$H_2 \rightleftarrows 2H\bullet \tag{1.8}$$

$$H\bullet + O_{2\ (\mathrm{permeation})} \leftrightarrows HO_2\bullet \tag{1.9}$$

$$HO_2\bullet + e^- + H^+ \rightarrow H_2O_2 \tag{1.10}$$

Cathode: Gubler et al. [65]

$$O_2 + 2H^+ + 2e^- = H_2O_2\ (E_0 = 0.672\ \mathrm{V}) \tag{1.11}$$

Ohguri et al. provided experimental data, presenting that the amount of radicals formed in the anodes is almost twice that in the cathodes of Nafion-based PEFCs [63]. Furthermore, it is reported that the membrane degradation starts at the electrode/membrane interface and then continues towards the center [48, 61].

During the operations of HT-PEFCs, various operating conditions, such as constant loads, load cycling, OCV, thermal cycling, etc., are required to meet different operational requirements, leading to different degradation behaviors in HT-PEFCs. Oono et al. operated HT-PEFCs at 200 mA cm^{-2} for periods of up to17,860 h. The results show that the membrane thinning, catalyst degradation and carbon corrosion occur during the durability test [64]. Søndergaard et al. run HT-PEFCs at 160 ℃ under a constant load of 200 mA cm^{-2} for periods from 1000 h to 13,000 h, with the degradation rate from 1.4-4.6 mV h^{-1} [65]. Halter et al. found that the phosphoric acid electrolyte migrates towards the anode at high current densities (e.g., 800 mA cm^{-2}), causing the flooding of the anode and the de-flooding occurs at low current densities (e.g., 200 mA cm^{-2}) [66]. Chen et al. reported that the dehydration transformation from H_3PO_4 to $H_4P_2O_7$ starts at around 130-140 ℃ [67]. Galbiati et al. studied the MEA degradation at a high temperature of 180 ℃, which shows a higher degradation rate compared to the MEA operated at 160 ℃, with the degradation rate increasing from around 8 mV h^{-1} to around 19 mV h^{-1} [68]. Load cycling as an effective stressor is studied by a large number of works. Pilinski et al. reported that the load cycling at high current densities shows a high-performance loss of 62 μV h^{-1} compared to 14 μV h^{-1} under the constant load operation [69]. Thomas et al. compared the durability of HT-PEFCs using the constant load condition and different load cycling modes [70]. The results demonstrate that the load cycling operation with a relaxation time of 2 min is beneficial for the HT-PEFC durability, with the degradation rate 1.5 times lower than that of the cell operated under the constant load condition (36 μV h^{-1} vs. 57 μV h^{-1}) [70]. J.A. Kerres found that load cycling tests could lead to the swelling and thinning of the PBI membrane, which impose mechanical stress on the membrane [71]. Open circuit voltage (OCV) hold operation is a commonly used stressor to accelerate durability tests. Yu el al. noted that the OCV and high load conditions can cause carbon corrosion [72]. Modestov et al. reported that substantial corrosion of the carbon support occur at OCV due to the high potential, while it becomes negligible under load operations [73]. Zhao et al. operated HT-PEFCs under OCV condition by using three types of composite membranes. The results show that the hydrogen crossover increases as the membrane thickness decreases and catalyst degradation is observed after the OCV hold tests [74]. These researches present different degradation behaviors under various operating conditions. However, it is hard to compare the degradation rates because different components and materials are used. It is still of great significance to do more detailed work under different operating conditions using identical HT-PEFCs.

1.3. Fundamentals of HT-PEFCs

Figure 1.2A shows the polarization curve for a standard HT-PEFC operated at 160℃, with H_2 and air purged in the anode and cathode, respectively. Generally, the cell's voltage can be described by Equation (1.12) [75]:

$$E_{cell} = E_{rev\,(P_{H_2},P_{O_2},T)} - \eta_{act} - \eta_{ohm} - \eta_{conc} \tag{1.12}$$

where E_{cell} is the test cell voltage, η_{act} the activation overpotential, η_{ohm} the ohmic overpotential and η_{conc} the concentration overpotential. E_{rev} is the reversible potential calculated from the Nernst equation (1.13):

$$E_{rev\,(P_{H_2},P_{O_2},T)} = \frac{\triangle H - T\triangle S}{nF} + \frac{RT}{nF} \cdot ln\left(\frac{P_{H_2}P_{O_2}^{0.5}}{P_{H2O}}\right) \tag{1.13}$$

where $\triangle H$ is the enthalpy change of the reaction, $\triangle S$ the entropy change, and T the operating temperature, P_{H2}, P_{O2}, P_{H2O} the hydrogen, oxygen, and water vapor pressures over the atmospheric pressure, respectively, R the universal gas constant, F the Faraday constant, and n the number of electrons involved in the charge transfer process.

In the activation-loss region of the UI curve ($j < 0.1$ A cm^{-2}), the potential exhibits exponential decay with increasing current density [19, 76]. The Butler-Volmer equation is used to study the voltage degradation in this region because η_{conc} can be neglected, with the equation shown below [77, 78]:

$$j = j_0[e^{\frac{\alpha nF\eta}{RT}} - e^{-\frac{(1-\alpha)nF\eta}{RT}}] \tag{1.14}$$

where j_0 is the exchange current density, n the number of electrons, η the overpotential, and α the charge transfer coefficient.

When the η is high, the reverse reaction of Equation (1.14) is ignored [79, 80]. Therefore, the Equation 1.14 can be simplified as:

$$j = j_0 e^{\frac{\alpha nF\eta}{RT}} \tag{1.15}$$

The simplified equation can be transferred to the Tafel equation:

$$\eta = a + b\log j \tag{1.16}$$

where a is a constant and b the so-called Tafel slope.

The Tafel slope is an important indicator for the ORR, and a lower Tafel slope means higher kinetics of the reaction on the cathode side [81]. η_{act} is determined by the Tafel equation. By using the electrochemical impedance spectroscopy (EIS) technique, η_{ohm} can be measured. Finally, η_{conc} is determined by Equation (1.12). Figure 1.2B shows the calculated η_{act}, η_{ohm} and η_{conc} of the HT-PEFC. The slope of a tangent to the curve represents the corresponding resistance. It can be seen that the charge transfer resistance (from η_{act}) decreases as the current density goes higher. This can be explained by the increased production of water at higher current densities, increasing the solubility of oxygen in the PA/water mixture, thus leading to an enhanced j_0 [82]. At low values of the overpotential (η < 100 mV), Equation (1.14) can be simplified to Equation (1.17) and j_0 is defined by Equation (1.18) [80, 83]:

$$R_{ct} = \frac{RT}{nFj_0} \tag{1.17}$$

$$j_0 = nFAk^0C \tag{1.18}$$

where A is the electrochemically active surface area, C the concentration of the redox species, and k^0 the standard homogeneous rate constant.

The increased mass transport resistance (R_m) at high current densities can be explained by the rapidly consumed reactants that cause concentration gradients [84].

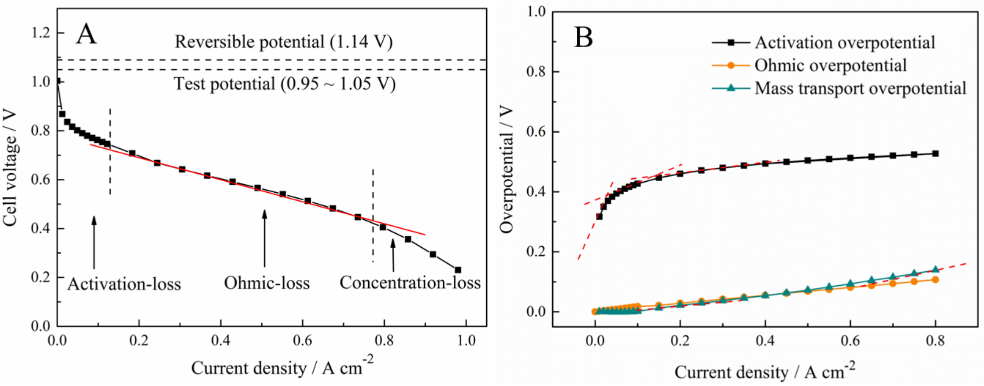

Figure 1.2: (A) A sample of polarization curve for an HT-PEFC operated at 160℃ with stoichiometry: H_2/Air = 2/2; (B) the calculated η_{act}, η_{ohm} and η_{conc} of the HT-PEFC based on Equation (1.12).

Electrochemical impedance microscopy (EIS) is a powerful tool for in-situ characterization. During EIS tests, the cathode is normally served as the working electrode and anode is functioned as a quasi-reference electrode. Firstly, a small amplitude AC sinusoidal potential wave is applied to HT-PEFCs with different frequencies, as shown in the equations below [85]:

$$V(t) = V_m \sin(\omega t + \varphi) \tag{1.19}$$

$$I(t) = I_m \sin(\omega t + \theta) \tag{1.20}$$

where $V(t)$ and $I(t)$ are the instantaneous voltage and current values at the instant of time, V_m and I_m are the amplitude values of the sinusoidal waves, ω is the angular frequency, t the time, and θ the phase angle.

Then the ratio of the AC potential to the current signal is measured and the impedance is defined in the complex plane using Euler's Function as described below:

$$Z = \frac{V\ (t)}{I\ (t)} = \frac{V_m e^{i\varphi}}{I_m e^{i\theta}} \tag{1.21}$$

where $i = \sqrt{-1}$.

Based on Equation (1.21), the AC impedance of a resistor is defined as:

$$Z_R = R \tag{1.22}$$

A capacitor is defined as:

$$Z_C = \frac{1}{i\omega C} \tag{1.23}$$

Figure 1.3 shows the Nyquist plot of an HT-PEFC and the corresponding equivalent circuit used for the fitting procedure. The graph is always recorded in the frequency range of 100 mHz to 100 kHz, with an amplitude of 10 mV. The inductive element (L) models the inductive effects (e.g., cable noise) in the high frequencies, followed by a resistor (R_Ω) that accounts for the ohmic resistance of the HT-PEFC. R_p is an element in the THALES software, which represents the cathode protonic resistance in the CCL. The two semi arcs in the Nyquist plot are related to the cathode ORR reaction, which represent the cathode charge transfer and oxygen diffusion processes, respectively. The resistor (R_{ct}) models the charge transfer resistance and the Nernst diffusion element (Z_N) models the mass transport (R_m) process. The Z_N is defined by the equations below [86]:

$$z_N(j\omega) = \frac{W}{\sqrt{K_N}} \times \frac{tanh\sqrt{i\omega/K_N}}{\sqrt{i\omega/K_N}} \tag{1.24}$$

$$R_m = Z_N(0) = \lim_{\omega \to 0} Z_N(j\omega) \tag{1.25}$$

where *W* is the Warburg impedance, k_N the diffusion coefficient, ω the angular frequency, and $i = \sqrt{-1}$.

The constant phase element (CPE_{dl}) simulates the double layer capacitance (C_{dl}) of the CCL, which is calculated using the equation below [87]:

$$C_{dl} = R^{\frac{1-n}{n}} \times Q^{\frac{1}{n}} \tag{1.26}$$

where *Q* is the pre-factor of the CPE and *n* the exponent.

The total resistance (R_{total}) is calculated by Equation (1.27):

$$R_{total} = R_{\Omega} + R_{ct} + \frac{1}{3}R_p + R_m \tag{1.27}$$

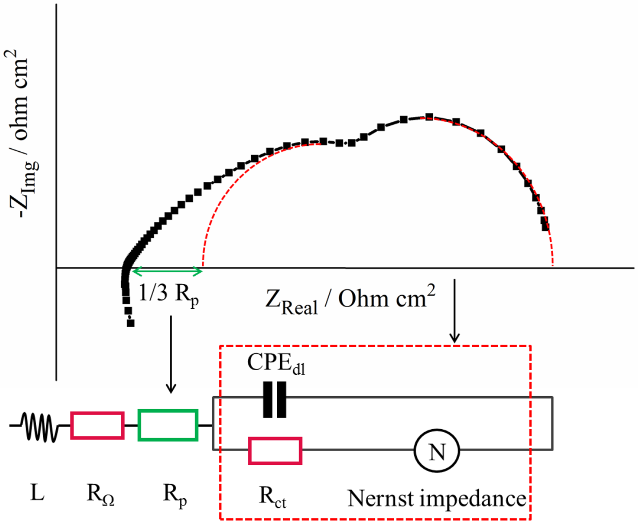

Figure 1.3: Nyquist plot features of an HT-PEFC and the corresponding equivalent circuit used for the fitting procedure.

Cyclic voltammetry (CV) is a commonly used technique to evaluate the electrochemically active surface area (*ECSA*) in HT-PEFCs. By purging nitrogen instead of air/oxygen in the cathode, the cathode *ECSA* can be calculated based on the hydrogen desorption region (red square), as shown in Figure 1.4A. The ECSA is calculated by the equation below [88]:

$$ECSA(m^2 g^{-1}\ Pt) \ = \frac{Q(C\ cm^{-2})}{210 \times 10^4\ (\mu C\ m^{-2}\ Pt) \times Pt\ loading\ (mg\ cm^{-2})} \tag{1.28}$$

where Q is the hydrogen desorption charge on the cathode; 210 × 10^{-4} μC m^{-2} is the amount of charge required to reduce monolayer hydrogen on smooth Pt in aqueous electrolytes.

We can see in the CV plot that only one single hydrogen desorption peak is observed, in contrast to LT-PEFC where two peaks are normally observed [89]. This can be explained by the significant H_3PO_4 anion coverage of the Pt nanoparticles [90], leading to suppression of the hydrogen desorption peak at around 0.23 V [91]. What is more, at high temperatures, especially higher than 100 °C, high faradaic hydrogen evolution reaction currents are superimposing the pseudocapacitive hydrogen underpotential deposition currents [92]. Those reasons lead to inaccurate and smaller ECSA compared to that in classic PEFCs. The tested ECSA in HT-PEFCs is normally about 20 m^2 g^{-1}, compared to 50 m^2 g^{-1} in classic PEFCs [93].

Figure 1.4B shows the linear sweep voltammetry (LSV) curve, which is used to evaluate the hydrogen crossover current and internal short circuit resistance ($R_{internal\ short}$). The measured current above zero is the oxidation current, which is the sum of the hydrogen limiting crossover current and a superimposed internal short circuit current caused by the passage of electrons through the membrane [59, 94]. The hydrogen crossover current is limited by the rate of hydrogen molecular permeation through the membrane, while the current rises linearly as the applied voltage increases due to the internal short circuit in HT-PEFCs. The $R_{internal\ short}$ is quantified by calculating the reciprocal of the slope in the linear region of 0.35-0.45 V [59]. The limiting crossover current density is calculated by Equation (1.29):

$$j_l = \frac{I}{A} - j_{internal\ short} = \frac{I}{A} - \frac{U_{cell}}{AR_{internal\ short}} \tag{1.29}$$

where j_l is the limiting crossover current density, I the measured current, A the electrode area, $j_{internal\ short}$ the internal short circuit current density, $R_{internal\ short}$ the internal short resistance, and U_{cell} the applied voltage.

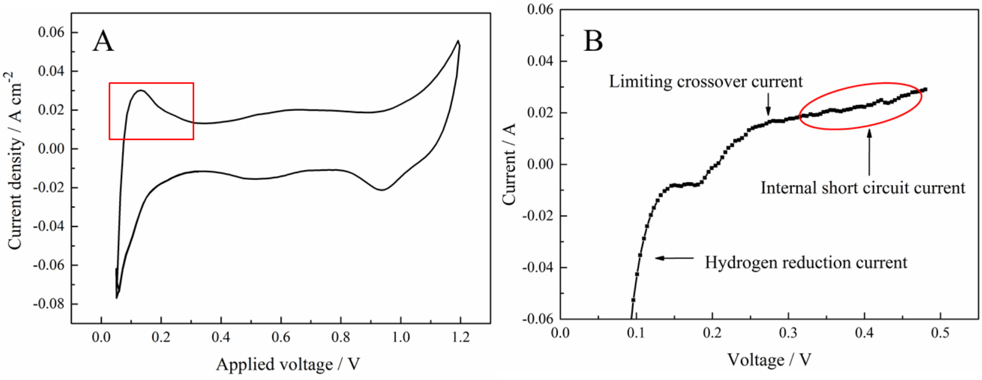

Figure 1.4: Cathode (A) CV and (B) LSV plots of an HT-PEFC at 160 ℃ with N_2 and H_2 purged in the cathode and anode, respectively.

1.4. Motivation and research goals

The membrane electrode assembly (MEA) is the core part of HT-PEFCs. Compared to classic PEFCs, the elevated operating temperatures and the introduced phosphoric acid bring both rewards and challenges to the HT-PEFC. The advantages have been mentioned above, and the challenges are identified as follows:

- Low HT-PEFCs’ performance
- Low catalyst utilization efficiency
- Enhanced catalyst degradation

This dissertation focuses on the MEA, especially for the CCL. Experimental studies concentrate on the preparation of various cathodes to better understand the impact of various factors on electrode performance. Durability tests are carried out to investigate the degradation mechanism of the MEA under different operating conditions. The main research goals are summarized below:

- Investigating the effect of cathode morphologies on HT-PEFCs’ performance
- Better understanding the correlations of the MEA parameters to improve the Pt utilization efficiency
- Investigating the Pt precipitation phenomenon in the PBI-based membrane and discussing the catalyst degradation mechanism
- Comparing the degradation behaviors under various operating conditions

2. Experimental setup and procedures

2.1. HT-PEFC preparation

2.1.1. Preparation of gas diffusion electrodes

The gas diffusion electrodes (GDEs) were prepared by a doctor blade method and a spraying method. Photographs of the devices are shown in Figure 2.1.

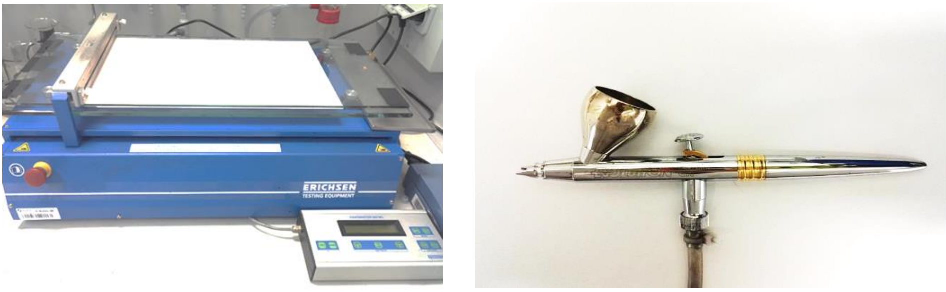

Figure 2.1: Photographs of the coating machine for doctor blade process (left) and airbrush for spraying technique (right).

The preparation process of the standard GDEs by the doctor blade method is as follows: Firstly, 1 g of a carbon-supported Pt catalyst (20 wt.% Pt, Alfa Aesar) was mixed with 3.0 mL deionized water and 19.5 mL solvent (Propan-1-ol: Propan-2-ol (1:1)), and then the mixture was sonicated for 4 min. Secondly, 744 µL PTFE (40 wt.% content in the CCL) purchased from Dyneon TF5032Z was added to the ink, which was sonicated for 30 min to finely disperse the Pt/C catalyst and binder in the solvent. Thirdly, the ink was coated on a commercially-available GDL, with a microporous layer on one side (Freudenberg H2315C2) by a blade with a speed of 7.5 mm s^{-1}. Finally, the prepared GDEs were dried in a fume hood overnight and cut into required size before use. Figure 2.2A shows the photograph and the corresponding Pt loadings of the prepared

GDEs by the doctor blade method. It can be seen that the Pt loading of the GDEs decreases in the blade moving direction. The first two GDEs were chosen to be used in HT-PEFCs to eliminate the effect of Pt loading difference on cells' performance. The GDEs with different thickness, Pt loadings and binder contents were prepared by using different spacers and different recipes of the ink. The anode Pt loading is maintained at 0.6 ± 0.05 mg cm^{-2} with the thickness of 60 ± 10 μm. The standard cathode Pt loading is 1.0 ± 0.05 mg cm^{-2} with the thickness of 120 ± 10 μm and the parameters of various cathodes will be shown in the following chapters. For the GDEs prepared by the spraying method, different recipes were used with more solvent (22.80 mL) in the ink. The catalyst ink was sprayed onto the GDL layer by layer until the Pt loading is within the desired range.

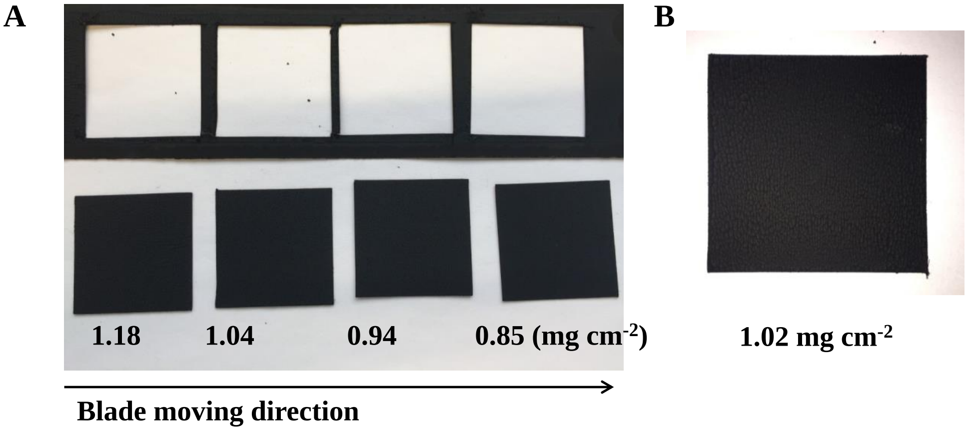

Figure 2.2: Photographs and the corresponding Pt loadings of the GDEs prepared by: (A) doctor blade method; and (B) airbrush spraying method.

2.1.2. Membrane doping

The membrane used in this work was cross-linked AM-55 membrane purchased from FuMA-Tech GmbH, Germany. Before a doping process, the membrane was dried in an oven at 150 ℃ for 30 mins and weighed as M_0. Then, the membrane was immersed in the 85 wt.% phosphoric acid (PA) at 110 ℃ for around 18h under magnetic stirring. After that, the doped membrane was flattened on a table to remove the excess PA on the surface. The surface area (A) of the doped membrane was measured and weighed as M_1. The final PA doping level (PADL) was kept at 15 ± 0.5 mg cm^{-2}, which was calculated using Equation (2.1):

$$\mathrm{PADL} = (M_1 - M_0) / A \tag{2.1}$$

2.1.3. HT-PEFCs single cell assembling

Figure 2.3 shows a photograph of HT-PEFCs single cell in an exploded view. The outermost components 1 in the figure are endplates made of stainless steel with gas inlet and outlet on them. Next to the endplates are expanded graphite (Sigraflex ®) used for sealing and conducting. Components 3 are three channel serpentine flow fields made of graphite with a width of 1 mm for the ribs and channels. The home-made MEA (component 4) was made by sandwiching the membrane between the anode and cathode. Outside of the MEA are perfluoroalkoxy gaskets, which are used for gas sealing and as a hard stop to achieve 15-20% MEA compression. During the HT-PEFCs assembly process, the torque applied to each bolt is typically 6 Nm to 8 Nm to prevent gas leakage. Then, the HT-PEFCs went through a gas leakage test: 1) purging nitrogen in both sides until the pressure is around 300 mbar and then closing the inlet and outlet; 2) recording the pressure drop within one minute. The gas sealing of the HT-PEFCs meets the requirement only when the pressure drop is lower than 40 mbar.

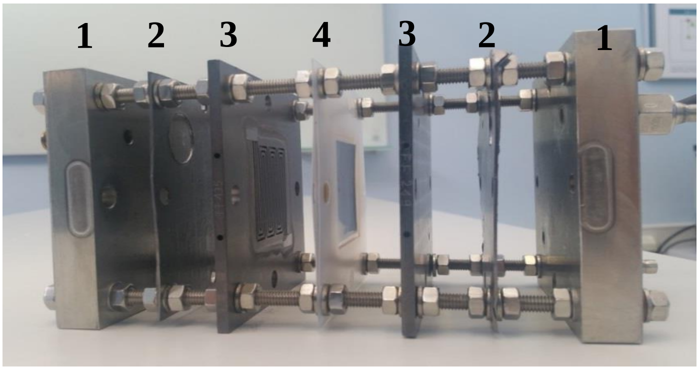

Figure 2.3: Photograph of HT-PEFCs single cell in an exploded view.

2.2. Electrochemical tests of HT-PEFCs

After the assembly and gas leakage test processes, the HT-PEFCs were tested on an automated test station. In Figure 2.4, the temperature and gas flow rates of the HT-PEFCs are regulated by a controlling system that is operated on a computer. The anode and cathode are supplied with H_2 and air, respectively, with a stoichiometry of 2/2. The lower part of the figure are power devices.

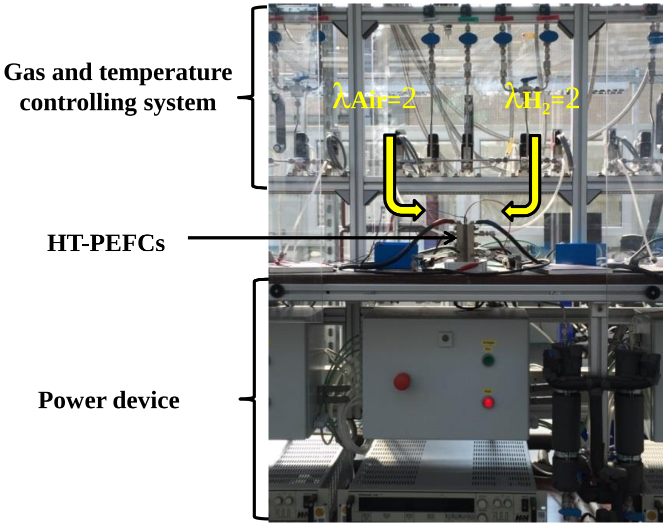

Figure 2.4: Photograph of the automotive test station for HT-PEFCs.

The first operation applies to the HT-PEFCs was a break-in procedure by running at 200 mA cm^{-2} for 70h. Then, the polarization curve was recorded. The current density increased by 10 mA cm^{-2} every 2 min when the current density was lower than 100 mA cm^{-2} and then increased by 50 mA cm^{-2} every 2 min until the voltage was lower than 0.3 V.

The cathode EIS, CV and LSV measurements were conducted by an IM 6 unit from Zahner-Elektrik, with the anode functioned as a quasi-reference electrode. Before the EIS measurement, the HT-PEFCs were kept at the desired current densities (e.g., 100 mA cm^{-2} and 200 mA cm^{-2}) at 160 ℃ for 15 min to reach a steady condition. Then the Nyquist plots were recorded and fitted by using the THALES software. After that, the current load was switched off for the CV and LSV tests. The anode and cathode were supplied with hydrogen and nitrogen with flow rates of 4.6 mL min^{-1} cm^{-2} and 6.9 mL min^{-1} cm^{-2}, respectively. 5 cycles of CVs were measured between 0.05 V and 1.2 V at a scan rate of 50 mV s^{-1}, with the last round chosen for the ECSA evaluation. The LSV test was carried out between 0.05 and 0.5 V at a scan rate of 5 mV s^{-1}.

2.3. MEA Characterizations

2.3.1. Electron microscopy

Scanning electron microscopy (SEM) and energy dispersive X-ray (EDX) mapping images were taken on a Zeiss Gemini Ultra Plus microscope. Focused ion beam/scanning electron microscopy (FIB/SEM) tests were carried out on a field emission scanning electron microscope (FE-SEM) (Zeiss Crossbeam 540). Since the electron microscope tests require operation in a vacuum environment, the MEA sample was washed with deionized water to remove the phosphoric acid inside. The washing process was as follows: Firstly, the MEA was washed by deionized water at 80 °C for 2 h. Secondly, the MEA was washed three times in an ultrasonic bath for 10 minutes each time. Thirdly, the MEA was washed by deionized water again at 80 °C for 2 h. Finally, the MEA was dried at 150 ℃ for 1 h. During the ultrasonic washing process, the gas diffusion layers and most of the catalyst were also removed. Figure 2.5A shows a photograph of the MEA sample. It can be clearly observed that alternating orange and black stripes appear on the membrane, which is considered to be the catalysts (black) adhering to the membrane (orange) caused by the stress under the ribs. The area under the rib was selected for the FIB/SEM measurements: i) to test the samples under the same environment; 2) to visualize the catalyst agglomeration. Figure 2.5B exhibits an SEM image of the FIB-prepared cross section. The rectangular crater was cut by using a finely focused ion beam (usually gallium), while the white area above the catalyst was a protective layer of Pt deposition. The EDX map of Pt was performed in the range of 5 μm in the direction perpendicular to the membrane. The EDX line profile corresponding to the plotted line (red) was the average of the Pt atom% in the mapped area, as shown in Figure 2.5C.

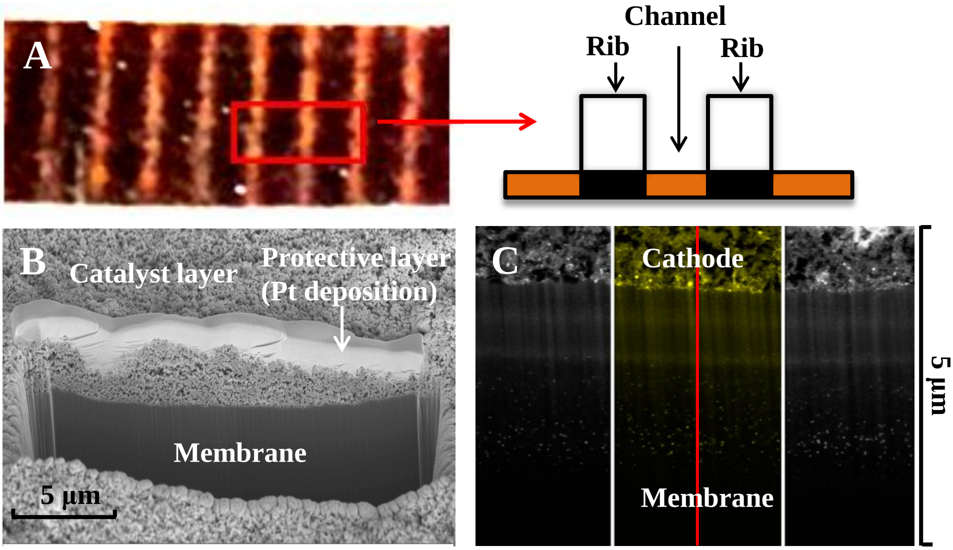

Figure 2.5: (A) Photograph of the washed MEA sample and the schematic cross-section of the rib and channel areas; (B) SEM image of the FIB-prepared cross-section; (C) a sample of the EDX mapping and line-scan profile of Pt.

2.3.2. Inductively coupled plasma-mass spectrometry (ICP-MS)

To compare the PA leaching and Pt loss outside the HT-PEFCs, the exhaust water was collected from the cathode side by cooling the gas stream to 7 °C. The concentrations of PO_4^{3-} and Pt in the water were analyzed by the inductively coupled plasma-mass spectrometry (ICP-MS) technique. The phosphate was determined by continuous flow analysis (CFA). The relative errors were 8%, 5% and 2% with the concentration smaller than 0.5 μg ml^{-1}, in the range of 0.5-1 μg ml^{-1} and in the range of 1-3 μg ml^{-1}, respectively. For the Pt detection, 3 replicate dilutions of each sample were prepared and analyzed. Due to the small Pt concentration in the collected water near the limit of detection, the standard deviation is relatively large.

2.3.3. Brunauer–Emmett–Teller (BET) measurement

The specific surface area (BET) and pore size distribution (BHJ) were measured by a Micromeritics Gemini VII device with a software V1.03t. The BET values have an error of up to 10%. From the models available for BJH analysis, the ‘Carbon Black STSA’ was chosen since this is the most suitable one. The BJH desorption analysis was used to determine the pores sizes under 30 nm.

2.4. Durability test

To investigate the degradation mechanism and compare the degradation behaviors of HT-PEFCs, the durability tests were carried out using different cathodes under various conditions. The cathodes with different Pt loadings, thicknesses, PADLs and contents of PTFE were prepared. The operating strategies include the standard condition, high temperature, thermal cycling, OCV and load cycling. A 100 h aging test was applied to identical home-made HT-PEFCs. Before the durability test, a polarization curve, EIS and CV were recorded as beginning of life (BOL). After the durability test, electrochemical measurements were performed again and recorded as end of life (EOL).

3. Effect of cathode morphology on the performance of HT-PEFCs

In this chapter, gas diffusion electrodes with different morphologies were prepared by using different fabrication methods and binders. The morphologies were characterized using SEM, EDX mapping, scanning electrochemical microscopy and BET technologies and the electrochemical performances were compared by polarization curve, EIS and CV.

3.1. Cathodes prepared by spraying and doctor blade methods

In this section, part of the work was done with the help of Ms. Lei Wu, who is a master student under my supervision.

3.1.1. Electrode morphology

The GDEs prepared by the doctor blade and air spraying methods are named as GDE 1 and GDE 2, respectively. Figure 3.1A and B show the large-scale images, and it is observed that GDE 1 exhibits more regular cracks and flatter surface morphology compared to GDE 2; the edge of the catalyst blocks is tilt in GDE 2. Figure 3.1C and D show the magnified images. Large White agglomerations are only observed in GDE 1 and will be discussed later. Furthermore, compared to GDE 1, GDE 2 shows a more smooth surface morphology. Figure 3.1E and F are SEM images of the nanoscale structure. We can see that GDE 1 seems to exhibit a more compact structure than GDE 2.

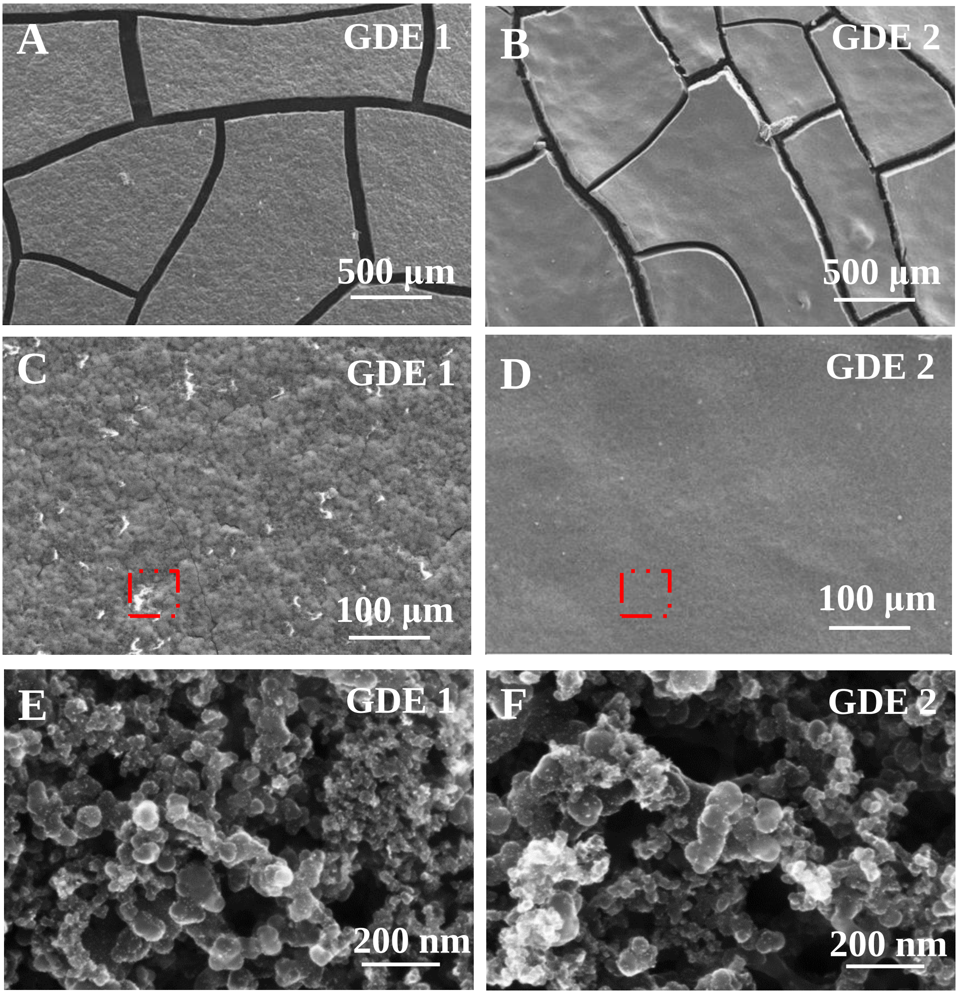

Figure 3.1: (A), (C) and (E) are SEM images of the GDE prepared by the doctor blade method at different magnifications; (B), (D) and (F) are SEM images of the GDE prepared by the air spraying method.

Figure 3.2 displays the magnified SEM images in red boxes of Figure 3.1 and the corresponding EDX maps of fluorine and platinum. Fluorine is a constituent only in the polytetrafluoroethylene (PTFE) binder, so the distribution of fluorine can indicate the distribution of the binder in the

GDEs. Accordingly, the white agglomerations in GDE 1 are caused by PTFE agglomeration and GDE 2 exhibits better PTFE dispersion than GDE 1. This can be explained by the different preparation processes of the GDEs. Compared to GDE 1, more solvent is used in the ink of GDE 2 and the ink is sprayed on the GDL layer by layer, leading to a more homogeneous PTFE distribution in GDE 2.

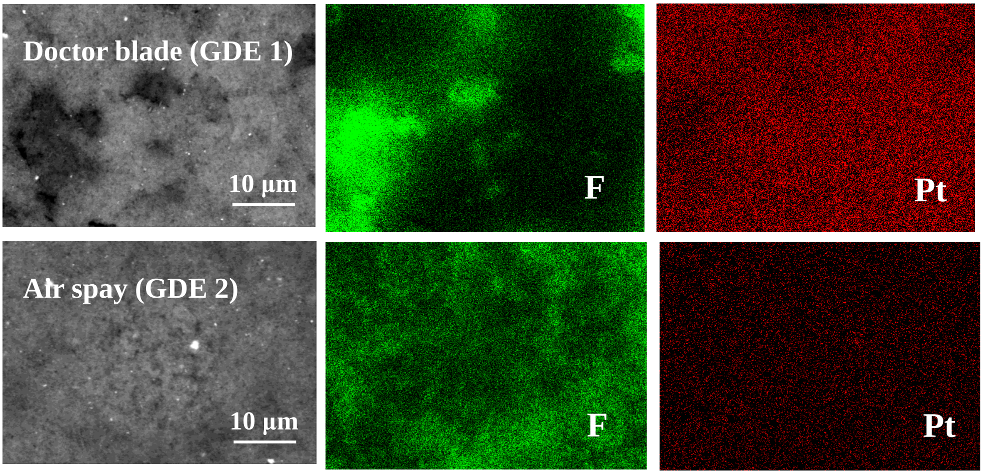

Figure 3.2: Magnified SEM images of GDE 1 (above) and GDE 2 (below) in red boxes of Figure 3.1 and the corresponding EDX maps of fluorine and platinum.

3.1.2. Electrochemical tests

The polarization curves and EIS plots of MEAs with the GDE 1 and GDE 2 used as cathodes were recorded, as shown in Figure 3.3. In the Tafel region, the two MEAs exhibit the same performance, indicating a limited effect of the preparation methods on the kinetics of ORR. The performance difference between MEA 1 and MEA 2 increases as the current density goes higher. MEA 2 shows an approximately linear voltage-current relationship, while the voltage decreases rapidly in MEA 1 when the current density is higher than 700 mA cm^{-2}. To give an explanation for the performance difference, EIS measurements were conducted at 200 mA cm^{-2} at 160 ℃. We can see in Figure 3.3B that both of the Nyquist plots exhibit two arcs and MEA 1 shows a larger overall resistance by comparing the right intercepts of the x-axis on the plots. Further details related to the resistances can be seen in Table 3.1.

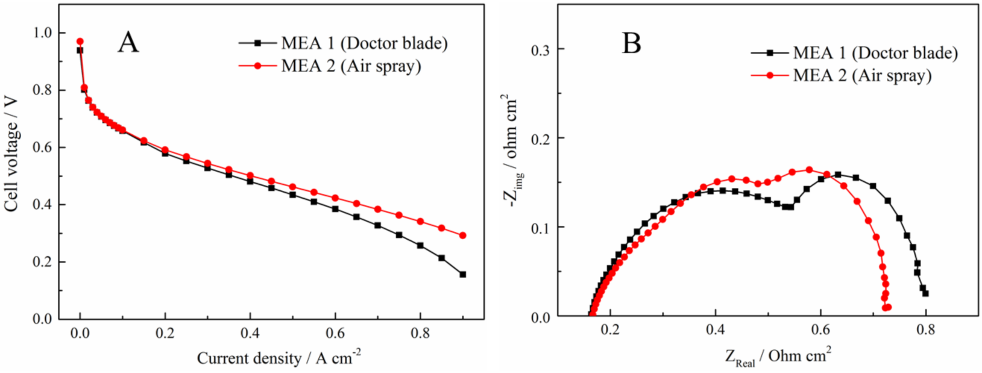

Figure 3.3: (A) Polarization curves of the MEAs with the cathodes prepared by the doctor blade (MEA 1) and air spraying methods (MEA 2); (B) Nyquist plots of MEA 1 and MEA 2 at a current density of 200 mA cm^{-2}.

As shown in Table 3.1, the MEAs display almost the same ohmic resistance (R_Ω). The ohmic loss is mainly dominated by the ionic resistance in the membrane, and hence R_Ω often refers to as the membrane resistance [95, 96]. The difference between MEA 1 and MEA 2 only lies in the cathode catalyst layer (CCL), so the values of R_Ω are the same. MEA 1 and MEA 2 exhibit similar charge transfer resistance (R_{ct}), corresponding to the comparable performance in the Tafel region of the polarization curves as discussed previously. Moreover, the slightly higher charge transfer resistance (R_{ct}) of MEA 1 than MEA 2 may be caused by the loose structure of the CCL in MEA 2, leading to a higher electrochemically active surface area (ECSA).

The major difference lies in the mass transport resistance (R_m) and cathode protonic resistance (R_p). Compared to MEA 2, MEA 1 exhibits a notably higher R_m. This is ascribed to the compact structure of the CCL and the PTFE agglomeration in MEA 1, hindering the oxygen transport to the Pt catalyst. In addition, the R_p in MEA 1 is obviously lower than that in MEA 2, which can be explained by the uneven edge of the catalyst blocks prepared by the air spraying method.

Table 3.1: Electrochemical properties of the MEAs.

MEA	R_Ω /mΩ cm^2	R_{ct} /mΩ cm^2	R_m /mΩ cm^2	R_p /mΩ cm^2	ECSA /m^2 g^{-1}
MEA 1	164	208	414	52	11.5
MEA 2	166	190	254	137	13.3

3.2. Cathodes prepared with different binders

3.2.1. Electrode morphology

To investigate the effect of different binders on the morphology and performance of GDEs, two types of PTFE (3M Dyneon) i.e., 5060Z and 5032Z PFEE, with the particle sizes of 220 µm and 160 µm were used in the preparation process. The GDEs prepared using 5060Z and 5032Z PFEE are referred to as GDE 3 and GDE 4, respectively. Figure 3.4 shows the SEM and EDX mapping images of GDE 3 and GDE 4. In the SEM backscattered electrons images (Figure 3.4A and B), it can be seen that the surface morphology varies with different types of PTFEs at the same content, and the GDE that contains the PTFE of larger particle size exhibits more irregular cracks. In addition, we can see in Figure 3.4C and D that compared to the fluorine mapping image of GDE 3, a more homogeneous PTFE distribution on the catalyst surface is observed in the Pt map of GDE 4.

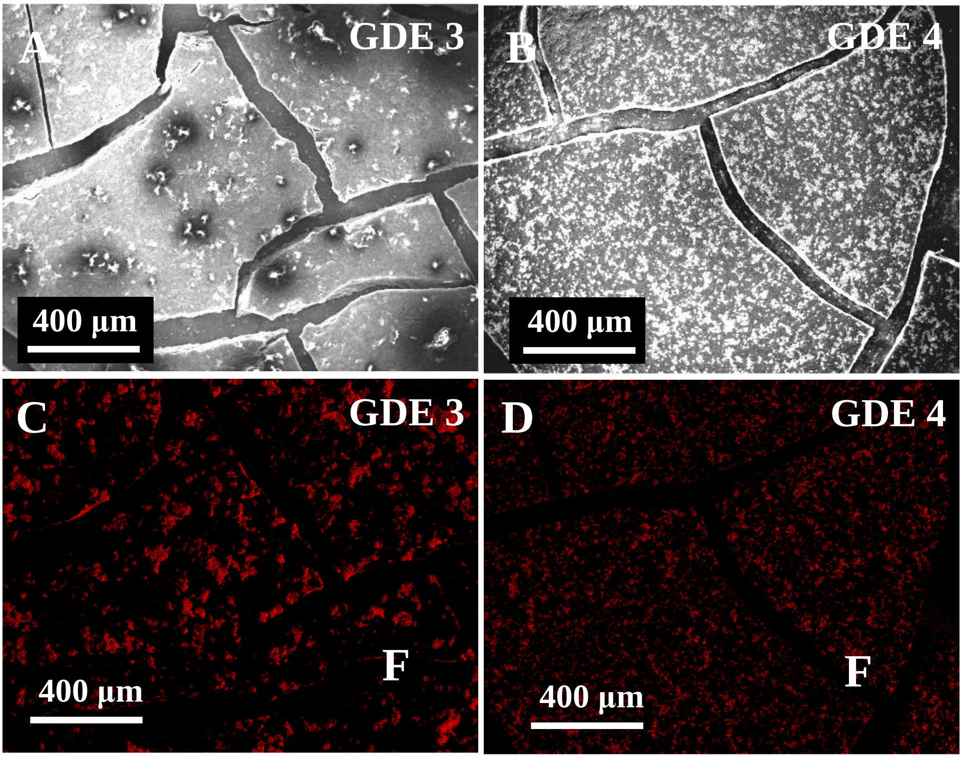

Figure 3.4: SEM images of the GDEs papered by using (A) 5060Z PTFE and (B) 5032Z PTFE; EDX maps of Pt: (C) GDE 3 and (D) GDE 4 [97].

3.2.2. Scanning Electrochemical Microscopy

In order to investigate the effect of the CCL morphology on the electrochemical performance, a 4D shear-based scanning electrochemical microscope (4D-SF/SECM) was used for the ex-situ analysis of the GDEs' electrochemical activity. SECM is an imaging technique in which small-scale electrodes are scanned on an immersed substrate while recording the current response, which depends on the electrochemical activity and surface topography of the substrate [98]. The related measurements were conducted by colleagues from Carl von Ossietzky University of Oldenburg. The results of this cooperation has been previously published [97]. Reproduced with permission from *J. Electrochem. Soc.*, 164, F873 (2017). Copyright 2017, The Electrochemical Society.

The measurements were made in a home-made SECM cell. The studied GDE was fixed at the bottom of the SECM cell with 50 mM H_2SO_4 as the electrolyte. A slight O_2 flow was introduced above the solution. A reversible hydrogen electrode (RHE) was used as the reference electrode (RE) and a Pt mesh as the counter electrode (CE). Figure 3.5A shows the micrograph of the microelectrode used by the colleagues in Oldenburg. During the measurement, the microelectrode was scanned on the GDE while recording the current response. The redox competition mode was applied to evaluate the local electrocatalytic activity of the GDE towards ORR. The microelectrode was maintained at a constant reduction potential of 0.4 V vs. RHE at which ORR occurs. If the GDE reaches the potential for ORR, the GDE and microelectrode compete for oxygen; therefore, the catalytic activity of the GDE is reflected in the current of the microelectrode. As is shown in Figure 3.5B, the scanning process is conducted in a constant-distance mode with current-distance curves recorded.

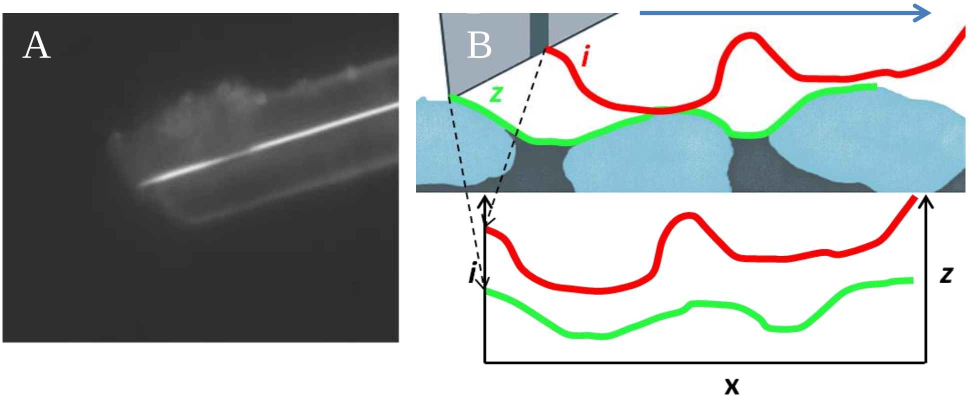

Figure 3.5: (A) Microphotograph of the microelectrode used by the colleagues in Oldenburg; (B) schematic representing the scanning process [97].

Figure 3.6 shows the 4D-SF/SECM images of electrochemical data (upper) and topography (below) for the investigated GDEs used by the colleagues in Oldenburg. It can be seen that the current of the microelectrode competing with GDE 4 is smaller than that with GDE 3, indicating a higher catalytic activity towards ORR of GDE 4. In addition, compared to GDE 3, GDE 4 exhibits a more homogeneous current distribution and morphological appearance. This is caused by the more desired morphology of GDE 4, i.e., more regular cracks and homogeneous PTFE distribution.

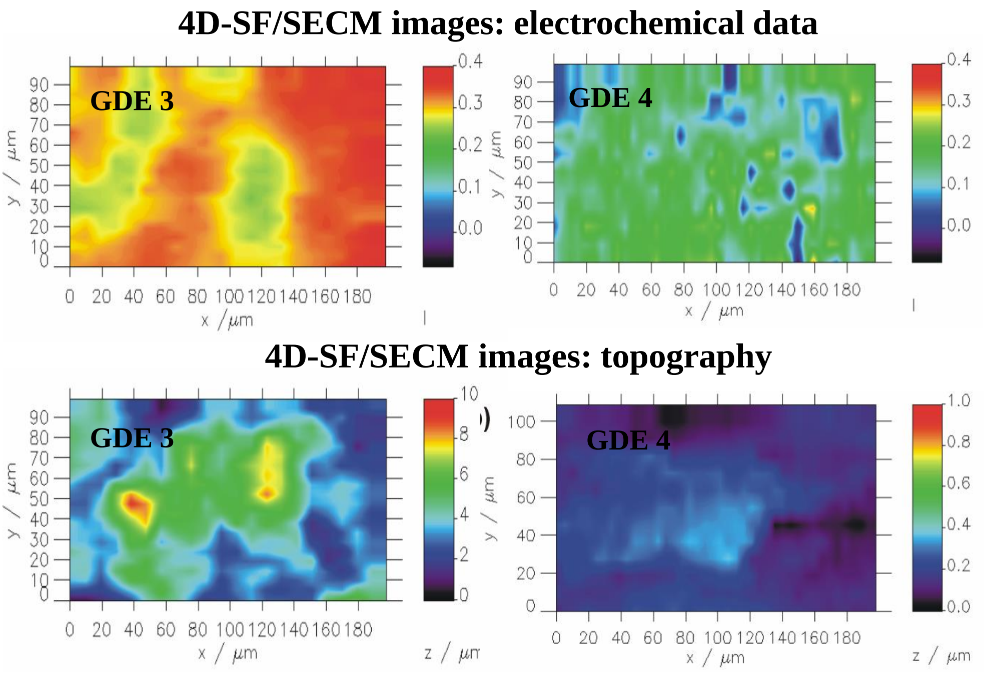

Figure 3.6: 4D-SF/SECM images of GDE 3 and GDE 4. The images upper and below are electrochemical data and topography, respectively. Exp. Data: electrolyte: 50 mM H_2SO_4; CV E_{start} = 0.8 V, E_{low} = 0.1 V, E_{end} = 0.8 V, v = 0.2 V/s; step size x = 5 µm, step size y = 10 µm [97].

3.2.3. Polarization curve

Polarization curves are used to compare the electrochemical performance of the GDEs in HT-PEFCs, as shown in Figure 3.7. MEA 3 and MEA 4 are prepared by using GDE 3 and GDE 4, respectively. It is clearly observed that MEA 4 performs better than MEA 3 over the whole range of current density. In the Tafel region ($j < 0.1$ A cm^{-2}), MEA 4 shows higher voltages than MEA 3 at the same current densities, which is due to the higher catalytic activity towards ORR of GDE 4 (proved by the SECM measurements). As the current density goes higher, the performance difference between the MEAs notably increases. This can be presumably explained by an enhanced contact resistance and interface resistance in MEA 3 due to the non-ideal morphology of GDE 3, resulting in a higher ohmic resistance [99, 100].

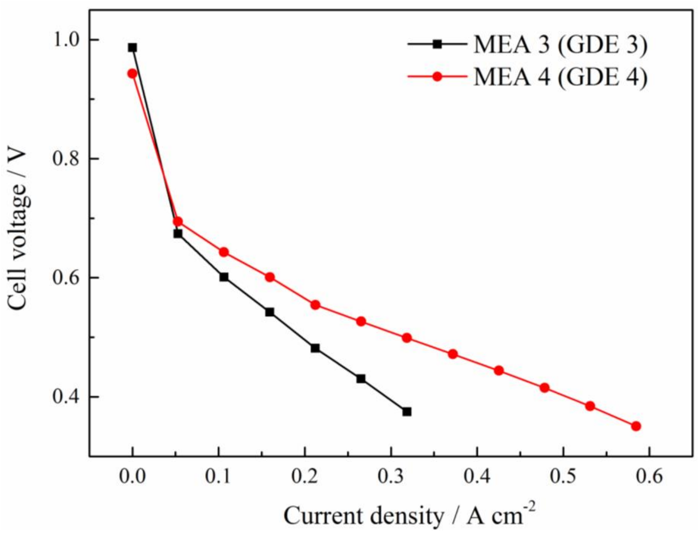

Figure 3.7: Polarization curves of MEAs using GDE 3 and GDE 4 at 160 ℃, λ air/H_2 = 2/2 [97].

3.3. Effect of binder content on morphology and performance

3.3.1. Cathodes prepared by different contents of binder

According to the results above, the doctor blade method and 5032Z PFEE are applied to fabricate the CCLs. Based on the standard electrode (40 wt.% PTFE), the cathodes with the binder content in the range from 0 wt.% to 60 wt.% in the CCLs were prepared by using different recipes and thickness of spacers. The parameters and recipes of the CCLs' preparation processes are shown in Table 3.2 and Table 3.3, respectively.

Table 3.2: Parameters of the CCLs.

PTFE content / wt.%	Thickness of Electrode / μm	Pt loading / mg cm^{-2}
0	95	1.15
5	106	1.17
10	103	1.18
25	130	1.16
40	139	1.12
60	163	1.07

Table 3.3: Recipes for the preparation of the CCLs.

PTFE content / wt.%	Pt/C catalyst / g	Water / mL	Solvent /mL	PTFE solution / μL	Thickness of spacer / cm
0	1.0	1.9	12.7	0	0.7
5	1.0	2.2	14.6	58	0.8
10	1.0	2.4	15.6	74	0.8
25	1.0	2.7	17.5	364	0.9
40	1.0	3.0	19.5	741	1.0
60	1.0	3.6	23.4	1670	1.3

3.3.2. BET measurement

The pore size distribution of the CCLs with different PTFE contents is studied. Figure 3.8 shows the differential pore volume of the pores smaller than 50 nm. Above 4.0 nm, the samples show a similar pore size distribution, only shifted due to the available BET area. Comparing all samples, only minor differences in the pore size range to about 10 nm diameter are found. The most striking differences are found in the pore diameter range between 1.5 nm and 3.0 nm, with the maximum deviation occurring around 2.2 nm. The BET surface area and pore volume are found to decrease with increasing PTFE content in the CCLs, from values of 143 m² g^{-1} and 0.496 cm³ g^{-1} for the 0 wt.% PTFE CCL to 57.6 m² g^{-1} and 0.347 cm³ g^{-1} for the 40 wt.% PTFE CCL, respectively (see in Table 3.4).

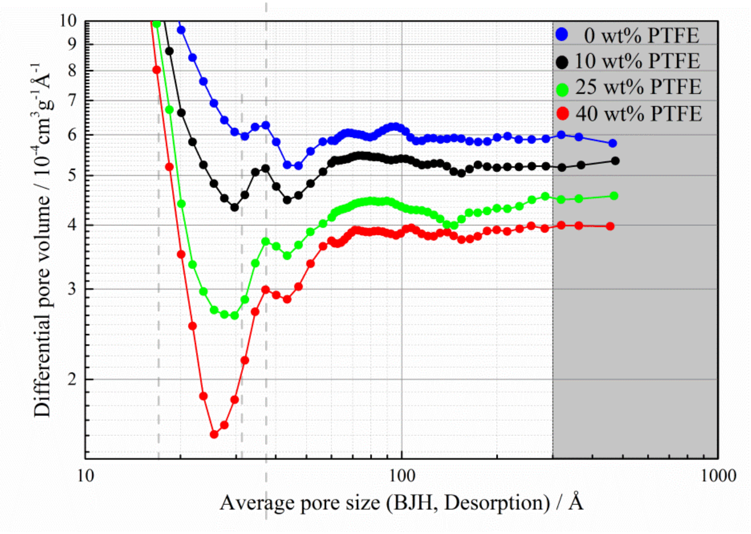

Figure 3.8: Average pore size distribution of the CCLs with different PTFE contents.

Table 3.4: BET measurements of the CCLs.

PTFE wt.%	0 wt.%	10 wt.%	25 wt.%	40 wt.%
BET surface area / $m^2\ g^{-1}$	143	98.2	71.6	57.6
BET pore volume / $cm^3\ g^{-1}$	0.496	0.466	0.390	0.347

3.3.3. SEM and EDX mapping

To investigate the effect of PTFE on the morphology of the catalyst layer, the 10 wt.% and 40 wt.% PTFE catalyst layers are characterized by SEM and EDX mapping. In the SEM cross-section images (Figure 3.9), the low binder catalyst layer shows more homogeneous distributions of PTFE and Pt.

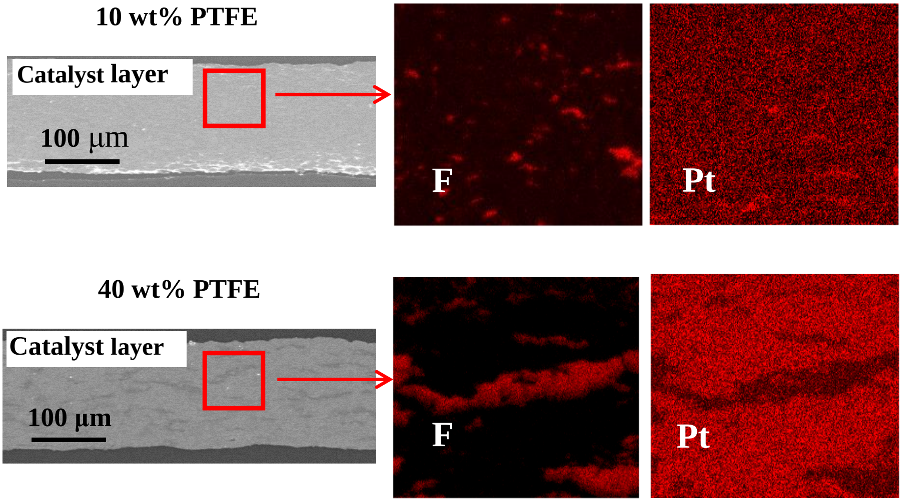

Figure 3.9: Cross-sectional SEM and EDX mapping images of the 10 wt.% and 40 wt.% PTFE catalyst layers.

In the SEM topography images of Figure 3.10, PTFE agglomerations are observed in the catalyst layer that contains higher PTFE content, and the PTFE binder exhibits a cross-linked network structure in the pores. By comparing the higher magnification (scale bar, 200 nm) images, it would seem that the high binder catalyst layer exhibits a more compact structure. This result agrees with the BET measurements that the CCL with a higher PTFE content shows a less porous structure and thus lower BET values.

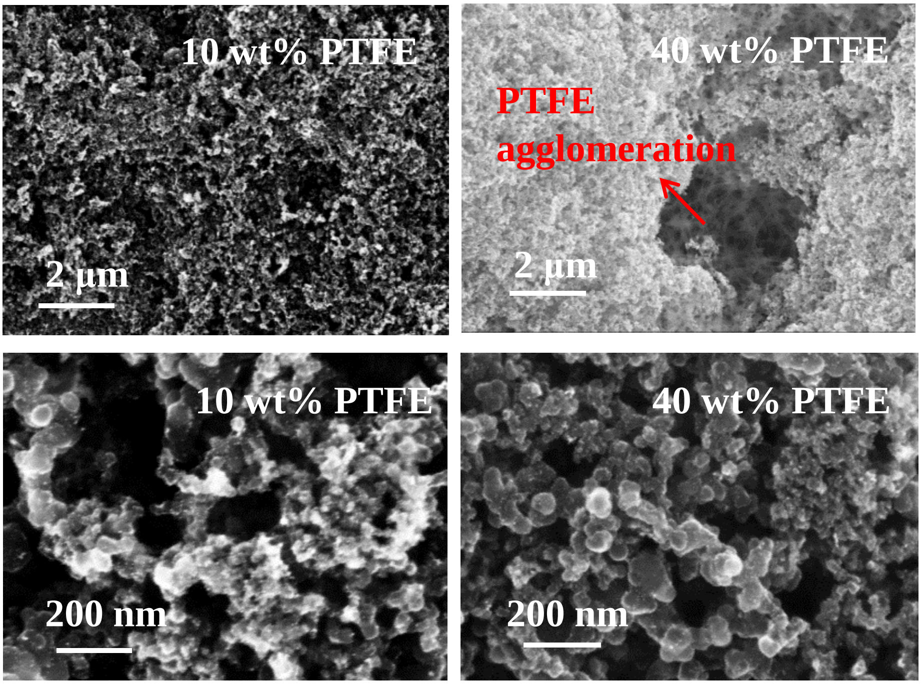

Figure 3.10: SEM topography images of the 10 wt.% (left) and 40 wt.% (right) PTFE catalyst layers.

3.3.4. Comparison of electrochemical properties

For all of the HT-PEFCs, the anodes are identical with the Pt loading of 0.6 ± 0.05 mg cm^{-2} and 40 wt.% PTFE in the catalyst layer. The Pt loading of the cathodes is maintained at 1.1 ± 0.1 mg cm^{-2} with different contents of PTFE. Figure 3.11 shows the polarization curves of the HT-PEFCs. In the Tafel region (j＜0.1 A cm^{-2}), there are moderate differences in the performance, implying that PTFE could affect the kinetics of the ORR on the cathode side. The differences in the curves are significant at relatively high current densities. The HT-PEFC with 60 wt.% PTFE in the CCL exhibits a considerably lower performance than the other HT-PEFCs, while the 10 wt.% PTFE HT-PEFC exhibits the best electrochemical performance.

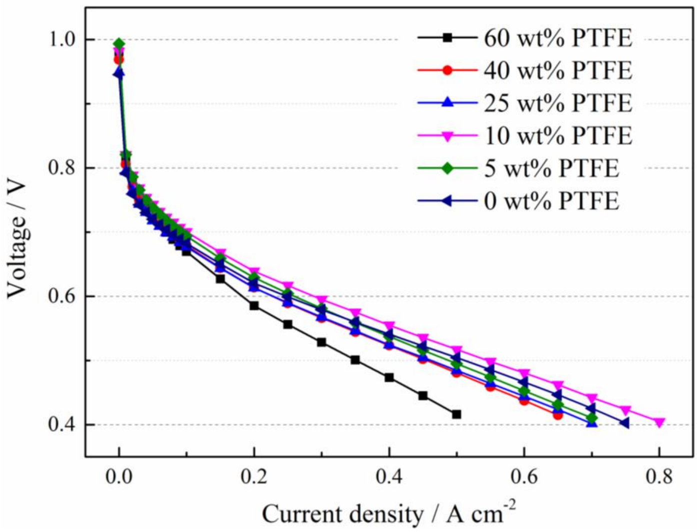

Figure 3.11: The polarization curves of the HT-PEFCs operated at T = 160 ℃, stoichiomitry: Air/H_2 = 2/2 with different PTFE contents after the 72h break-in procedure. Acid doping level: 15 ± 0.5 mg cm^{-2}.

Table 3.5 shows the Tafel slopes and voltages of the cells at 200 mA cm^{-2}. The 0 wt.% PTFE cell shows the lowest Tafel slope of 0.095 V decade^{-1}, indicating the highest kinetics of ORR at the cathode. The 60 wt.% PTFE cell exhibits a notably higher Tafel slope value (0.131 V decade^{-1}) than the other cells, demonstrating that the kinetics of ORR is negatively affected by an excessive amount of PTFE. In our case, the PA distribution in the CCLs is different due to the different hydrophobicity levels of the catalyst layers, probably leading to changes in the ORR path or limiting case, further causing the changes of the Tafel slope [81]. The voltage of the standard HT-PEFC (40 wt.%) is 0.613 V, which is improved by reducing the PTFE content in the CCL, with the highest value of 0.639 V in the 10 wt.% PTFE cell (26 mV higher than the standard cell). These results indicate that the binder content of PTFE has an important influence on HT-PEFCs' performance.

Table 3.5: Tafel slopes and voltages of the HT-PEFCs at 200 mA cm^{-2}.

PTFE / wt.%	Tafel slope / mV dec^{-1}	Voltage at 200 mA cm^{-2} / V
0 %	0.095	0.620
5 %	0.113	0.629
10 %	0.107	0.639
25 %	0.112	0.613
40 %	0.113	0.613
60 %	0.131	0.585

Figure 3.12 shows the cathode CVs of the HT-PEFCs in the scan range from 50 mV to 505 mV. The peaks at 0.13 V and 0.28 V are assigned to the hydrogen desorption on Pt (110) site and Pt (100) edge and corner sites, respectively [101]. The peak at 0.13 V is clearly observed in the HT-PEFCs. Interestingly, the peak at 0.28 V is not obvious in the cells with 60 wt.%, 40 wt.% and 25 wt.% PTFE in the CCLs. This is presumably explained by the blockage of the Pt (100) site when the PTFE content is over 25 wt.%. Similar statements have been reported in classic PEFCs [102, 103]. Friedmann et al. found that the PTFE binder in CCLs could cause the blockage of active catalyst sites and decrease in hydration of the catalyst surface area, thus resulting in lower catalyst utilization and poor proton conduction [103]. The calculated ECSA decreases as the PTFE content increases. The ECSA of the cathodes with 0 wt.%, 25 wt.% and 60 wt.% PTFE are 18.4, 13.8 and 11.6 m^2 g^{-1}, respectively. These results are consistent with the Tafel slopes of the cells discussed previously. The reduced ECSA causes a decrease in the exchange current density of ORR, which ultimately leads to an increase in the Tafel slope.

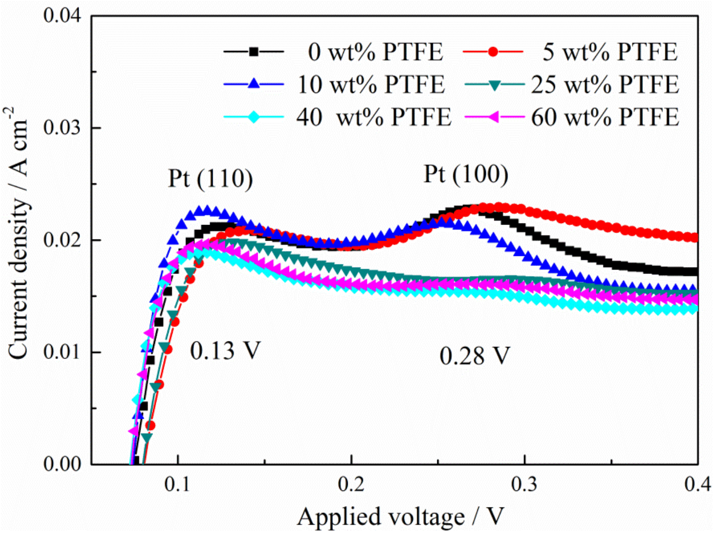

Figure 3.12: The test conditions of the cyclic voltammetry are as follows: cell temperature is 160 ℃; hydrogen and nitrogen with the flow rates of 66.4 mL min^{-1} nitrogen 99.6 mL min^{-1} are supplied in the anode and cathode sides, respectively. The scan rate is 50 mV s^{-1} with a scan range 50-505 mV.

The Nyquist plots are recorded at 200 mA cm^{-2} and fitted by the above-mentioned equivalent circuit model, as shown in Figure 3.13. It is clear that the charge transfer resistance (R_{ct}) for the HT-PEFCs is comparable due to the same catalyst used in the CCLs and operating conditions. The mass transport resistance (R_m) varies significantly with the PTFE content, while the 10 wt.% PTFE HT-PEFC shows the smallest value. PTFE molecules are known to be hydrophobic. Therefore, compared to the 10 wt.% PTFE HT-PEFC, the PA content increases in the CCLs as the PTFE concentration decreases (0 and 5 wt.% PTFE), and the excessive PA leads to the PA flooding effect, hindering the O_2 transport in the electrode [104]; at higher PTFE concentrations (25, 40, and 60 wt.% PTFE), the CCLs are highly hydrophobic with reduced PA content; however, the large PTFE agglomerations can block the porous structures in the CCLs, leading to an increase in R_m. For the cathode protonic resistance (R_p), it remains constant when the PTFE content is lower than 10 wt.%. After that, the R_p increases dramatically, which is caused by the increased hydrophobicity of the catalyst layer surfaces and therefore considerably decreased PA concentrations in the CCLs. The ohmic resistance (R_Ω) is not obviously affected by the different PTFE concentrations in the CCLs. This is due to the excess PA doping in the membrane, and hence the PA redistribution has no obvious effect on the R_Ω. The 60 wt.% PTFE cell shows a slightly higher R_Ω value than other cells, resulting from a decrease in the electron conductivity of the catalyst layer by the presence of a large amount of non-conductivity PTFE.

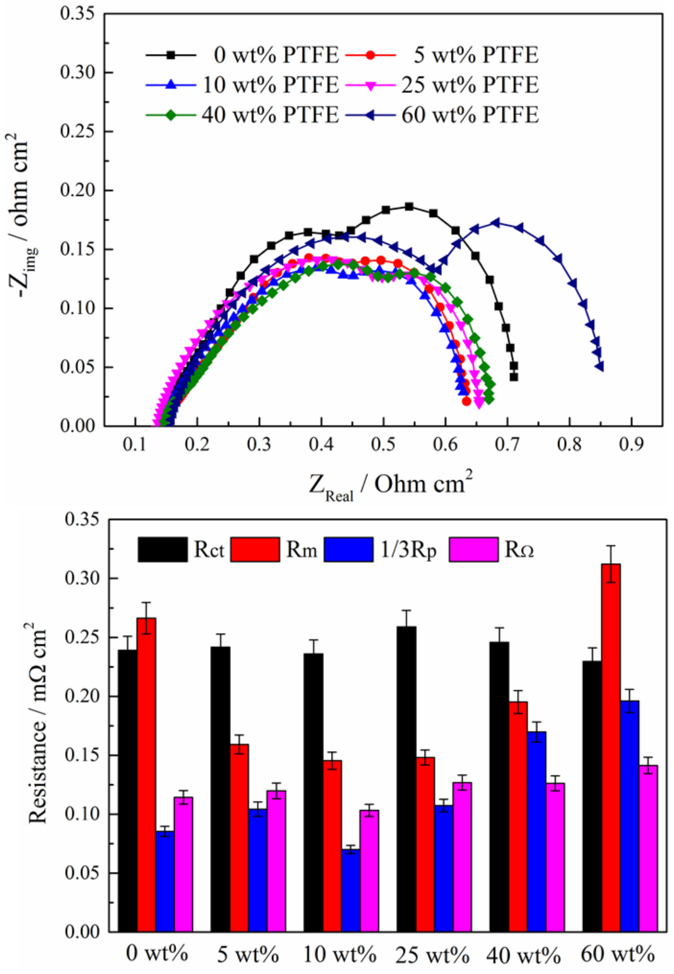

Figure 3.13: Nyquist plots and the corresponding fitting results of the HT-PEFCs with different PTFE contents in the CCLs.

3.4. Summary

In this chapter, various GDEs are prepared and characterized by electron microscopy and electrochemical methods. The results demonstrate that the morphology of the catalyst layer has a strong effect on the performance of HT-PEFCs.

- Compared to the GDE prepared by the air spraying method, the GDE prepared by the doctor blade method shows cross-linked PTFE agglomerations in the catalyst pores and a more compact structure.
- The air sprayed GDE beneficially influences the HT-PEFCs' performance by reducing the mass transport resistance due to the more desirable catalyst morphology.
- The particle size of the 5032Z PTFE is smaller than that of the 5060Z PTFE (160 μm vs. 220 μm). Electrodes with the smaller particle size of PTFE binder exhibit more regular cracks and more uniform PTFE distribution, which favor the ORR and show better performance over the entire range of current density.
- SECM can be used as an in-situ analysis to assess the morphology and local electrochemical activity of GDEs towards the ORR, which provides an effective way to evaluate the electrochemical performance prior to assembling them in HT-PEFC stacks.
- The BET surface area and pore volume decrease as the PTFE content increases. Compared to the 40 wt.% PTFE GDE, the 10 wt.% PTFE GDE presents more uniform PTFE and Pt distributions, resulting in a lower mass transport resistance and protonic resistance, and thus enhanced cell performance.
- Electrodes with 10 wt.% PTFE in the catalyst layer show the best electrochemical performance.

According to the results above, the spraying method is more suitable for the preparation processes of GDEs. However, the air spraying process is time-consuming, which brings difficulties to the research. Therefore, in the following sections, the doctor blade method is still applied to prepare GDEs. Since the preparation technology is very important for improving the electrochemical performance of GDEs, more advanced and time-saving spraying technology should be studied in the future.

The PTFE binder evidently impacts the performance of HT-PEFCs by adjusting the PA distribution in CCLs. The lack of PTFE in the CCL leads to the PA flooding effect and thus a high mass transport resistance, while excessive PTFE in the CCL enhances the hydrophobicity of the catalyst interface and blocks the porous structure, resulting in an increased cathode protonic resistance and mass transport resistance. By this, an optimized PTFE content (10 wt.%) is given according to the electrochemical performance of the HT-PEFCs. However, the effect of PTFE on the durability of HT-PFECs has not been investigated, which should be one of the significant factors for optimizing the PTFE content and will be discussed in the next chapter.

4. Role of PTFE on HT-PEFC durability

The effects of PTFE content at the cathode on cell durability are studied in this chapter. OCV and high potential cycling as effective stressors are applied to accelerate the degradation of HT-PEFCs.

4.1. OCV operation

4.1.1. Voltage-time and polarization curves

Two cells with 10 wt.% PTFE and 40 wt.% PTFE in the CCLs, respectively, are subjected to a 100 h OCV operation. Figure 4.1A shows the voltage-time curves and voltage degradation rates (VDRs) of the HT-PEFCs. The VDR is calculated by the equation below:

$$\mathrm{VDR} = (V_{\mathrm{BOL}} - V_{\mathrm{EOL}}) / 100\ \mathrm{h} \tag{4.1}$$

It can be seen that the voltage rapidly increases at the beginning of the OCV operation. This is explained by a fast decrease in water vapor partial pressure under the currentless and non-humidified condition, resulting in an increase in the cell voltage according to the Nernst equation. In addition, the removal of water leads to the dehydration transformation from phosphoric acid to pyrophosphoric acid, and changes in gas solubility in the two PA species may also contribute to this trend [105, 106]. The equation of the PA dehydration process in the membrane is shown as below:

$$2H_3PO_4 \rightleftharpoons H_4P_2O_7 + H_2O \tag{4.2}$$

After that, the 10 wt.% and 40 wt.% PTFE cells show a similar OCV aging trend with the VDRs of 112 and 120 μV h^{-1}, respectively. The OCV loss is considered to be related to the increased hydrogen crossover caused by membrane degradation [107]. The similar degradation rate indicates that the PTFE content in the CCL has no effect on membrane degradation. Figure 4.1B shows BOL and EOL polarization curves of the HT-PEFCs. We can see that both cells exhibit pronounced performance degradation, indicating that OCV condition is detrimental for the durability of HT-PEFCs. The difference in performance degradation of the HT-PEFCs will be discussed below.

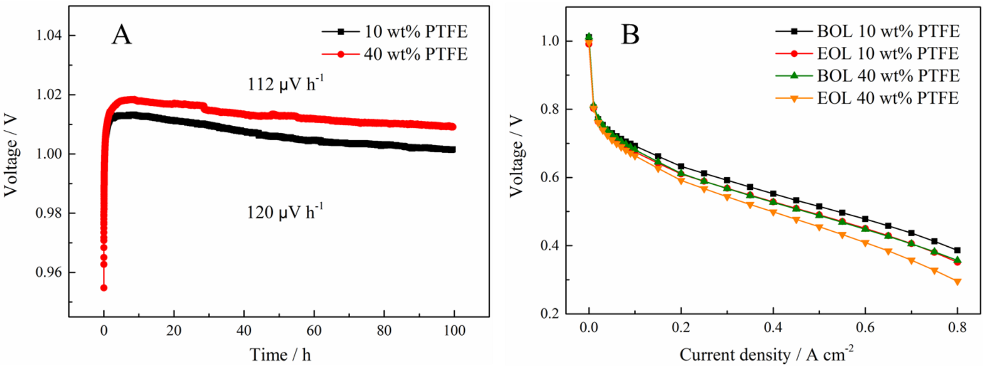

Figure 4.1: (A) Changes in cell voltage over time of the 10 wt.% PTFE and 40 wt.% PTFE HT-PEFCs during the 100h OCV operation; (B) BOL and EOL polarization curves of the HT-PTFEs at 160 ℃ with anode/cathode λ of 2/2.

4.1.2. Degradation rate comparison

The calculated degradation rates for the HT-PEFCs are plotted in Figure 4.2. At low current densities below 200 mA cm^{-2}, there is a minor difference in the degradation rate. Then, the difference of the curves increases substantially. The interesting result signifies that the durability of HT-PEFCs is influenced by the content of PTFE in the CCL. The 40 wt.% PTFE HT-PEFC shows an exponential increase in the degradation rate at higher current densities, while the 10 wt.% PTFE HT-PEFC shows an approximately linear increase. At 800 mA cm^{-2}, the degradation rate of the 40 wt.% PTFE HT-PEFC is 661 μV h^{-1}, which is almost twice that of the 10 wt.% PTFE HT-PEFC (347 μV h^{-1}).

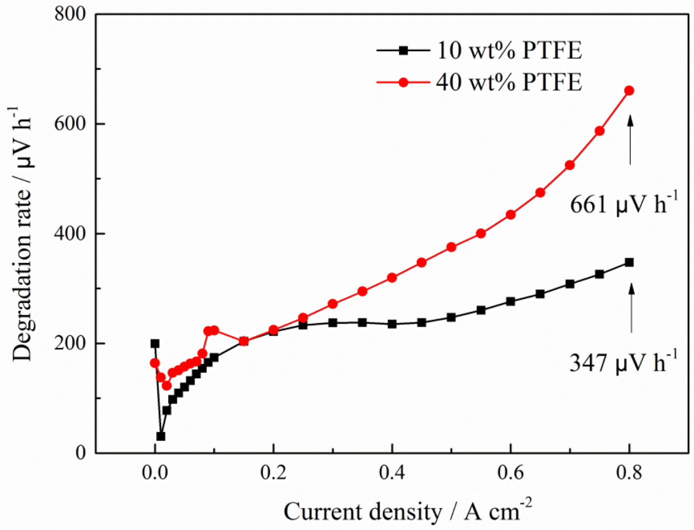

Figure 4.2: Comparison of degradation rates for the HT-PEFCs with different PTFE contents in the CCLs.

4.1.3. Electrochemical impedance spectroscopy

The BOL and EOL Nyquist plots, as shown in Figure 4.3, are recorded at 200 mA cm^{-2} and fitted by the equivalent circuit discussed above (see section 1.3).

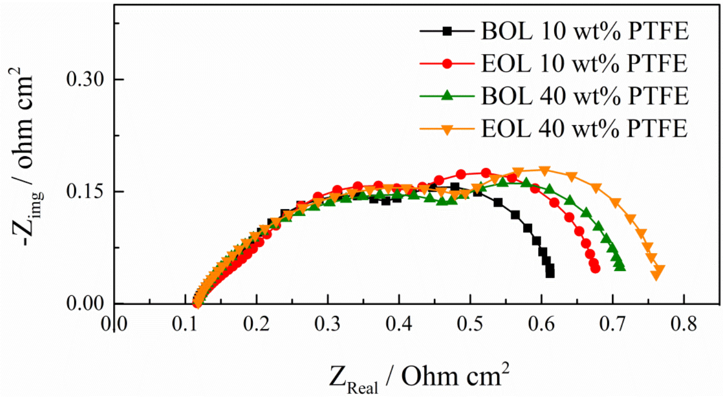

Figure 4.3: BOL and EOL Nyquist plots of the HT-PEFCs.

Figure 4.4A and B show the fitting results from the Nyquist plots of the 10 wt.% PTFE and 40 wt.% PTFE cells, respectively. By comparing the BOL and EOL values, there is a significant increase in the R_{ct} of the 10 wt.% PTFE cell, while a small increase of the 40 wt.% PTFE cell. It is well known that PTFE plays a role in binding the catalyst and improving the mechanical property of the CCL [104]. Therefore, the low binder MEA (10 wt.% PTFE) could probably suffer a more severe Pt corrosion during the aging process, and thus a greater increase in R_{ct}.

On the contrary, the high binder MEA (40 wt.% PTFE) exhibits a more increase in R_m than the low binder MEA. This can be explained by the fact that severe carbon corrosion/oxidation and PA flooding take place at the cathode during the OCV hold test, which negatively influences the transport of reactant gases [108], and the high binder MEA with the more compact structure in the CCL is more susceptible to a mass transport problem.

The R_p and R_Ω are almost identical before and after the aging for both the HT-PEFCs.

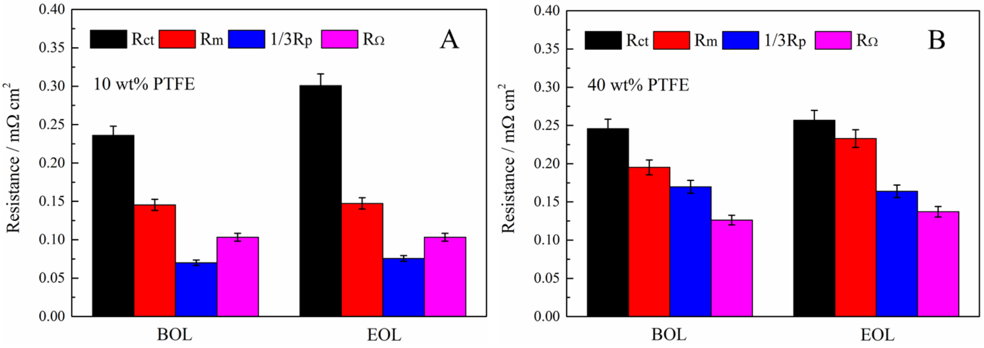

Figure 4.4: The fitting results of BOL and EOL EIS data for the HT-PEFCs with (A) 10 wt.% and (B) 40 wt.% PTFE.

4.1.4. Cyclic voltammetry

The cathode CV plots and the corresponding ECSA before and after aging are shown in Figure 4.5. The oxidation currents between 0.1 and 0.3 V and between 0.9 and 1.2 V are ascribed to the hydrogen desorption and formation of Pt oxides, respectively [109]. We can see in Figure 4.5A that the currents decrease after aging, which is caused by the loss of ECSA for the Pt/C catalyst. The low binder MEA shows a higher ECSA loss during the OCV operation compared to the high binder MEA (1.98 $m^2\ g^{-1}$ vs. 1.58 $m^2\ g^{-1}$). The results could be applied to explain the higher increase in the R_{ct} of the low binder MEA (10 wt.% PTFE) in the EIS measurements.

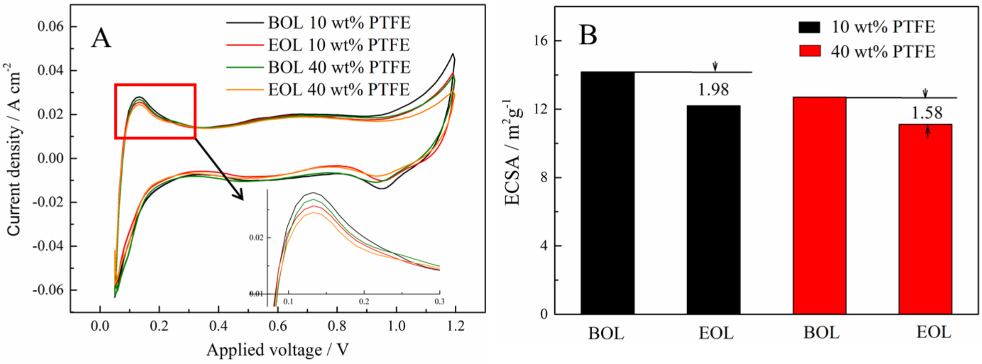

Figure 4.5: (A) Cathode CV curves of the HT-PEFCs; (B) calculated ECSA before and after aging.

4.1.5. Voltage loss contributions

To further understand the PTFE effect on the performance degradation across the whole current range, the UI curves and electrochemical characteristics are analyzed to quantify the voltage loss contributions by the equation below [110]:

$$E_{\text{IR-free}} = E_{\text{eq}} - \eta_{\text{act}} - \eta_{\text{conc}} \tag{4.3}$$

where $E_{\text{IR-free}}$ is the IR-free cell voltage calculated by adding η_{Ω}, E_{eq} the thermodynamic equilibrium potential 1.14 V, η_{act} the activation overpotential due to reaction kinetics and η_{conc} the concentration overpotential due to mass transfer limitations.

Figure 4.6 shows the calculated voltage loss contributions of the HT-PEFCs with different PTFE contents. Comparing the η_{act} curves, we can see that the η_{act} rises for both MEAs after aging, and the difference between BOL and EOL increases as the current density increases. The same trend is observed in the η_{conc} of the high binder MEA (40 wt.%), while the low binder MEA (10 wt.%) exhibits a different aging behavior, with the η_{conc} remaining almost constant over the entire current range.

The low binder MEA shows a slightly higher increase in η_{act} than the high binder MEA (28.7 mV vs. 26.3 mV at 800 mA cm^{-2}), as shown in Figure 4.6A. We can see in Figure 4.6B that there is a considerable increase in the η_{conc} for the high binder MEA. At 800 mA cm^{-2}, the increase in η_{conc} for the low binder MEA and high binder MEA are 6.0 mV and 34.3 mV, respectively.

The binder (PTFE) can improve the mechanical properties of the Pt/C catalyst, leading to a decrease in the catalyst degradation rate. However, the negative effects of PTFE on cell's performance outweigh the positive effects. After aging, the high binder MEA suffers a severe mass transport problem.

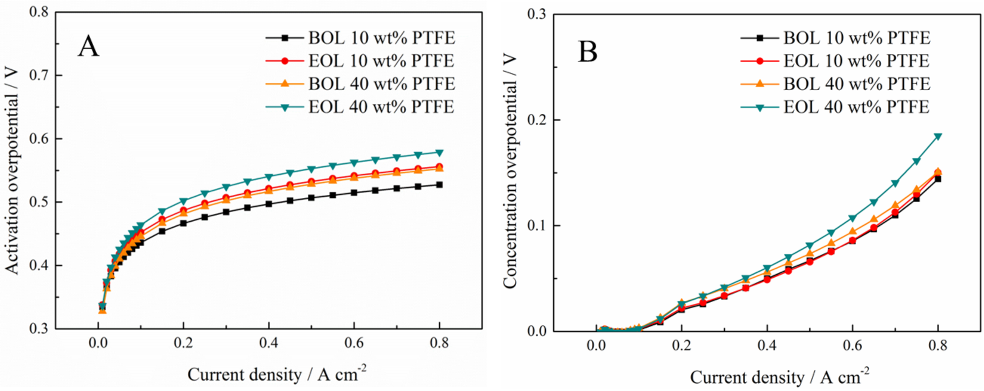

Figure 4.6: (A) Activation overpotential and (B) concentration overpotential of the HT-PEFCs before and after the 100 h OCV operation.

4.1.6. Recovery test

During the OCV operation, HT-PEFCs' performance is influenced by both the reversible and irreversible processes [111]. The irreversible degradation is considered to be originated from the catalyst agglomeration, carbon corrosion and membrane degradation; reversible degradation is mainly caused by the Pt surface oxidation and PA redistribution [74]. It is reported that load cycling tests can be used to recover cells' performance by removing the effect of reversible processes during the OCV operation [70, 111].

To exclude the effect of reversible processes on the voltage drop during the OCV hold test, the HT-PEFCs are operated under a current cycling profile. As is shown in Figure 4.7A, the current density jumps between 200 to 600 mA cm^{-2} at an interval of 50 mA cm^{-2} every 5 min. The low load operating mode, especially consists of open circuit conditions, is known to accelerate proton-exchange membrane (PEM) decomposition [112]. Thereby, a relatively high current density range between 200 to 600 mA cm^{-2} is chosen to keep the voltage below 0.7 and thus avoid severe carbon and Pt corrosion [108]. The voltage-time curves of the 10 wt.% and 40 wt.% PTFE cells during the 100 h operation are depicted in Figure 4.7 B. Interestingly, the voltage of the 40 wt.% PTFE cell increases over time at most current densities, while the 10 wt.% PTFE cell slightly decreases at all current densities.

The BOL and EOL voltages at 200, 400 and 600 mA cm^{-2} of the HT-PEFCs are listed in Table 4.1. The voltage of the 10 wt.% PTFE cell drops at the three current densities, while the 40 wt.% PTFE cell exhibits a different trend, with the voltage increasing at 400 and 600 mA cm^{-2} from 0.477 and 0.393 V to 0.483 and 0.407 V, respectively, due to the recovery of reversible degradation.

Table 4.1: The BOL and EOL voltages at different current densities.

PTFE content	200 mA cm^{-2}	400 mA cm^{-2}	600 mA cm^{-2}
10 wt.% BOL	0.605	0.512	0.440
10 wt.% EOL	0.588	0.498	0.417
40 wt.% BOL	0.571	0.477	0.393
40 wt.% EOL	0.568	0.483	0.407

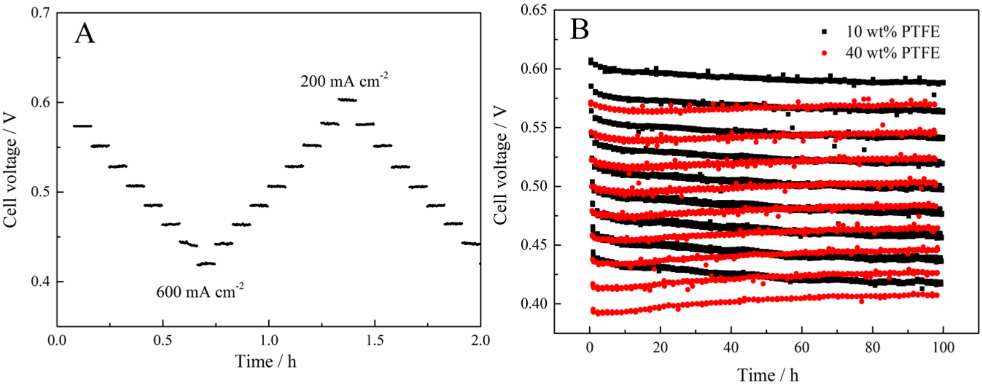

Figure 4.7: (A) Single cycles of the load cycling test; (B) voltage-time curves of the 10 wt.% and 40 wt.% PTFE cells during the 100 h operation.

The degradation rates of the cells operated after the 100 h aging + 100 h recovery are shown in Figure 4.8. Despite the voltage recovery of the 40 wt.% PTFE cell during the load cycling operation, the VDRs are still considerably higher than those of the 10 wt.% PTFE cell when the current density is higher than 300 mA cm^{-2}. These results demonstrate that the difference in the degradation rate is caused by the different PTFE contents of the CCLs.

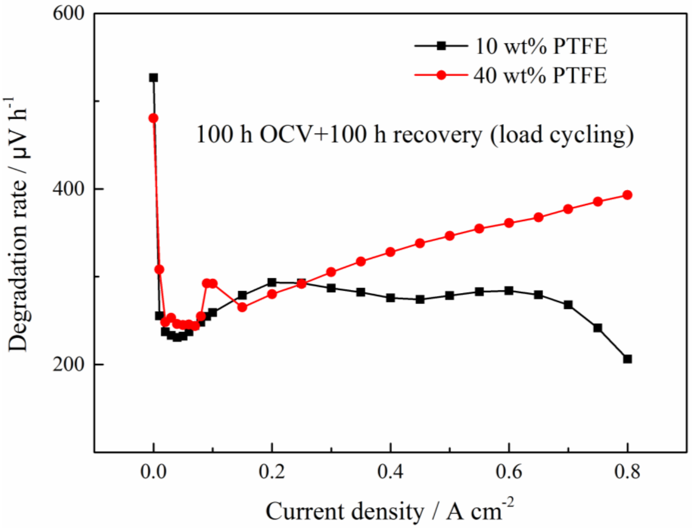

Figure 4.8: Degradation rate of the HT-PEFCs after the 200 h operation (100 h aging + 100 h recovery).

4.2. Load cycling test

4.2.1. Voltage-time curve

To further investigate the effect of PTFE content on the durability of HT-PEFCs, another two MEAs with different contents of PTFE are prepared. We can see in Table 4.2 that the two MEAs only differ in the PTFE content of the CCLs.

Table 4.2: Parameters of Low bind and High binder MEAs.

MEA	PTFE in CCL	PTFE in ACL	PA doping level
Low binder	0 wt.%	40 wt.%	15.5 mg cm^{-2}
High binder	60 wt.%	40 wt.%	15.5 mg cm^{-2}

The low-load cycling condition is applied as an effective stressor to accelerate the MEAs' degradation with the current density jumping between OCV and 200 mA cm^{-2} every 20 min, as shown in Figure 4.9A. The changes in voltages during the 100 h aging are recorded in Figure 4.9B. The Low binder and High binder MEAs exhibit the same OCV aging trend with the VDR of 220 µV h^{-1}, implying that the PTFE content has no effect on the PBI-based membrane during the low-load cycling test. However, the changes in voltages at 200 mA cm^{-2} of the Low binder and High binder MEAs are notably different. The degradation rate of the High binder MEA (620 µV h^{-1}) is almost twice that of the Low binder MEA (340 µV h^{-1}). This result is consistent with the 100h OCV aging test discussed above, i.e., the lower binder MEAs show lower performance degradation after the aging tests.

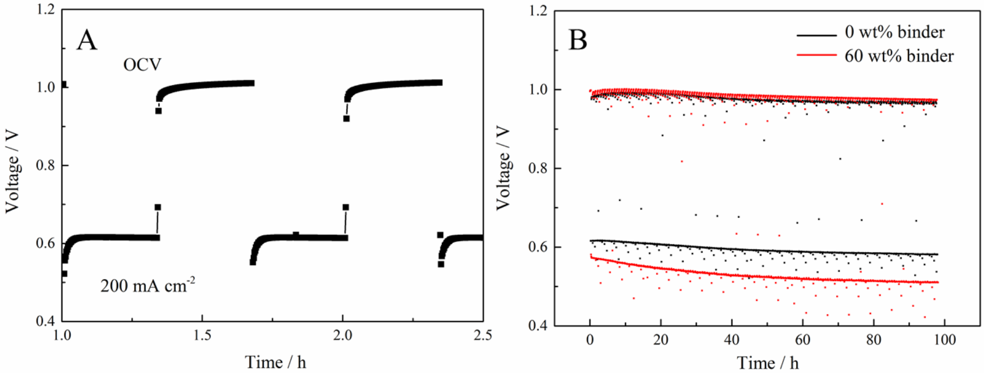

Figure 4.9: (A) Single cycles and (B) voltage-time curves of the 0 wt.% and 60 wt.% PTFE cells cycling between OCV (20 min) and 200 mA cm^{-2} (20 min) for 100 h at 160 ℃, H_2/air ($\lambda = 2/2$).

4.2.2. ICP-MS measurement

The PA leaching and Pt migration outside the HT-PEFCs are compared by the ICP-MS technology. In Table 4.3, the Low binder MEA shows a higher Pt loss than the High binder MEA (0.11 µg L^{-1} vs. 0.07 µg L^{-1}). This result agrees with the CV measurement of the OCV hold test that the lower binder MEAs exhibit higher Pt corrosion and more decrease in ECSA. Also, the Low binder MEA exhibits more severe PA leaching. This is probably due to the fact that the

PTFE network (supported by the SEM image in Section 3.3) can hold the impregnated PA in the CCL, leading to a decreased amount of PA leaching [32].

Table 4.3: Pt and PA concentrations in the water collected from cathode gas stream.

MEA	ICP-MS measurement	
	Pt loss	PA loss
Low binder	0.11 µg L^{-1}	1.59 µg mL^{-1}
High binder	0.07 µg L^{-1}	0.96 µg mL^{-1}

4.3. Summary

OCV and low-load cycling operations are used as effective stressors to investigate the effect of PTFE on the HT-PEFC durability.

- The PTFE binder plays a role in improving the stability of the Pt/C catalyst. However, the CCL with an excessive amount of PTFE presents a less porous and more compact structure and it is more susceptible to a mass transport problem caused by the factors, such as carbon corrosion/oxidation and PA flooding. After aging, the charge transfer resistance increases more in the low binder MEA, while the mass transport resistance increases more in the high binder MEA.
- In both the OCV and load-cycling tests, the negative effect on cells' performance is much greater than the positive effect by increasing the PTFE content in the CCLs.
- The impregnated PA in the CCL is trapped in the PTFE network, resulting in lower PA leaching in the higher binder MEA.

By considering the performance of the MEAs with different PTFE contents and the durability tests, 10-25 wt.% PTFE is advisable in the CCL.

5. Correlations between MEA parameters and electrochemical properties

In this chapter, 9 MEAs with different CCL parameters were prepared to optimize the MEA's performance as well as study the correlations between the MEA parameters and electrochemical properties. The EIS measurements were conducted with the help of Dr. Yasser Rahim. Parts of this work have been published [82] and an oral presentation was given at the 232nd ECS meeting, National Harbor, MD, October 2017.

Design of Experiments (DoE) is an effective method in statistical experiment planning and has significant advantages in terms of time and effort saved [113-115]. In this work, DoE methodology is applied to optimize the design parameters of MEAs, with all analyses performed with the software Statgraphics Centurion XVII.

5.1. Experimental plan

The experimental plan begins with the definition of response variables, including the voltage, ohmic resistance, cathode protonic resistance, charge transfer resistance, mass transport resistance, and capacitance. The second step is to define the experimental factors. As is shown in Table 5.1, three factors, i.e., CCL thickness, cathode Pt loading, and PA doping level with the continuous type are selected. Step three is to select the design. A two-level three-factor (2^3) full factorial design is chosen. As is shown in Table 5.2, a nine-run experimental plan is created with a middle point. The next step is to specify the model, with the two-factor interactions model selected. The statistical analysis is carried out using the regression analysis and the linear model of three factors including interactions are shown as follows [116]:

$$y = c_0 + c_1x_1 + c_2x_2 + c_3x_3 + c_4x_1x_2 + c_5x_1x_3 + c_6x_2x_3 \tag{5.1}$$

The last step is to evaluate the design using the DoE wizard. The Pareto chart (a bar chart sorted by frequency) and 3-D graphic are applied to present the results.

Table 5.1: List of factors and the investigated levels.

Serial	Factor	Unit	Code	Low level (−)	High level (+)
1	CCL thickness	μm	A	60	120
2	Cathode Pt loading	mg cm^{-2}	B	0.6	1
3	PADL	mg cm^{-2}	C	15	25

Table 5.2: Design matrix in standard order for a two-level three-factor full factorial (2^3) DoE.

MEAs	A: CCL thickness / μm	B: Pt loading / mg cm^{-2}	C: Doping level / mg cm^{-2}
MEA 1	−	−	−
MEA 2	+	−	−
MEA 3	−	+	−
MEA 4	+	+	−
MEA 5	−	−	+
MEA 6	+	−	+
MEA 7	−	+	+
MEA 8	+	+	+
MEA 9	90	0.8	20

5.2. Cathodes with different parameters

In the nine MEAs, all the anodes are the same with the Pt loading of 0.6 ± 0.05 mg cm^{-2}. The CCL thickness and cathode Pt loading were controlled by using different types of Pt/C catalysts, thicknesses of spacers and recipes. The high-level PADL (25 mg cm^{-2}) was achieved by adding extra 5 mg cm^{-2} PA on both ACL and CCL. The recipes for the preparation of the nine MEAs are shown in Table 5.3. Due to unavoidable experimental errors that occurred during the MEAs’ preparation processes, the MEAs indicate small differences between the planned and actual parameters, as shown in Table 5.4.

Table 5.3: Recipes for the preparation of the MEAs.

MEA ID	Pt/C / g	Catalyst type	Extra C / g	Water / mL	Solvent /mL	PTFE / µL	Spacer / cm
MEA 1	1.0	20 wt.% Pt	\	3.0	19.5	744	0.5
MEA 2	0.8	20 wt.% Pt	0.2	3.0	19.5	744	0.8
MEA 3	0.5	40 wt.% Pt	\	1.2	7.7	225	0.4
MEA 4	1.0	20 wt.% Pt	\	3.0	19.5	744	1.0
MEA 5	1.0	20 wt.% Pt	\	3.0	19.5	744	0.5
MEA 6	0.8	20 wt.% Pt	0.2	3.0	19.5	744	0.8
MEA 7	0.5	40 wt.% Pt	\	1.2	7.7	225	0.4
MEA 8	1.0	20 wt.% Pt	\	3.0	19.5	744	1.0
MEA 9	1.0	20 wt.% Pt	\	3.0	19.5	744	0.8

Table 5.4: The planned and actual physical parameters of the MEAs.

MEA ID	Planned CCL thickness / µm	Actual CCL thickness / µm	Planned Pt loading / mg cm^{-2}	Actual Pt loading / mg cm^{-2}	Planned doping level / mg cm^{-2}	Actual doping level / mg cm^{-2}
MEA 1	60	62	0.6	0.58	15	14.5
MEA 2	120	120	0.6	0.62	15	14.5
MEA 3	60	51	1	0.93	15	15.5
MEA 4	120	130	1	1.0	15	15.0
MEA 5	60	70	0.6	0.62	25	24.3
MEA 6	120	110	0.6	0.58	25	24.5
MEA 7	60	55	1	1.0	25	24.5
MEA 8	120	125	1	0.95	25	24.5
MEA 9	90	93	0.8	0.77	20	20.1

5.3. HT-PEFCs voltage

The polarization curves with stoichiometries of (H_2/air) 2/2 and 2/6 of the nine home-made MEAs are depicted in Figure 5.1. In Figure 5.1A with a low air stoichiometry in the cathode, the performance can be roughly divided into two parts that MEAs 3, 5, 7 and 8 demonstrate worse performance than the other cells. One thing should be noted that, with the exception of MEA 3, MEAs 5, 7 and 8 all have the high PADL of 25 mg cm^{-2}. Moreover, MEA 7 with a high Pt loading, low thickness and high PADL shows a pronouncedly worse electrochemical performance. This is explained by a severe PA flooding effect, resulting in blockage of the porous structures and ‘dead’ of part of the Pt catalyst.

Figure 5.1B shows the polarization curves of the MEAs with a high air stoichiometry. It can be seen that, with the exception of MEA 7, the MEAs exhibit comparable performance. These results indicate that a high flow rate of air can significantly improve the performance of the MEAs with high PADL. The voltage at 200 mA cm^{-2} with the stoichiometry of 2/2 is used as a response variable for the DoE design matrix and analyzed by the software Statgraphics.

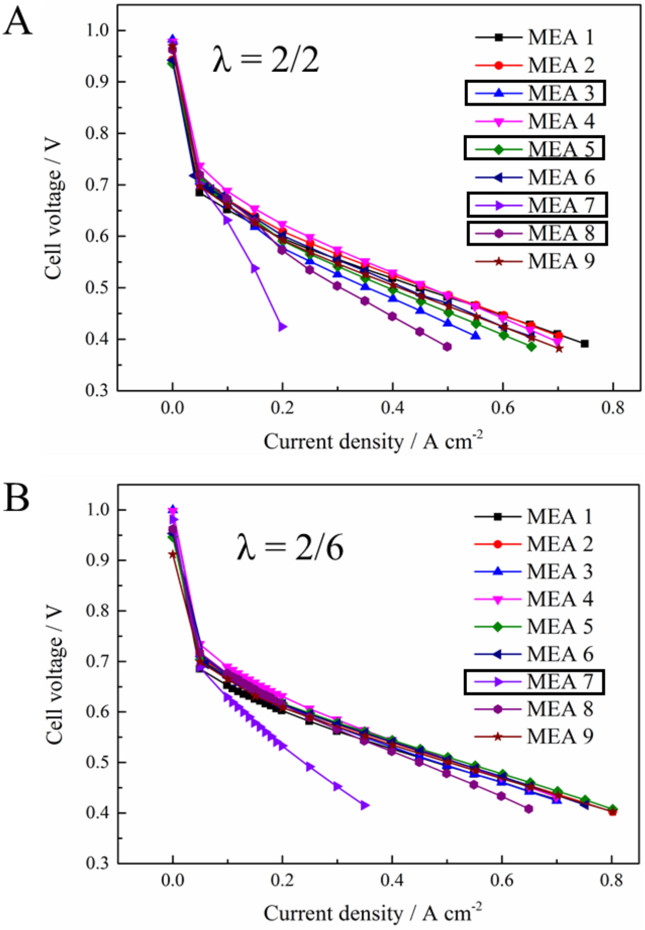

Figure 5.1: Polarization curves of the home-made MEAs tested at 160 ℃ with λ H_2/air = (A) 2/2 and (B) 2/6 after the break-in procedure.

Figure 5.2 shows the 3-D graphic of the voltage obtained at 200 mA cm^{-2} with λ H_2/air = 2/2. Clearly, the voltage is strongly influenced by the investigated factors. The red region means a high voltage with the setting values of the factors. It is worth noting that the MEA (MEA 6) with the value of CCL thickness 120 μm, Pt loading 0.6 mg cm^{-2} and PADL 25 mg cm^{-2} exhibits the same voltage with the MEA (MEA 4) of CCL thickness 120 μm, Pt loading 1.0 mg cm^{-2} and

PADL 15 mg cm^{-2}. This result implies that the Pt utilization can be increased by adjusting the CCL thickness and PADL. Martin et al. reported that the performance of HT-PEFCs increases as the Pt/C ratio decreases. This enhancement is attributed to a better dispersion of the catalyst and a less severe PA flooding effect in the CCL [117]. As is shown in Table 5.3, extra carbon is added in the commercial 20 wt.% Pt catalyst that is used in MEA 6. The ratio of the Pt/C catalyst in MEA 6 is lower than that of MEA 4 (0.2 vs. 0.25). More details will be discussed later by using the EIS results. Another point of interest is that the MEA (MEA 7) with CCL thickness of 60 μm, Pt loading of 0.6 mg cm^{-2} and PADL of 25 mg cm^{-2} shows the lowest voltage at around 0.5 V. This agrees with the results of the polarization curves discussed above, in which the MEA exhibits the worst performance.

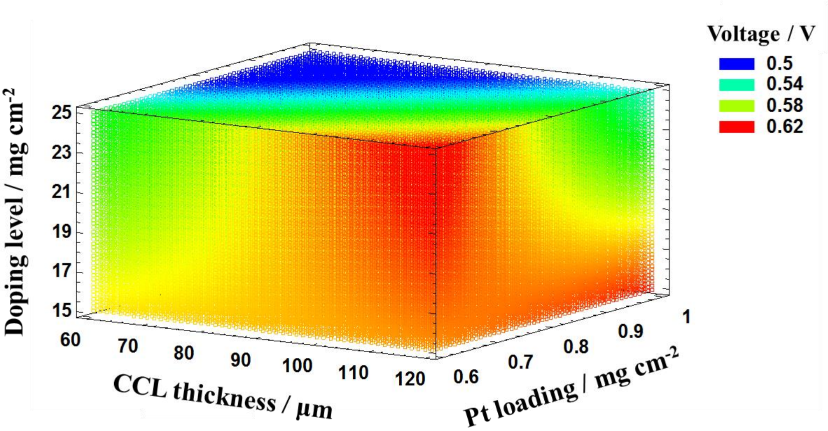

Figure 5.2: 3-D graphic of the voltage recorded at 200 mA cm^{-2} with λ H_2/air = 2/2.

Pareto chart is one of the most commonly used graphical options to reflect the importance of factors and their interactions in experimental design. Figure 5.3 shows the Pareto chart of the voltage obtained at 200 mA cm^{-2} with λ H_2/air = 2/2. All of the three factors exhibit notable influences on the voltage. We can see that the voltage is positively affected by the CCL thickness, with a voltage increase of above 50 mV by increasing the CCL thickness from 60 to 120 μm. In addition, the interactions related to the CCL thickness (A) show beneficial influences on the voltage. These results suggest that the cell voltage increases as the CCL thickness increases. One thing should be noted that all the MEAs are in a relatively high PADL from 15 to 20 mg cm^{-2}. Therefore, a larger thickness of the CCL could lead to a better distribution of PA, ultimately resulting in increased performance. The other two factors (Pt loading and PADL） exhibit substantially negative effects on the cell's voltage, with voltages decrease of above 50 mV. Furthermore, the interaction factor of BC is another pronounced factor that causes a decrease in the cell's voltage.

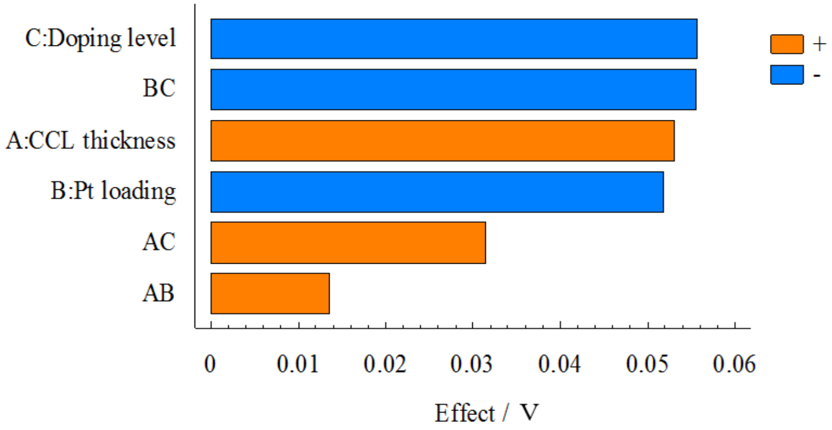

Figure 5.3: Pareto chart of the voltage obtained at 200 mA cm^{-2} with λ H_2/air = 2/2.

5.4. Resistances

The Nyquist plots of the MEAs were recorded at 100 mA cm^{-2}, T = 160 ℃, as shown in Figure 5.4. The EIS data were fitted by the established equivalent circuit in Section 1.3. The ohmic resistance (R_{Ω}), cathode protonic resistance (R_P), charge transfer resistance (R_{ct}), mass transport resistance (R_m) and cathode capacitance (C_{dl}) were calculated, and finally the parameters were used as response variables and analyzed by the software Statgraphics.

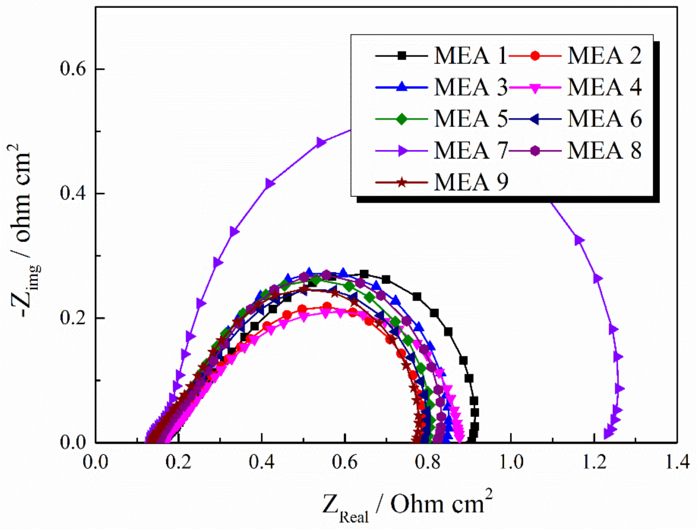

Figure 5.4: EIS plots of the home-made MEAs tested at 100 mA cm^{-2} and fitted using the equivalent circuit discussed in Section 1.3, T = 160 ℃.

5.4.1. Ohmic resistance

Figure 5.5 shows the 3-D graphic of the MEAs' R_Ω. It is clear that the R_Ω decreases from the bottom to top, signifying that R_Ω can be reduced by increasing PADL. This is because that R_Ω is mainly dominated by the membrane resistance. A high PADL helps to accelerate the structural diffusion of protons in the membrane via the Grotthuss mechanism and vehicle mechanism [118, 119]. The lowest R_Ω exists in MEA 7 with the planned setting parameters of CCL thickness 60 μm, Pt loading 1.0 mg cm^{-2}, and PADL 25 mg cm^{-2}, which is due to the high PADL and a smaller actual CCL thickness (54 um).

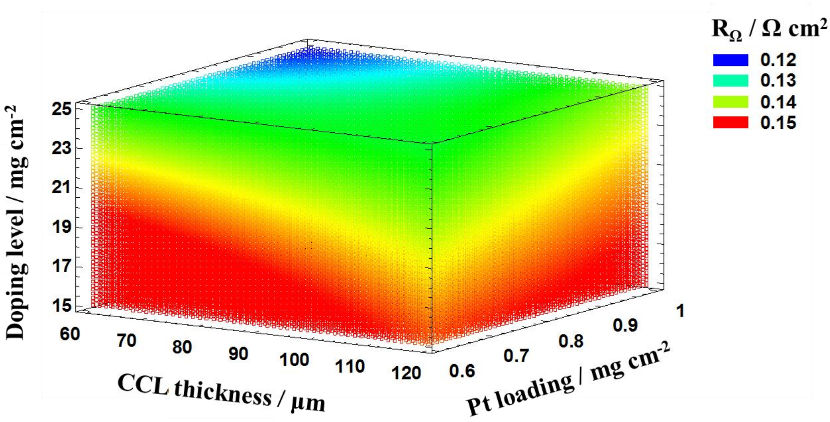

Figure 5.5: 3-D graphic of ohmic resistance values of the MEAs.

In the Pareto chart for R_Ω (Figure 5.6), as expected, the PADL is the most dominant factor in reducing R_Ω. The value decreases approximately 0.02 Ω cm^2 by increasing the PADL from 15 to 25 mg cm^{-2}. Also, the other two factors, i.e., CCL thickness and Pt loading, have positive impacts of lowering the R_Ω. The two-factor interaction of the CCL thickness and Pt loading is the most important factor in enhancing the R_Ω.

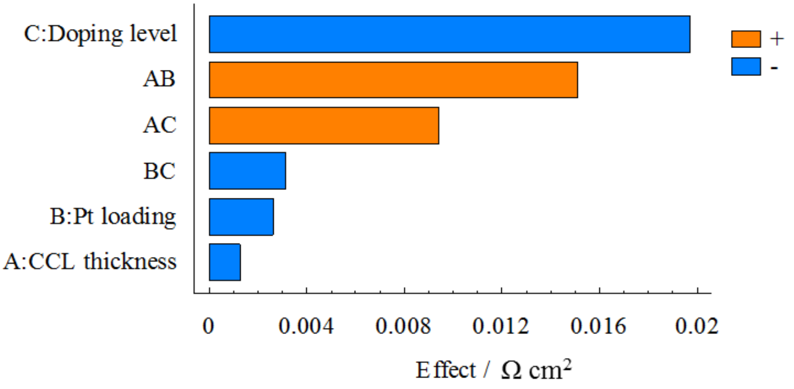

Figure 5.6: Pareto chart for the ohmic resistance.

5.4.2. Protonic resistance

The cathode protonic resistance of the nine MEAs is depicted in Figure 5.7. Similar to R_Ω, R_P is mainly determined by the PADL, and a high PADL is good for reducing R_p. We can see that the R_P value decreases approximately from 0.15 Ω cm^2 to 0.12 Ω cm^2 by increasing the PADL from 15 mg cm^{-2} to 25 mg cm^{-2} in the MEAs.

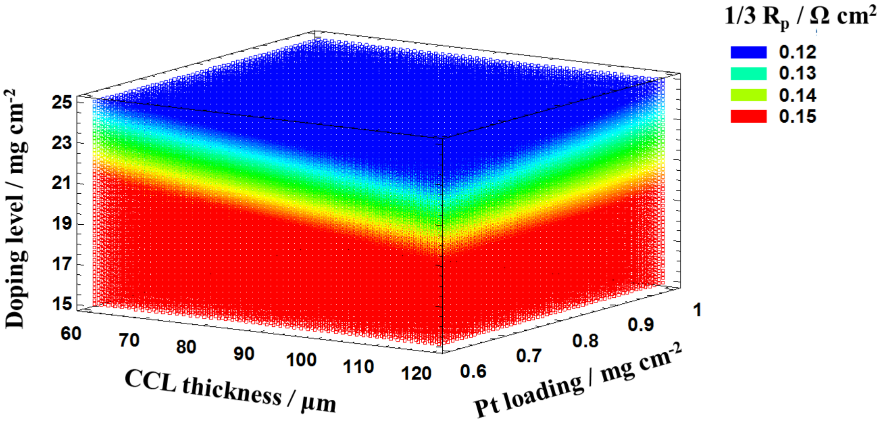

Figure 5.7: 3-D graphic of cathode protonic resistance values of the MEAs.

The Pareto chart for the cathode protonic resistance of the MEAs is shown in Figure 5.8. The PADL has the greatest impact on the R_p. This is reasonable that R_p is mainly dominated by the diffusion of protons in the CCL. A high PADL means a high content of PA in the CCL, thus leading to a decrease in R_p. In addition, the Pt loading is the second factor in reducing the R_p, while the other factors more or less adversely affect the R_p.

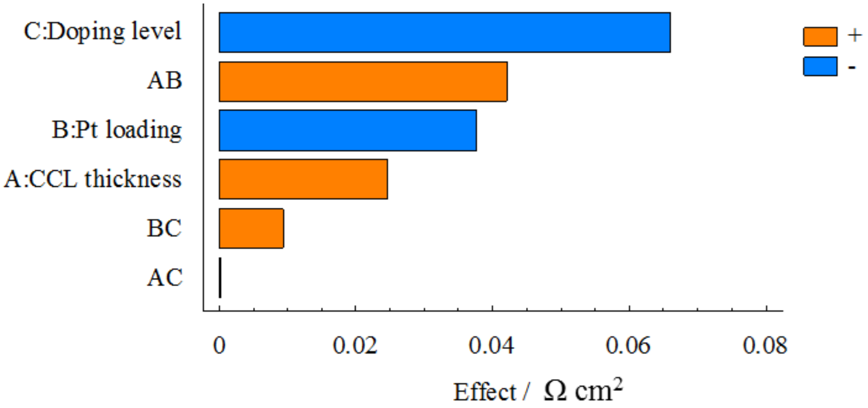

Figure 5.8: Pareto chart for the cathode protonic resistance.

5.4.3. Charge transfer resistance

The 3-D graphic of the charge transfer resistance of the MEAs is shown in Figure 5.9. The R_{ct} of the PA/Pt interface is inversely proportional to the exchange current density of the ORR, which, in turn, is proportional to the number of reaction sites, termed as Triple-Phase Boundary (TPB) [120]. This explains that MEA 8 exhibits the lowest R_{ct}. The high Pt loading (1.0 mg cm^{-2}) and PADL (25 mg cm^{-2}) result in forming more TPBs than the other MEAs, and thus the lowest R_{ct}. In the graphic, the two corners shown in red indicate the corresponding two MEAs with the highest R_{ct}. One is MEA 1 with the setting parameters of CCL thickness 60 µm, Pt loading 0.6 mg cm^{-2} and PADL 15 mg cm^{-2}. By the same token, the high R_{ct} is caused by reduced amounts of TPBs. The other one is MEA 7. As discussed above, a severe mass transport problem occurs due to the high PADL and small actual CCL thickness. Parts of the CCL are flooded in this case, and the flooded parts would be more or less “dead” because of the small O_2 concentration, leading to reduced TPBs and ultimately a strongly increased R_{ct}.

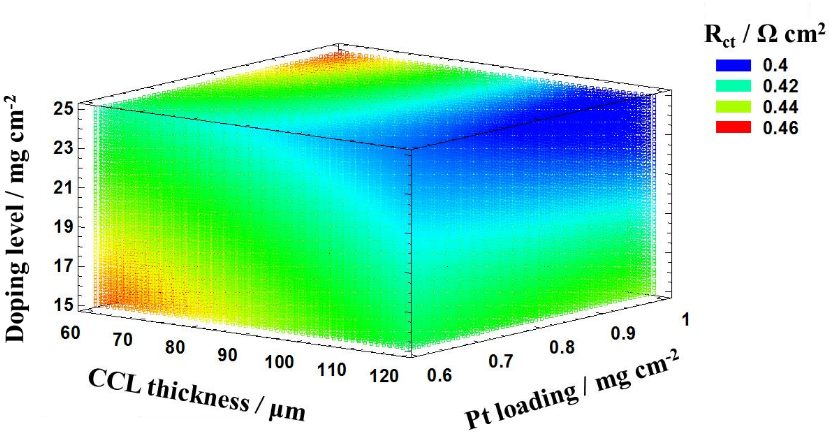

Figure 5.9: 3-D graphic of charge transfer resistance values of the MEAs.

Figures 5.10 shows the Pareto chart for the charge transfer resistance. Factor A and C are the most important factors in reducing the R_{ct}. A larger CCL thickness contributes to the PA distribution, leading to a decreased mass transport resistance and thus an enhanced oxygen concentration; a higher PADL can definitely increase the numbers of TPBs and exchange current density. We can see that these two factors are contradictory to some extent, so a proper CCL thickness and PADL are essential for reducing the R_{ct} of ORR. In addition, the two-factor interaction between the CCL thickness and Pt loading has a strong impact in reducing the R_{ct}. The factor Pt loading shows a less significant effect on the R_{ct}. This is probably due to the large Pt loading range investigated.

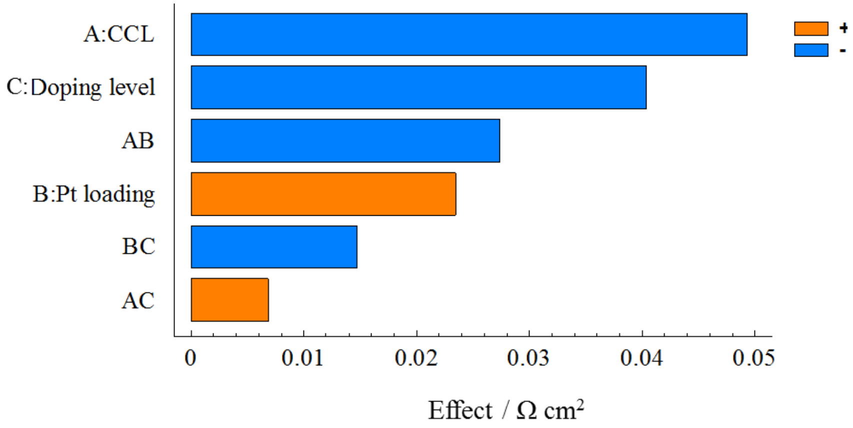

Figure 5.10: Pareto chart for the charge transfer resistance.

5.4.4. Mass transport resistance

Figure 5.11 shows the 3-D graphic of the mass transport resistance of the MEAs. The blue part presents the lowest R_m around 0.03 Ω cm^2. MEA 2 and MEA 6 with the same CCL thickness (120 μm) and Pt loading (0.6 mg cm^{-2}) have the lowest R_m. As discussed previously, a lower ratio of Pt/C ratio in the CCL contributes to a better dispersion of the catalyst and a less severe PA flooding effect in the CCL; MEA 2 and 6 have the lowest Pt/C ratio of 0.2, thus leading to the smallest R_m value.

It is clear that the highest R_m exists in MEA 8 that has the CCL thickness of 120 μm, Pt loading of 0.6 mg cm^{-2}, and PADL of 25 mg cm^{-2}. This observation can be explained by a) the PA flooding effect may occur in the CCL due to the high PADL; b) the distance of gas transport to TBPs increases because of the large CCL thickness.

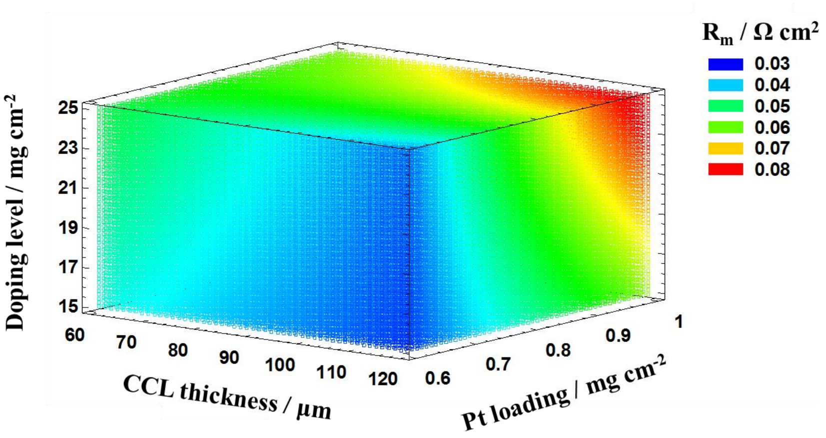

Figure 5.11: 3-D graphic of mass transport resistance values of the MEAs.

The Pareto chart for the mass transport resistant of the MEAs is shown in Figure 5.12. With the exception of the two-factor interaction between the CCL thickness and PADL, all the other factors lead to an increase in R_m. Among the factors, the interaction between the CCL thickness and Pt loading is the most significant factor in increasing the R_m. In addition, the rises in Pt loading and PADL are the next factors that cause a mass transport problem.

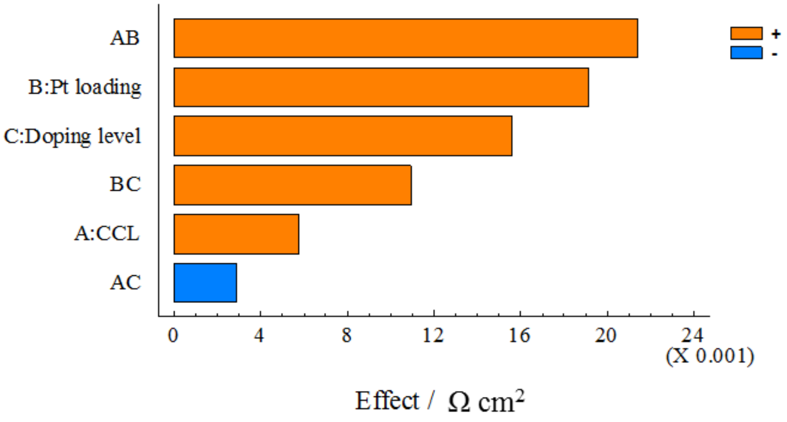

Figure 5.12: Pareto chart for the mass transport resistance.

5.4.5. Double layer capacitance

The input parameters affecting the output response of double layer capacitance is performed, as shown in Figure 5.13. Since C_{dl} is determined by the wetted surface area of the Pt/C catalyst in the CCL, a higher C_{dl} is commonly used as an indicator of a higher ECSA [121]. It is clear that MEA 8 with a high level of CCL thickness, Pt loading and PADL exhibits the greatest C_{dl}, signifying the largest value of ECSA. The lowest C_{dl} (the blue corner) exists in MEA 2, with a low level of Pt loading and PADL, leading to a small contacting area between the Pt/C catalyst and PA. Accordingly, a high Pt loading and PADL help increase the C_{dl} at the cathode.

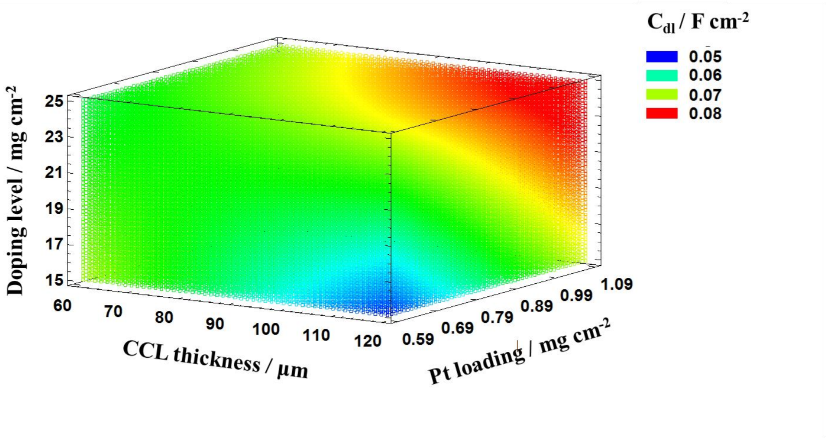

Figure 5.13: 3-D graphic of double layer capacitance values of the CCLs

As shown in the Pareto chart for the double layer capacitance of the cathode, the interaction between the CCL thickness and doping level plays the most important role in increasing the C_{dl}; the Pt loading and PADL help increase the C_{dl} as expected. Moreover, the CCL thickness negatively affects the C_{dl}. This is probably explained that the ORR mainly takes place on the Pt catalyst particles close to the membrane and a large CCL thickness could lead to decreases in the concentrations of Pt and PA close to the membrane, thus leading to a reduction of the C_{dl}.

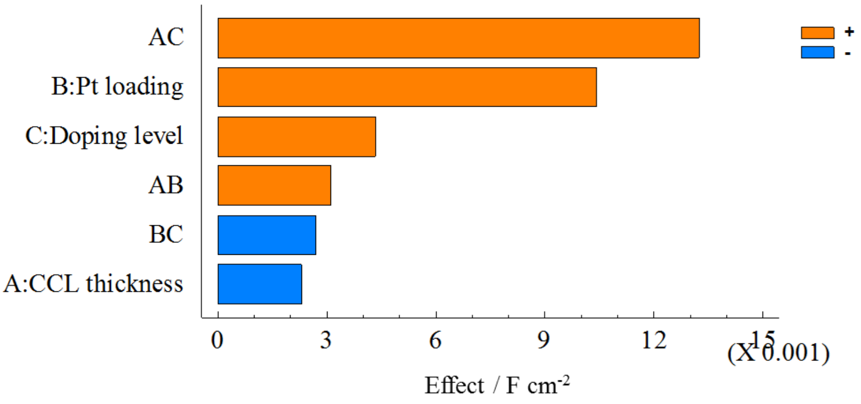

Figure 5.14: Pareto chart for the double layer capacitance of the cathode.

5.5. Summary

In this chapter, a two-level factorial with three factors experiment is planned by utilizing the DoE method. The cell voltage and cell resistance from EIS are considered as the response variables. Among the MEAs, MEA 6 shows the attractive characteristics with a high voltage and low Pt loading. According to the results above, this is attributed to:

- The high PADL reduces the R_{Ω} and R_p.
- The high PADL helps to increase the TPBs, leading to a decrease in the R_{ct}.
- The extra carbon in the CCL decreases the Pt/C ratio, which is good for the PA distribution; therefore, there is only a relatively small increase in the R_m by increasing the PADL.

The investigated factors, i.e., Pt loading, thickness of CCL and PADL have strong interactions and the two-factor interactions have significant effects on the changes in all the response variables. The PADL is a critical factor in the HT-PEFC’s performance and it is should be noted that the selected range of the PADL is at a relatively high level (larger than 15 mg cm^{-2}). This work provides a direction for the preparation of the MEA with a high PADL: using the catalyst with a low Pt/C ratio and relatively high CCL thickness to better distribute the Pt catalyst as well as alleviate the PA flooding effect, thereby increasing the Pt utilization efficiency in the CCL.

In the opposite direction, the MEA in a low PADL range is not studied in this work. It is assumed that in this case, the thickness of CCL should be reduced and the interactions among these factors can be different.

6. Study of Pt bands formation and Pt/C degradation in HT-PEFCs

In HT-PEFCs, Pt dissolution and precipitation become more complicated due to the enhanced Pt/C catalyst degradation kinetics. However, several aspects, including the mechanism of Pt band formation in the PBI-based membrane, have not been well studied. In this chapter, a 200 h constant operation (first 100 h hold at 200 mA cm^{-2} and the second 100 h at OCV) is applied to HT-PEFCs and extensive characterizations are conducted to investigate the degradation behavior in the MEA. The work has been published in *Electrochimica Acta* [59], which is used with permission from the Copyright Clearance Center.

6.1. Operating procedure

Two identical MEAs were prepared with the Pt loadings of 0.6 ± 0.05 and 1.1 ± 0.05 mg cm^{-2} at the anode and cathode, respectively. The 5032Z PTFE was used as the binder in both sides with the content of 40 wt.%. The PADL was controlled at 15.0 ± 1.0 mg cm^{-2}. During the tests, the temperature was kept at 160 ℃. Non-humidified pure hydrogen and air were purged in the anode and cathode, respectively, with a stoichiometry of 2/2. As shown in Figure 6.1, the new MEA is run 70 hours at a constant current density of 200 mA cm^{-2} as an initial activation (break-in procedure). Then, the new MEA is characterized by FIB/SEM tomography. Another MEA, termed aged MEA, is first subjected to the break-in process and following tested for another 200 h (the first 100 h at 200 mA cm^{-2} and second 100 h at OCV).

There is no significant degradation of the aged MEA during the 100 h operation at 200 mA cm^{-2}. An approximately stable degradation rate of 160 μVh^{-1} is observed during the second 100 h operation under the OCV condition. The aged MEA is interrupted to perform polarization curves, cyclic voltammetry (CV) and electrochemical impedance spectroscopy (EIS) measurements three times after break-in, 100 h and 200 h, respectively. Finally, it is also visualized by FIB/SEM tomography.

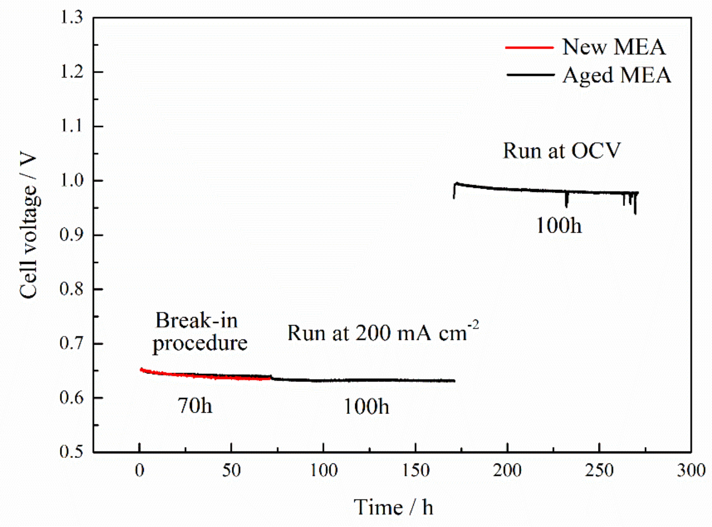

Figure 6.1: Cell voltage variation during the running time of the new MEA and aged MEA [59].

6.2. Electron microscopy characterizations

6.2.1. SEM-EDX mapping analysis

The cross-sectional SEM image and EDX mapping are applied to determine Pt distribution in the new MEA. We can see in Figure 6.2A that a bright area appears at the interface of the membrane and the cathode. In the EDX mapping images of the elements Pt, C and F, a band only exists in the Pt map (Figure 6.2B). These results evidently demonstrate that the bright area is ascribed to the agglomeration of Pt particles. The phenomenon is unexpected, as the new MEA is only experienced a standardized break-in procedure. In LT-PEFCs, Pt bands are formed by using accelerated stressors [74, 122], but there is no observation of Pt band under normal testing conditions (e.g., constant running at 200 mA cm^{-2}). The presence of the Pt band implies exacerbated degradation of the Pt/C catalyst in HT-PEFCs.

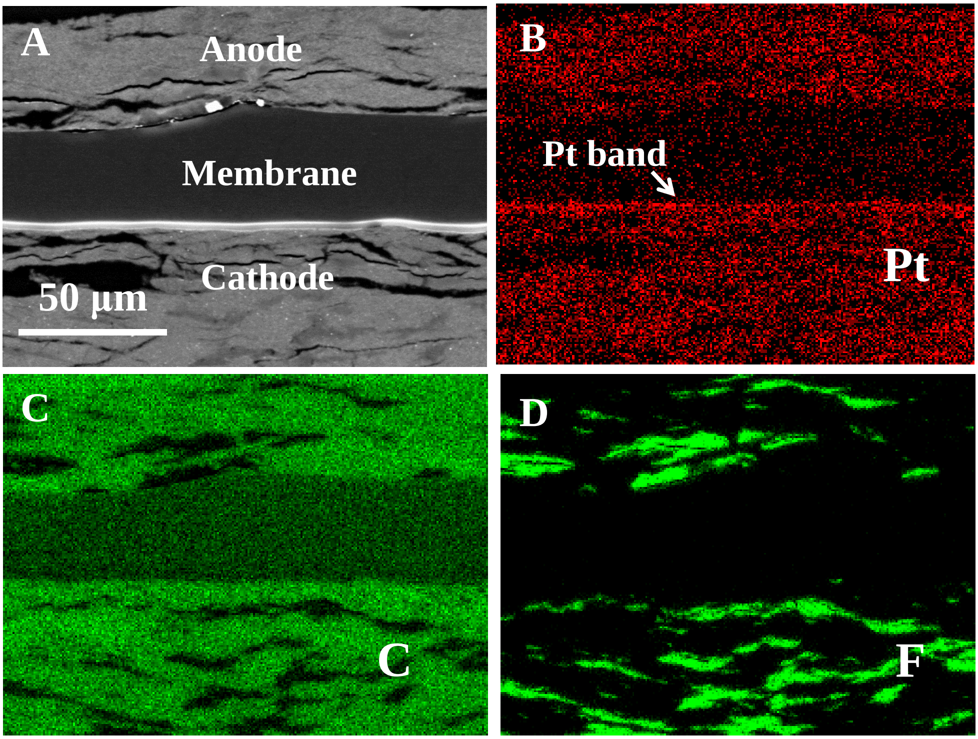

Figure 6.2: (A) SEM cross-sectional image of the new MEA; EDX mapping images of elements (B) Pt; (C) C; and (D) F [59].

To further investigate the Pt band formation in the new MEA, elemental analysis is performed in boxes from the ACL to the CCL along the lateral region of the Pt band, as shown in Figure 6.3A. For the Pt band region, EDX analysis is conducted at random points instead of the box region due to the narrowness and waviness of the band. In the EDX line-scan profile of Pt, a sharp increase in Pt intensity is observed at the interface of the membrane/cathode. Figure 6.3B presents the SEM cross-sectional image of a fresh GDE. The average Pt mass% in the fresh catalyst layer is determined in the black box region. The average values of the Pt mass% in the anode, membrane, Pt band, cathode and fresh CCL (dashed line) are depicted in Figure 6.3C. Compared to the Pt mass% in the fresh GDE (3.7), it is clear that the Pt mass% of the anode does not change (3.7), the Pt mass% in the middle of the PBI-based membrane is zero and the Pt mass%

sharply increases at the band area and obviously decreases in the CCL. What is more, the Pt mass% decreases more in the region closer to the membrane. These results illustrate that Pt particles move from the CCL to the membrane/cathode interface during the break-in process.

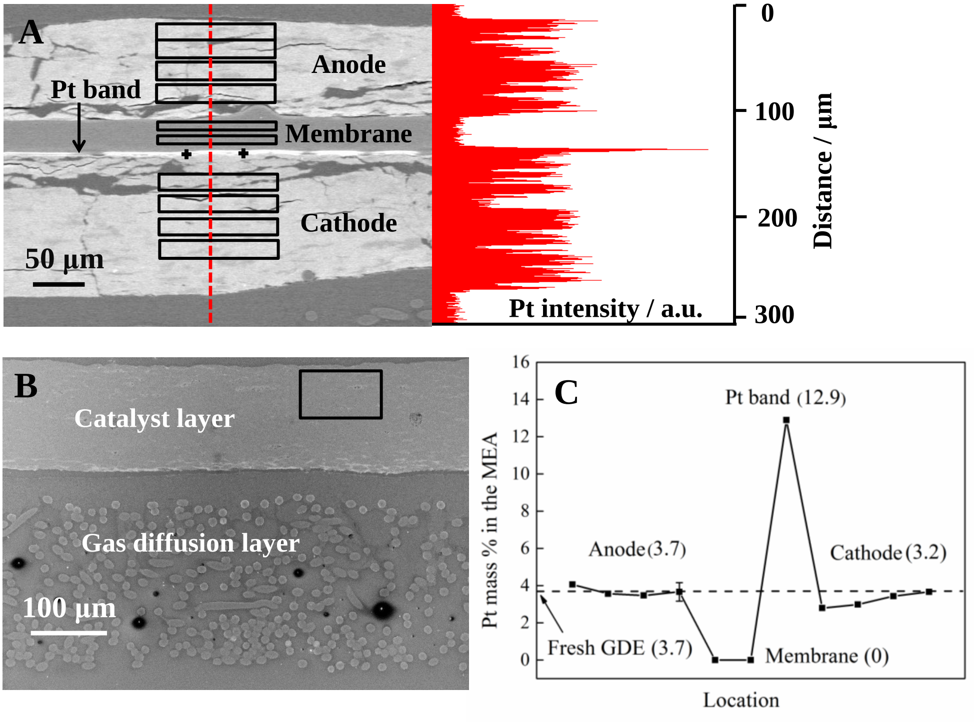

Figure 6.3: (A) SEM cross-sectional image (left) and EDX line-scan profile (right) of the new MEA; (B) SEM cross-sectional image of the fresh GDE; (C) Pt mass% at different locations in the MEA. The error of the EDX analysis on Pt is indicated by the error bar (within ± 0.5%) [59].

6.2.2. FIB/SEM measurement

The focused ion beam coupled SEM (FIB/SEM) system is applied for a detailed investigation of the Pt precipitation behavior at the interface. Figure 6.4 presents the SEM images of the (A) new

MEA and (B) aged MEA on the anode sides after the FIB milling. We can see that there is no notable Pt agglomeration in the ACL and no Pt precipitation in the membrane due to the low anode potential (close to 0 V vs. the reversible hydrogen electrode) [123, 124]. In addition, fuel starvation cannot occur, as pure hydrogen is served as the anode gas with a stoichiometry of 2. Hence, Pt/C catalyst corrosion on the anode side is avoided in the new MEA.

The membrane at the interface of the new MEA is flat. After the 200 h aging process, the interface of anode/membrane becomes distorted, indicating the membrane degradation. During the OCV operation, a considerable membrane thinning occurs due to the dehydration process, which leads to an increase in the amount of cross-leaking O_2. Thereby, hydrogen peroxide is formed at the ACL through Equation (1.11) [63, 125, 126]. Ultimately, radicals (•OH) are generated via the Fenton's reaction, which has been proven to be detrimental to the membrane [62, 125]:

$$H_2O_2 + Fe^{2+} \rightarrow \bullet OH + OH^{-} + Fe^{3+} \qquad (6.1)$$

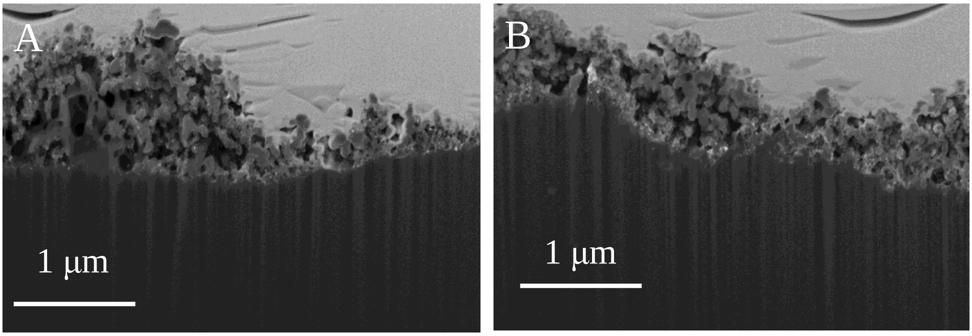

Figure 6.4: SEM cross-sectional images on the anode sides of the (A) new and (B) aged MEAs after FIB milling [59].

Further insights into the Pt band formation are provided by the SEM cross-sectional images of the FIB-milled CCL. We can see in Figure 6.5A that a Pt line (band) presents in the membrane of the new MEA about 1.5 µm from the cathode/membrane interface. In the FIB/SEM image of the aged MEA (Figure 6.5B), two clear Pt bands appear with small Pt particles distributed between them. By comparing the two images, the position of the Pt band below in the aged MEA is not exactly the same as that in the new MEA. Presumably, this is caused by the deviation (±0.5 mg cm^{-2}) of the PADL in these two MEAs. Different PADLs cause different amounts of H_2 dissolution and H_2 cross-leakage through the membrane, thus resulting in slightly different positions of the Pt bands [127].

Furthermore, by comparing the magnified SEM images of the first band in Figure 6.5C and D (red boxes in Figure 6.5A and B), it can be seen that the Pt band is strengthened and the number of larger Pt particles increases after aging. This is ascribed to the Pt/C catalyst corrosion and migration during the first 100 h running at 200 mA cm^{-2}. The second Pt band is considered to be formed under the OCV condition, which shifts closer to the CCL within 0.5 μm from the cathode/membrane interface. These observations imply that the position of a Pt band is influenced by the operating conditions, which will be discussed in the next section. Figure 6.5E and F exhibit magnified images of the CCLs of the new and aged MEAs (orange boxes in Figure 6.5A and B), respectively. In the SEM image of the new MEA, there are no visualizable Pt particles. After the aging process, a number of Pt agglomerations appear on the CCL. The growth of Pt particles involves the Pt dissolution and redeposition processes, known as the Ostwald ripening mechanism[51].

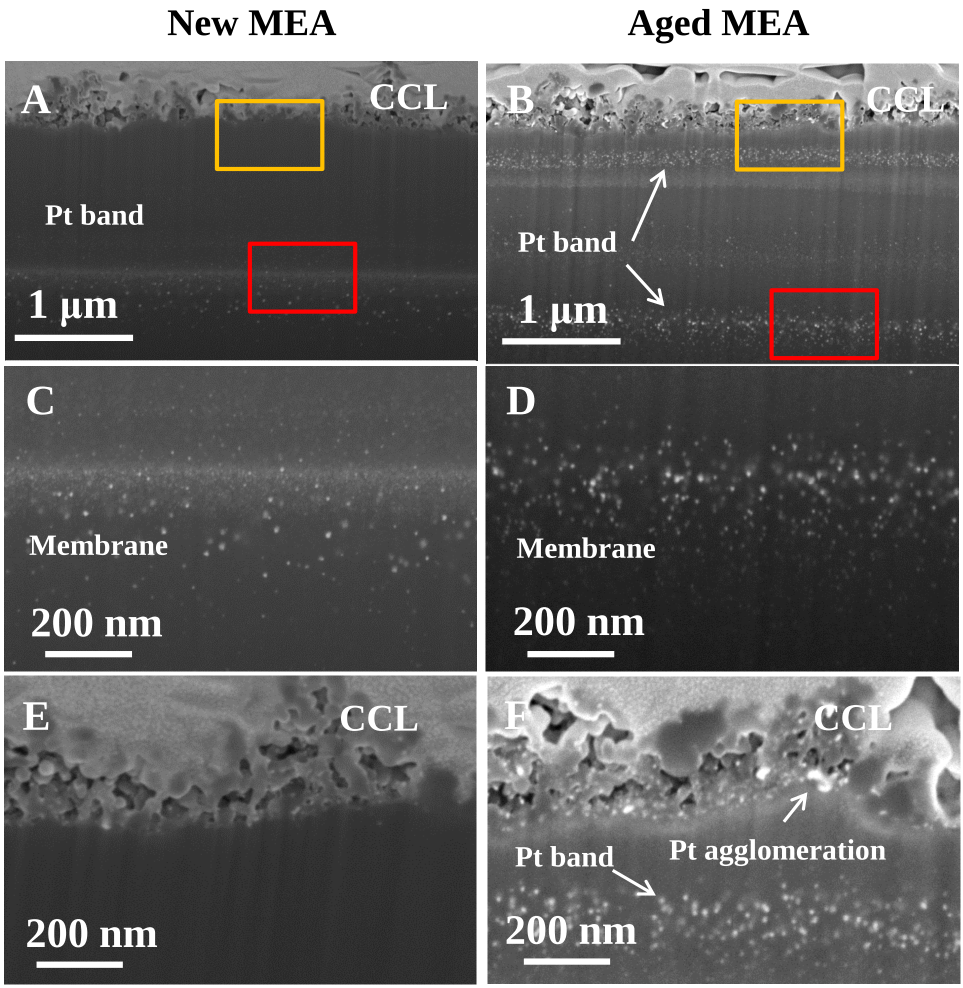

Figure 6.5: SEM cross-sectional images of FIB-milled CCLs: (A) New MEA and (B) aged MEA; (C) and (D) Magnified images of the first band (red boxes in Figure 6.5A and B); (E) and (F) Magnified images of cathode catalyst layers (orange boxes in Figure 6.5A and B) [59].

6.3. Mechanism of Pt band formation

The mechanism of the Pt band formation in the new MEA is described as follows: As the kinetics for the corrosion of Pt nanoparticles is accelerated at higher temperatures and the more acidic environment in HT-PEFCs, Pt dissolution occurs during the break-in process [128]. Next, the formed Pt ions move towards the membrane due to a concentration difference. Finally, the Pt ions (Pt^{z+}) react with the cross-leaking H_2 molecules, resulting in a clear Pt band within the membrane. The reaction equation is presented in Equation (6.2):

$$Pt^{z+} + z/2H_2 \rightarrow Pt + zH^+ \tag{6.2}$$

To account for the change in the position of the second Pt band, LSV measurements were conducted to quantify the changes in hydrogen crossover during the OCV operation. As is shown in Figure 6.6A, an HT-PEFC was held at OCV for 100 h and interrupted by the LSV tests at 0h, 3h, 7.5h, 23h, 46h, and 100h, respectively. At each time, the cathode gas was switched from air to nitrogen without shutting down the test rig. After 20 minutes purging, the air was almost substituted by nitrogen in the cathode and afterward the LSV measurement was performed. The LSV curves are depicted in Figure 6.6B. According to Equation (1.28), the limiting crossover current density (j_l) and internal short-circuit resistance ($R_{internal\ short}$) are calculated at each interruption during the OCV hold test.

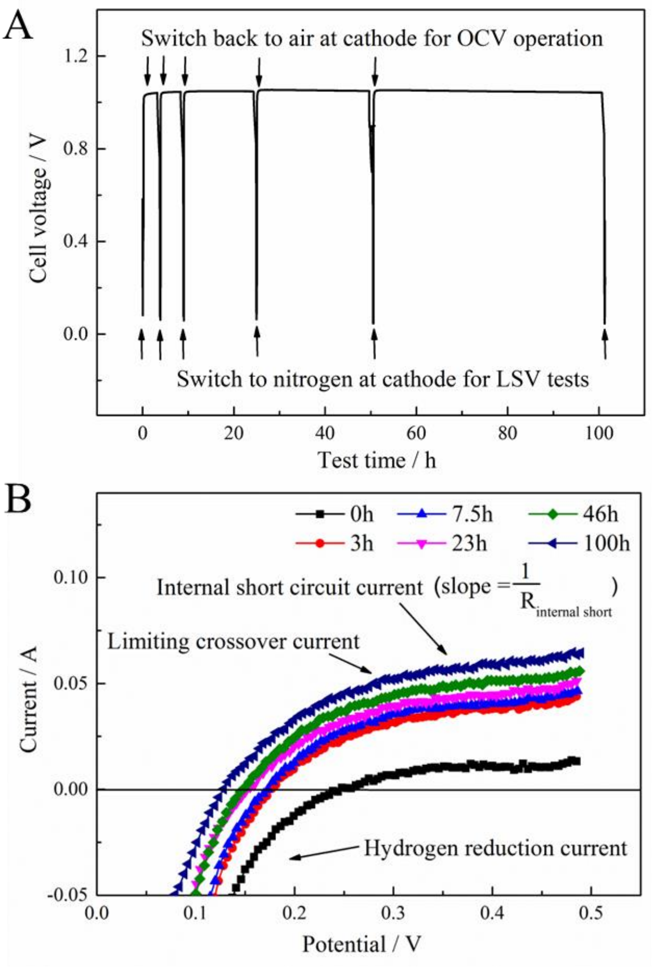

Figure 6.6: (A) Cell voltage variation of the LSV tests during 100h OCV operation; (B) LSV curve of the MEA at each time with a scan rate of 5 mV S^{-1} from 0.05 V to 0.5 V, T=160 ℃ [59].

As is shown in Table 6.1, the j_l rises significantly from 0.76 to 1.72 mA cm^{-2} after the first 3 hours OCV operation. This is probably caused by the thinning of the membrane due to the PA dehydration under the currentless condition [105]. Furthermore, the membrane thinning effect may cause a small portion of the cathode to come into contact with the anode, leading to a finite internal electronic short [106, 129, 130]. As a result, the $R_{internal\ short}$ drops sharply from 2325.58 to 24.75 Ω within the first 3 h of OCV operation.

After 3 h, the increasing trend of j_l slows down, which implies that the membrane is slightly degraded and no macroscopic pinhole is formed [131]. From 3 h to 100 h, the $R_{internal\ short}$ value almost stays constant, suggesting that the membrane thinning process is completed within the first 3 h OCV aging. Based on these results, the membrane thinning and increased hydrogen crossover are the possible reasons that lead to the shift of the second Pt band closer to the interface.

Table 6.1: Hydrogen crossover current density and internal short-circuit resistance.

Operation time / h	j_l / mA cm^{-2}	$R_{internal\ short}$ / Ω	Fitting error / %
0	0.76	2325.58	±0.35
3	1.72	24.75	±0.41
7.5	1.79	23.96	±0.34
23	1.92	23.49	±0.27
46	2.14	25.95	±0.28
100	2.46	19.62	±0.33

According to the discussion above, a schematic diagram of the Pt bands formation in the membrane is presented in Figure 6.7. The first Pt band (area 1, A1) is formed during the break-in process, which is strengthened after the first 100 h running at 200 mA cm^{-2}. Then, the load is switched to OCV and kept for another 100 h. Within the first 3 h OCV operation, dispersed Pt particles precipitate in A2 while the membrane thickness is changing. From the time the membrane approaches a steady condition to the end of the OCV hold test, the second Pt band is formed in region A3 closer to the membrane/cathode interface.

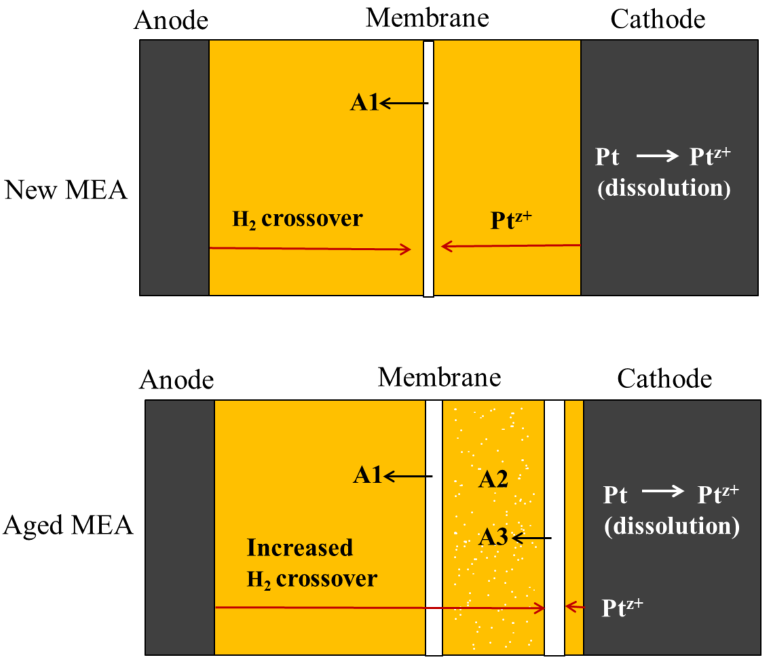

Figure 6.7: Schematic diagram of the Pt bands formation in the membrane [59].

6.4. Electrochemical measurements

6.4.1. Cyclic voltammetry

The cyclic voltammetry (CV) technique is used to investigate the impact of Pt corrosion on the electrochemically active surface area (ECSA) loss. Figure 6.8 presents the cathode CV curves of the new and aged MEAs. The aged MEA after the first 100 h test at 200 mA cm^{-2} and the second 100 h at OCV are named as aged MEA 100 h and aged MEA 200 h, respectively. Due to the remarkable reversible voltage loss during the OCV operation, the aged MEA was run by a recovery process before the electrochemical measurements. The peaks in the black box of Figure 6.8A are caused by the hydrogen desorption process, and it can be seen that the oxidation current in this region decreases, signifying reduced ECSA. One thing should be noted here is that in HT-PEFCs, Pt degradation is the main, but not the only cause for the changes in ECSA during the aging process. The ECSA is also significantly affected by the adsorption of phosphorus impurities on the Pt surface [132]. The adsorption mechanism is complicated due to a series of chemical transformations of PA and the influencing factors such as the operating temperature and PA concentration [133, 134]. Thus, the adsorption of phosphate anions results in lower ECSA values compared to those of LT-PEFCs [93]. Although the CV test for PBI-based HT-PEFCs is less rigorous than classic PEFCs, it is still an effective in-situ method for estimating the ECSA loss during durability tests.

The ECSA values of the new MEA and aged MEA are depicted in Figure 6.8B. There is a 7.6% ECSA loss by comparing the new MEA and the aged MEA 100 h, which is highly related to the formation of the first Pt band in the membrane. During the 100 h OCV operation, the ECSA remarkably decreases by 21.9%. This is ascribed to the high potential around 1.0 V on the cathode side, leading to severe Pt corrosion and further loss into the membrane. Besides, the formation of peroxide species and carbon corrosion also contribute to the pronounced ECSA loss [111].

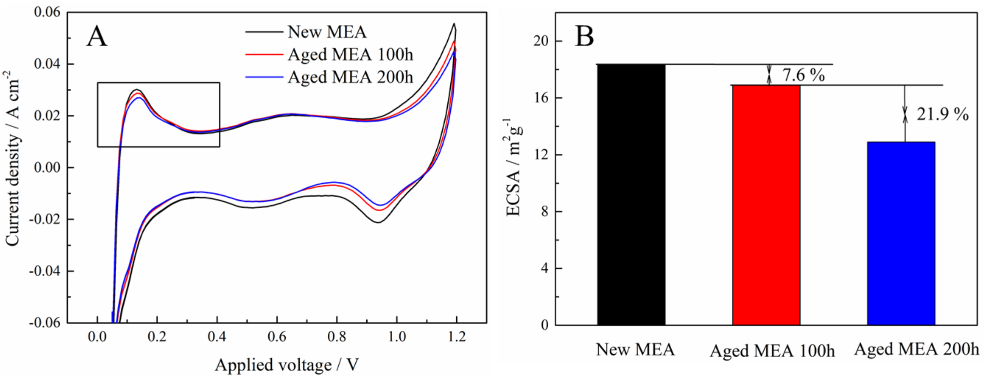

Figure 6.8: (A) Cathode CVs of the new and aged MEAs under N_2 atmosphere without humidification at 160 ℃; (B) calculated ECSA values of the new and aged MEAs [59].

6.4.2. Changes in cell resistance and performance

To investigate the effects of Pt dissolution and precipitation on cells' resistance and performance, EIS and polarization curves for the new and aged MEAs were recorded. Figure 6.9A presents the EIS plots performed at 100 mA cm^{-2} and the inset is the transmission-line equivalent circuit model. The Nernst diffusion element is not included in the model due to the negligible mass transport resistance at low loads. There is no increase in cell resistance by comparing the new MEA and aged MEA 100h, which agrees with the results in Figure 6.9B that the performance (black line and red line) is almost identical throughout the entire voltage range. It would seem that the impact of ECSA loss (supported by the FIB/SEM and CV tests) is not reflected on the MEAs' performance degradation under the constant load condition at 200 mA cm^{-2}. This result is probably explained by two factors. One is the excess Pt loading (1.10 ± 0.05 mg cm^{-2}) used in the CCL. The second is that the utilization of Pt particles in the CCL is much less than 100% and the ORR mainly occurs at the Pt catalyst particles close to the membrane [135]. For the aged MEA 200h, there is a substantial increase in the overall resistance and a decrease in cell performance. More details can be seen in the EIS fitting results in Table 6.2.

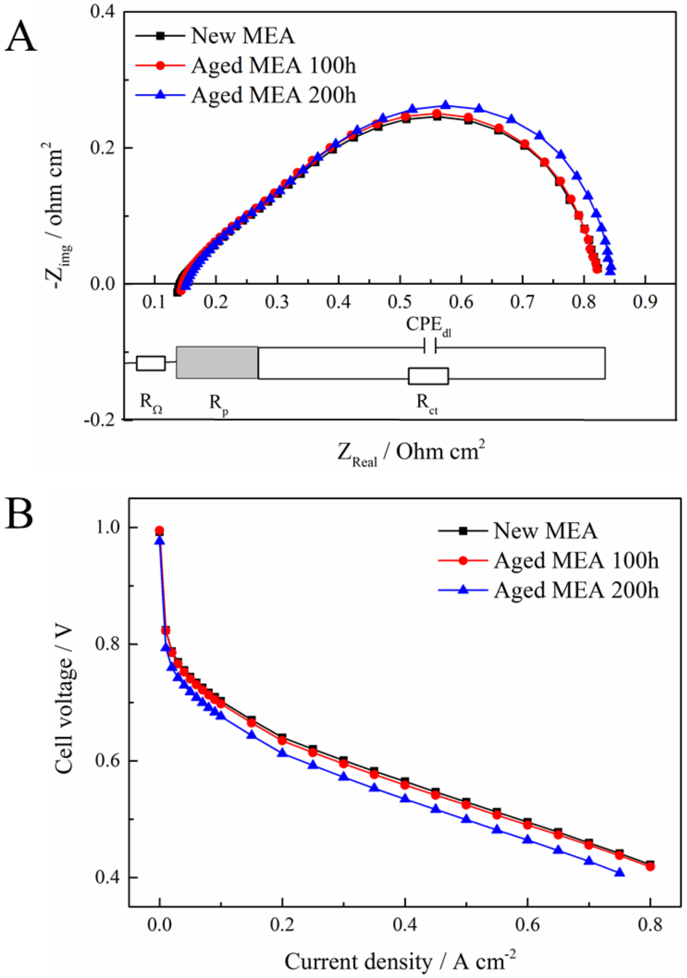

Figure 6.9: (A) EIS of the new and aged MEAs tested at 100 mA cm^{-2} conducted with the amplitude of 10 mV and the frequency range from 100 mHz to 100 kHz. T = 160 ℃ (inset is the equivalent circuit); (B) Polarization curves of the new and aged MEAs operated at 160 ℃, ambient pressure and $\lambda_{H2/air}$ = 2/2 [59].

We can see in Table 6.2 that the R_{Ω} is almost constant after the 200 h aging. This is due to that R_{Ω} is mainly dependent on the PADL, and PA leaching is negligible in a short period of operation, especially under OCV condition [136]. There is a slight increase in R_p, which may be caused by the carbon corrosion during OCV operation, resulting in the interface and structural changes in the CCL [43]. What is more, the R_{ct} highly increases after aging. This is caused by the formation of Pt bands in the membrane, leading to a considerable ECSA loss and thus an increased R_{ct}.

Table 6.2: Fitted EIS parameters of the new MEA and aged MEA 200h.

Measurement	R_Ω / Ω cm^2	R_p / Ω cm^2	R_{ct} / Ω cm^2	Fitting error / %
New MEA	0.128	0.181	0.518	±2.06
Aged MEA 200h	0.132	0.190	0.543	±2.15

6.5. Summary

The new MEA (run a break-in procedure) and the aged MEA (run a break-in procedure + 100h at 200 mA cm^{-2} + 100h at OCV) are characterized by the FIB/SEM technology.

- In the new MEA, a Pt band is formed in the PBI-based membrane, implying the severe corrosive environment in HT-PEFCs and enhanced degradation kinetics compared to classic PEFCs.
- A 7.6% loss in ECSA of the cathode is noted after the first 100h operation at 200 mA cm^{-2}, but the influence of catalyst degradation on the cell's performance is not obvious, indicating a limited Pt utilization efficiency in the CCL.
- The second Pt band is formed closer to the cathode/membrane interface, which is due to the membrane thinning effect and the increased hydrogen crossover.
- Compared to the constant operation at 200 mA cm^{-2}, the OCV condition is more detrimental for HT-PEFCs, leading to a significant decrease in ECSA and increase in R_{ct}.

7. Comparison of degradation under various operating conditions

This chapter focuses on comparing the degradation behavior under various conditions as well as investigating the influence of operating conditions on the degradation mechanism. After the break-in process, the degradation rate of HT-PTFCs is fast within hundreds of hours of the initial operation and then slows down as a fairly constant condition is approached [39, 65]. Therefore, a 100 h aging test was conducted to investigate the degradation behavior in HT-PEFCs.

Six identical HT-PEFCs were prepared with the Pt loadings of 0.6 ± 0.05 and 1.1 ± 0.05 mg cm^{-2} at the anode and cathode, respectively. The PADL was maintained at 15.0 ± 1.0 mg cm^{-2}. Five stressors, including high temperature, thermal cycling, open circuit voltage, high-load cycling and low-load cycling are applied to accelerate the degradation process and compared to the standard operating condition (details are shown in Table 7.1). Under each condition, the anode and cathode were purged with non-humidified pure hydrogen and air, respectively, with a stoichiometry of 2/2. Each cell was activated by a break-in procedure for 70 h running at 200 mA cm^{-2} prior to the 100 h aging test. Then, a polarization curve, electrochemical impedance spectroscopy (EIS) and cyclic voltammetry (CV) were recorded as beginning of life (BOL). During the 100 h aging test, condensed water was collected from the cathode side by cooling the exhaust gas down to 7 °C. The PA and Pt losses under different test conditions were compared by using inductively coupled plasma mass spectrometry (ICP-MS). After the 100 h aging test, a polarization curve, EIS and CV were recorded as end of life (EOL). After that, each aged MEA was cut into rectangular pieces (about 1 × 2 cm^2) for the FIB/SEM characterization. It should be noted that before the EOL test, Cell 3 aged the under OCV condition was recovered to a steady state to exclude the severe voltage drop caused by reversible processes [74]. The recovery process consists of two steps: 1) run Cell 3 at 200 mA cm^{-2} for 2 h to wet the membrane; 2) shut down the test rig and keep the cell without operation overnight to reach the equilibrium distribution of PA and reduce the Pt oxidation layer (cell voltage below 0.3 V).

Table 7.1: Operating conditions of the HT-PEFCs.

HT-PEFCs	Operating strategies
Cell 1	Standard condition (160 ℃, 200 mA cm^{-2})
Cell 2	High temperature (180 ℃, 200 mA cm^{-2})
Cell 3	OCV (160 ℃, open circuit voltage)
Cell 4	Thermal cycling (temperature cycled at 140 ℃, 160 ℃, and 180 ℃ at 1-h intervals, 200 mA cm^{-2})
Cell 5	High-load cycling (160 ℃, current density jumps between 200 and 600 mA cm^{-2} at an interval of 50 mA cm^{-2} every 5 min)
Cell 6	Low-load cycling (160 ℃, current density jumps between OCV and 200 mA cm^{-2} at an interval of 50 mA cm^{-2} every 5 min)

The work has been published in *Journal of Power Sources*, which is used with permission from the Copyright Clearance Center [137].

7.1. Voltage-time curve

The voltage-time curve and voltage degradation rate (VDR) of each cell during the 100 h test are shown in Figure 7.1. The VDR is calculated by Equation 7.1:

$$\mathrm{VDR} = (V_{\mathrm{BOL}} - V_{\mathrm{EOL}}) / 100\ \mathrm{h} \tag{7.1}$$

Figure 7.1A depicts the voltage-time curves of the break-in procedure and the cells tested under constant conditions. It can be seen that the cell voltage continuously decreases during the 70 h break-in process, which may be caused by the PA redistribution in the MEA: before the break-in, the PA migrates from the membrane to the catalyst layers due to a concentration difference. By this, an initial PA balance is established in the MEA before tests. During the break-in process, water is generated in the CCL, which leads to a PA redistribution from the ACL and membrane to the CCL, thus aggravating the PA flooding in the CCL.

Moreover, the voltage drop during the break-in process is probably related to the formation of Pt surface oxide or adsorption of contaminants [111]. The same explanation applies to the voltage drops of Cell 1 within the first 20 h and Cell 2 within the first 30 h of the 100 h aging tests. After approaching the steady state, the voltage of Cell 1 stays constant. This is due to the limited degradation under the standard condition, which has been discussed in Chapter 6. Also, the voltage of Cell 2 keeps constant after the downward trend. This observation is inconsistent with the works of Zhang et al. and Søndergaard et al., which demonstrate that the performance degradation at a higher temperature (180 ℃) is more significant than that at a lower temperature (160 ℃) [138, 139]. By comparing the experimental conditions between these works and our own, the cell voltage remains constant under the high-temperature operation may be due to the negligible PA leaching during the short-term operation and different anode gases. The voltage variation of Cell 3 during the OCV operation has been detailedly discussed previously in Section 4.1.

Figure 7.1B shows single cycles of the cells tested under dynamic conditions. The voltage of Cell 4 changes with time due to varied electrode reaction kinetics at different temperatures. Once again, the cell voltage drops rapidly during the first 25 h and then remains constant (Figure 7.1C). Figure 7.1D shows the voltage-time curves of the load cycling tests. Cell 5 is cycled at a low voltage range below 0.65 V and Cell 6 at a high voltage range between 0.6 V and 1.0 V. The inset exhibits the VDRs at different current densities. We can see that the VDRs tend to increase with the current density. At the overlapping point of 200 mA cm^{-2}, Cell 6 shows a higher degradation rate than Cell 5 (135 μV h^{-1} vs. 103 μV h^{-1}). Furthermore, the recorded OCV of Cell 6 increases with time up to about 40 h, which is longer than the time required for Cell 3' OCV to reach the maximum (around 7 h). This is because that compared to the currentless operating condition of Cell 3, water is generated in Cell 6, resulting in more time required to reach the thermodynamic equilibrium of the membrane hydration and dehydration processes.

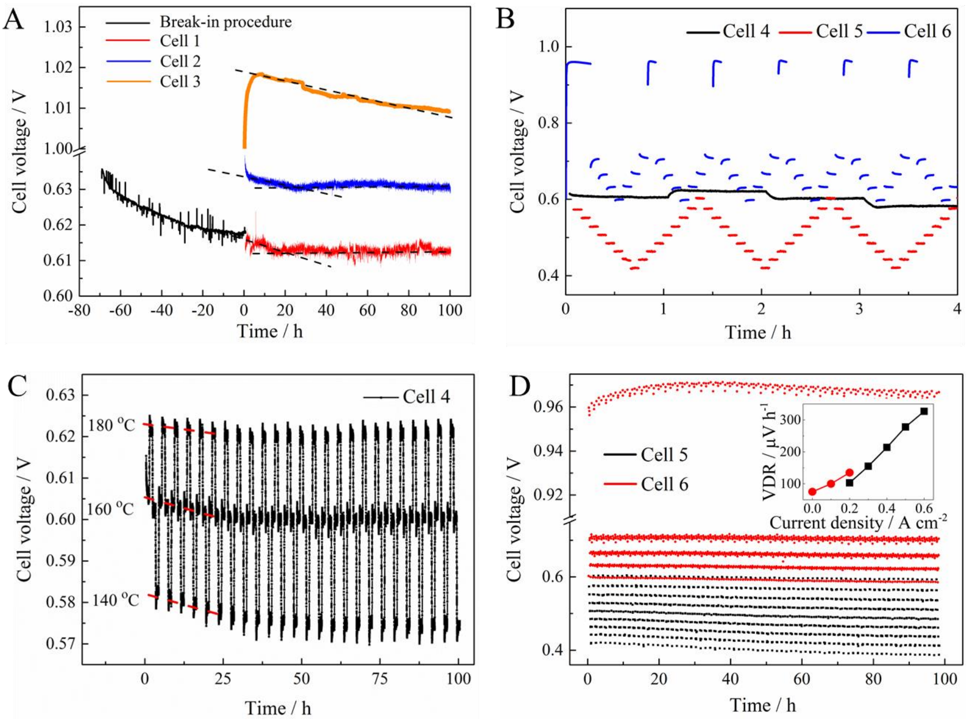

Figure 7.1: (A) Voltage-time curves of the break-in procedure and the cells under constant test conditions; (B) single cycles under dynamic test conditions; (C) the thermal cycling test; and (D) the load cycling tests (inset is VDRs of Cell 5 and Cell 6) [137].

7.2. FIB/SEM and EDX mapping analysis

7.2.1. FIB/SEM characterization

Figure 7.2 shows the SEM images of the FIB-prepared cross-section on the anode side for each cell. It can be seen that with the exception of Cell 3, there is no noticeable Pt agglomeration in the CCL and Pt precipitation in the membrane. In the magnified SEM image of Cell 3, dispersed Pt agglomerations are observed at the interface. This is probably caused by an enhanced oxygen crossover due to the extraordinary membrane thinning effect. Further, localized hydrogen starvation occurs, resulting in the “reverse current” phenomena and much higher potential in the local anode catalyst layer (ACL) [140]. Accordingly, Pt particles in the anode dissolve and migrate into the membrane. In the other cells, water is produced during the operations, leading to the limited membrane thinning effect; thereby, the anode potential approaches 0 V and no Pt corrosion occurs at the ACLs [124].

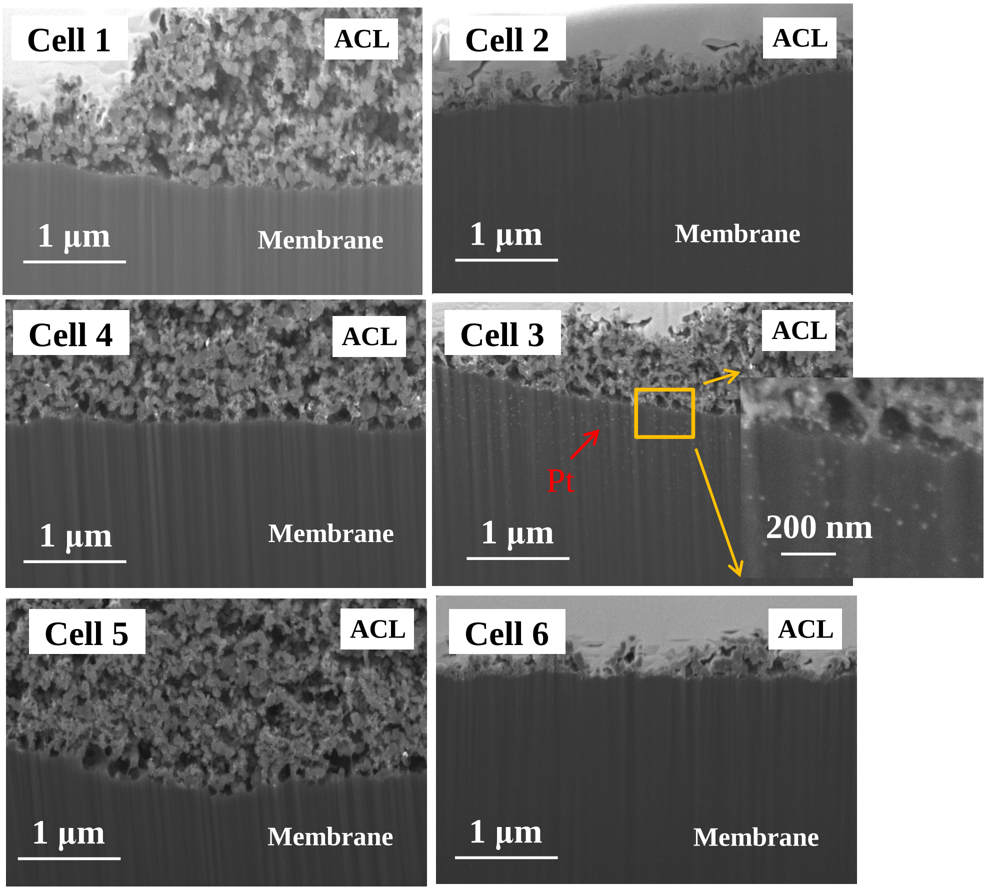

Figure 7.2: SEM images of the FIB-prepared cross-section on the anode side [137].

The SEM images of the FIB-prepared cross-section on the cathode side for each cell are presented in Figure 7.3. The Pt corrosion is indeed affected by the operating conditions and the six cells exhibit strongly different Pt precipitation behaviors in the membrane. In Cell 1 tested under the standard condition, a white band with low contrast is observed in the membrane. According to the results in Chapter 6, the white region in the membrane is ascribed to a band-like Pt precipitation (proved by the EDX mapping results below).

Compared to Cell 1, Cell 2 shows a strengthened Pt band, implying a more severe Pt degradation at an elevated temperature. What is more, the location of the Pt band(s) in Cell 2 is closer to the CCL than that in Cell 1. A thin and bright Pt band is observed in the membrane of Cell 3, which locates further closer to the catalyst layer.

Compared to other cells, Cell 4 operated under the thermal cycling condition shows a larger Pt precipitation region in the membrane, with low brightness and contrast. Both Cell 5 and Cell 6 are tested in the load cycling modes; however, they exhibit totally different Pt precipitation phenomena. Compared to Cell 5, Cell 6 presents only one clear Pt band, which is much brighter than the bands in Cell 5. More detailed information on the Pt corrosion is provided by the EDX mapping analysis below.

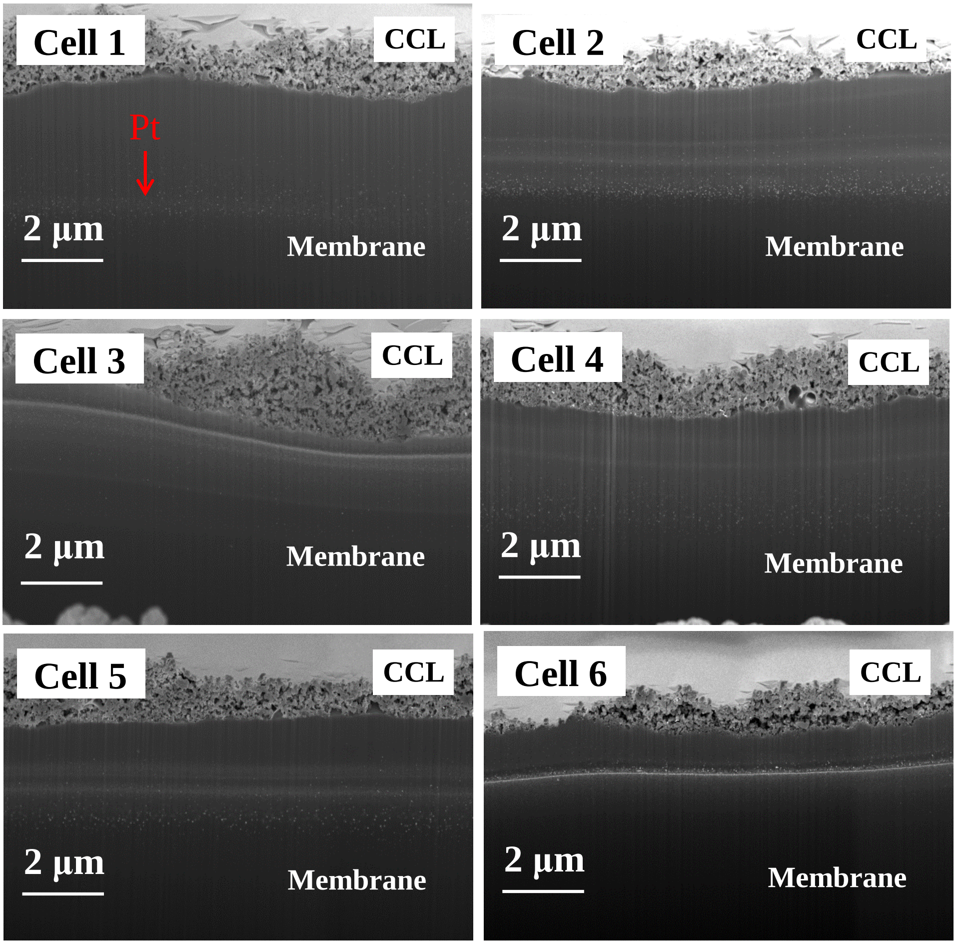

Figure 7.3: SEM images of the FIB-prepared cross-section on the cathode side [137].

7.2.2. EDX mapping analysis

To further investigate and compare the precipitation behavior, the EDX mapping and line-scan profile of Pt were recorded on the cathode side of each cell. Figure 7.4 shows the images of Cell 1. In the EDX mapping image, the interface of the membrane/CCL is marked with a purple dashed line. The image below is the corresponding EDX line-scan profile, which is determined by the average of the Pt atom% (At%) in the mapped area. The rise of Pt At% at the right side of the curve is caused by the Pt protective layer deposited on the area of investigation.

It can be seen that a small Pt peak appears at a distance of 2.3 μm from the interface in Cell 1, which corresponds to the Pt band in the membrane formed during the 70 h break-in + 100 h running at 200 mA cm^{-2}.

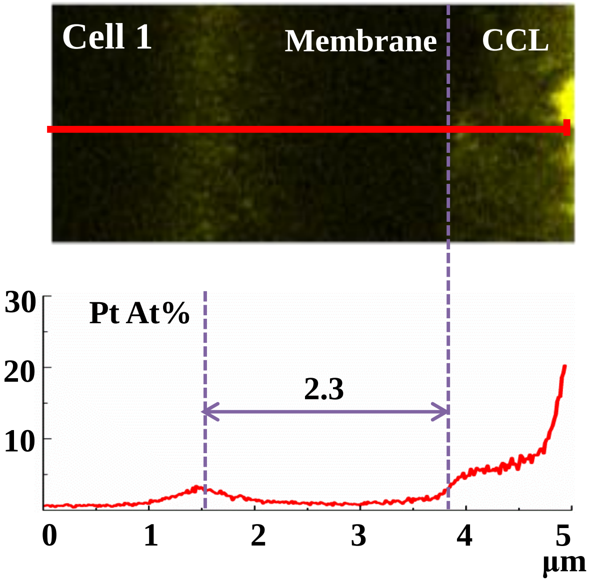

Figure 7.4: EDX mapping and line-scan profile of Pt in Cell 1.

In Cell 2, two distinct Pt peaks are observed with distances of 2.0 and 1.5 μm from the interface, respectively, as shown in Figure 7.5. Zhang et al. reported a model that describes the position of the Pt band in the membrane [56]. The authors claim that the Pt particles in the membrane will dissolve and migrate until the local flux ratio of O_2 and H_2 is 1/2. The distance between the Pt band and the interface is determined by the gas permeability of the membrane, gas partial pressure, and the thickness of the membrane that is positively related to the distance. In the EDX line profile, each peak in Cell 2 locates closer to the membrane/CCL interface than that in Cell 1.

Since Cell 1 and Cell 2 are operated with the same membrane material and gas flow rates, the smaller distances of the Pt bands in Cell 2 are probably ascribed to the membrane thinning effect at the elevated temperature [67]. During the membrane thinning process, a Pt band with the distance of 2.0 µm is formed and the peak formed during the break-in is merged into the strengthened Pt peak. According to the discussion in Figure 7.1, the steady state in Cell 2 is approached after approximately 30 h of the aging test. Thereafter, the second Pt band appears at a distance of 1.5 µm to the membrane/CCL interface.

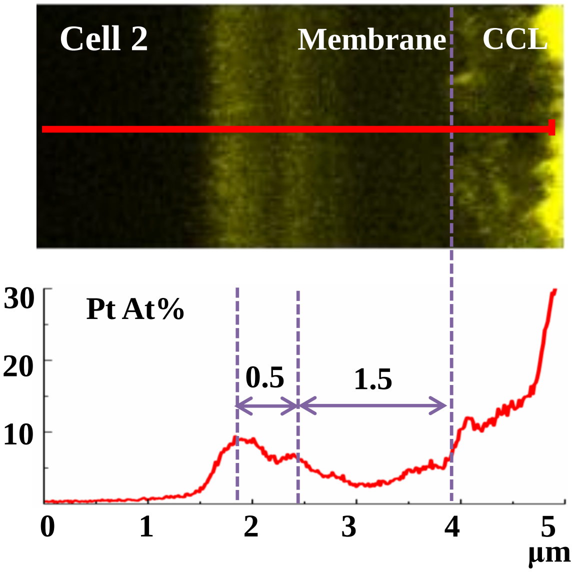

Figure 7.5: EDX mapping and line-scan profile of Pt in Cell 2.

Figure 7.6 presents the EDX mapping and line-scan profile of Pt in Cell 3. A small Pt peak is noted at a distance of 2.1 µm to the interface, which results from Pt corrosion during the break-in procedure. The distance is slightly different from that in Cell 1 (2.3 µm). This is considered to be caused by an experimental deviation, e.g., a difference in PADL in the membrane may lead to a different hydrogen dissolution and crossover. In addition, an intensive Pt peak is observed with the smallest distance (0.3 µm) to the interface. Similar to the explanation for Cell 2, the shift of the Pt band to the CCL is attributed to the considerable membrane thinning during the OCV hold test [141].

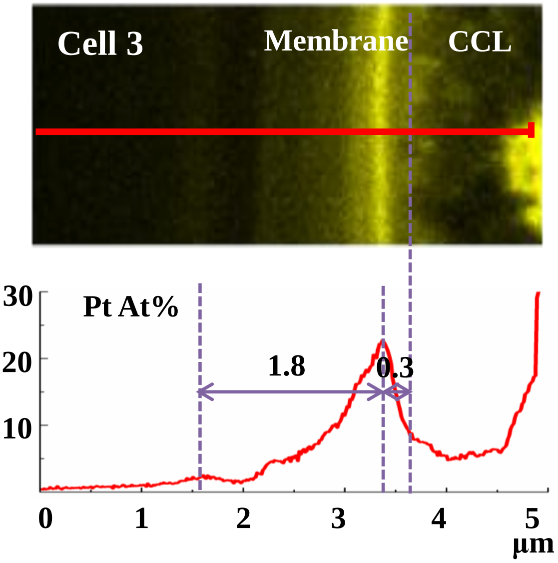

Figure 7.6: EDX mapping and line-scan profile of Pt in Cell 3.

Pt precipitation in the cells operated under dynamic conditions is more complicated. As shown in Figure 7.7, three Pt peaks are observed in the membrane of Cell 4, which correspond to Pt precipitation at three cycling temperatures. As discussed above, peaks closer to the interface are caused by higher temperatures. Therefore, the distances of the Pt peaks formed at 140 ℃, 160 ℃ and 180 ℃ are 2.2 µm, 1.0 µm, and 0.4 µm to the interface, respectively. It should be noted that the distances in Cell 4 are much smaller than those in Cell 1 and Cell 2 at the same temperatures. This may be due to an increase in hydrogen crossover during the thermal cycling test compared to the constant load operations. At 140 ℃, the dehydration process of the membrane is not obvious and starts at higher temperatures [67]. Therefore, the membrane thins at higher temperatures (160 ℃ and 180 ℃) and swells at 140 ℃. The expansion/contraction effects can impose mechanical stress on the membrane, resulting in membrane degradation and thus increased hydrogen crossover (supported by the substantially reduced OCV of Cell 4 shown below).

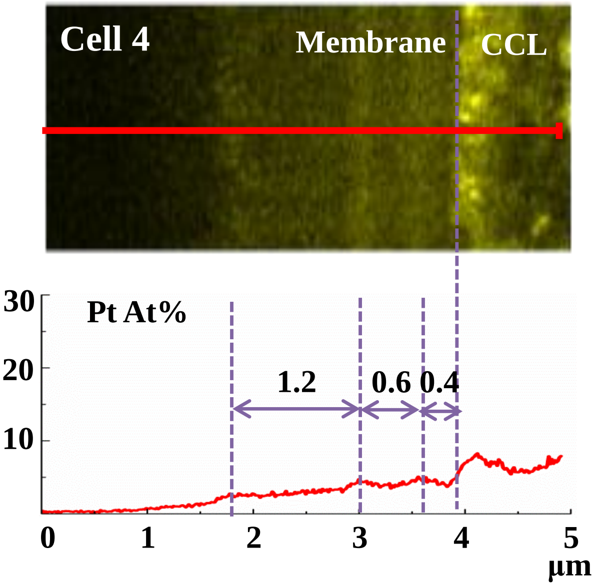

Figure 7.7: EDX mapping and line-scan profile of Pt in Cell 4.

In our previous work, the changes in membrane thickness under dynamic operating conditions were visualized by using in-situ synchrotron X-ray radiography. The results demonstrate that there is a considerable swelling (20%) of the PBI-based membrane by switching the load from OCV to 140 mA cm^{-2}, while further increases in current density do not cause any detectable changes [141]. According to these observations, the membrane thickness of Cell 5 remains constant during the aging process. The location of Pt bands is presumably impacted by changes in water vapor partial pressure and PA redistribution under different loads, resulting in the changes in gas permeability of the membrane [142]. Moreover, unlike the separated Pt peaks in Cell 4, the Pt peaks in Cell 5 are merged to some extent, which is probably ascribed to the unstable condition in the membrane due to the short-time current jump.

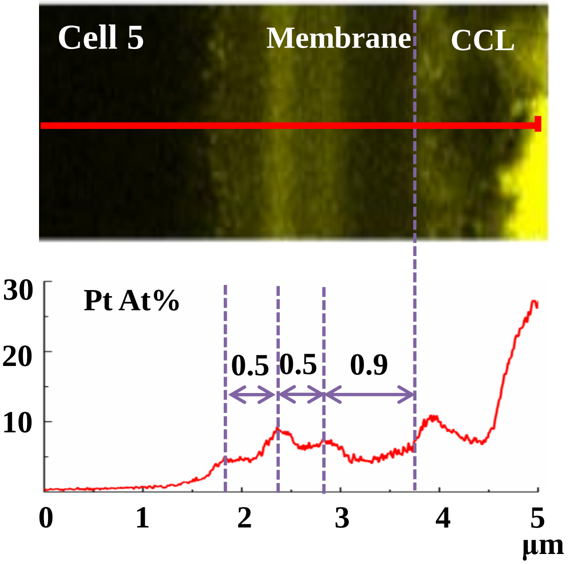

Figure 7.8: EDX mapping and line-scan profile of Pt in Cell 5.

In the EDX line profile of Cell 6 shown in Figure 7.9, only one sharp Pt peak is observed at a distance of 0.8 µm to the interface of CCL/membrane, indicating a relatively stable state of the membrane during the aging test. This can be explained by less water generation at low loads. Besides, as the hydration process of the membrane is much faster than the dehydration process [105], the membrane thickness could reach a dynamic equilibrium during the cycling operation, with only slight changes.

In addition, Pt particles agglomeration in the CCL of each cell is observed from both the mapping image and EDX-line profile. The repeated oxidation and reduction of the Pt particles lead to the Pt migration towards the membrane. Part of the Pt particles aggregate at the interface in the CCL, resulting in small Pt particles growth to agglomerations via the Ostwald ripening mechanism [143].

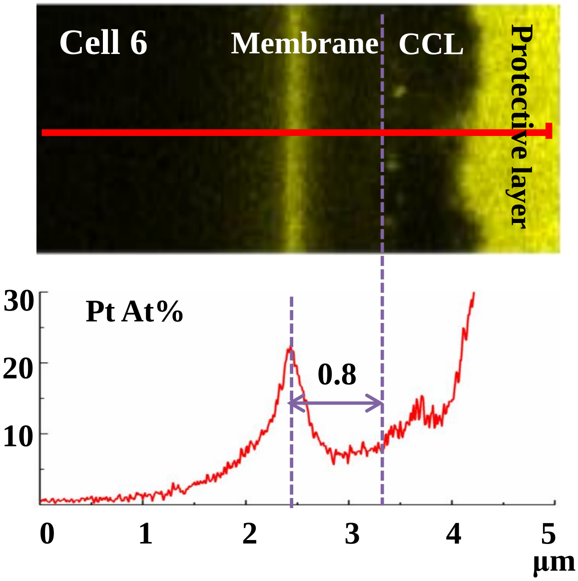

Figure 7.9: EDX mapping and line-scan profile of Pt in Cell 6.

The average Pt At% in the membrane of the mapped area is calculated by Equation (7.2):

$$\overline{Pt}\ At\% = \frac{\int_{0(\text{interface})}^{\Delta x} Pt\ At\%\ (x)\ dx}{\Delta x} \tag{7.2}$$

We can see in Table 2 that the average Pt At% in the membrane is in the following order: Cell 3 $\approx$ Cell 6 $>$ Cell 2 $\approx$ Cell 5 $>$ Cell 4 $>$ Cell 1. The value of average Pt At% in the membrane of Cell 1 is the smallest, suggesting limited Pt corrosion under the standard operating condition. In Cell 3 operated at OCV and Cell 6 cycled at high voltages, the value of average Pt At% is the highest, which is more than three times that in Cell 1. The results indicate that the high potential is the most important factor in degradation of the Pt catalyst.

Furthermore, Cell 2 aged at the high temperature and Cell 5 cycled at high loads show significantly higher Pt content in the membrane compared to Cell 1, illustrating that high-temperature and load cycling conditions are the next stressors that affect the durability of the Pt catalyst. Zhao et al. conducted potential cycling and potential hold experiments to investigate the Pt/C catalyst degradation in classic PEFCs. The results demonstrate that the dissolution and precipitation of Pt in the membrane mainly depends on the operation time rather than the operation conditions [144]. However, in current work, the HT-PEFCs tested under various operating conditions exhibit notably different Pt precipitation phenomena, possibly suggesting different catalyst degradation mechanisms between HT-PEFCs and classic PEFCs.

The ECSA loss of each cell is obtained from the difference between ECSA BOL and EOL, with the values presented in Table 7.2. The calculated ECSA loss is in the following order: $\mathrm{Cell}\ 6 > Cell\ 2 \approx Cell\ 3 > Cell\ 5 > Cell\ 4 > Cell\ 1$, which is approximately the same as the order of the average Pt At% precipitation in the membrane, with a few exceptions. This is because Pt degradation is the dominant but not the only factor in ECSA loss. In HT-PEFCs, ECSA is significantly impacted by the adsorption of contaminations on the surface of Pt [132], hence leading to relatively large deviations when comparing ECSA losses under different accelerating stressors.

Table 7.2: Values of the average Pt At% and ECSA loss for each cell.

HT-PEFCs	Cell 1	Cell 2	Cell 3	Cell 4	Cell 5	Cell 6
Average Pt At%	1.28	3.35	4.85	2.25	3.23	4.79
ECSA loss / m^2 g^{-1}	0.63	1.78	1.76	0.76	1.06	2.02

7.3. ICP-MS measurement

The phosphoric acid leaching, especially on the cathode side, is one of the most important reasons for limiting the durability of HT-PEFCs [72]. In order to compare the PA loss under each stressor, the liquid water was collected from the cathode side, with the exception of Cell 3, as no water was generated under the currentless condition. The concentrations of Pt and PA in the water were determined by ICP-MS, with the loss rates calculated by dividing the operating time. We can see in Figure 7.10 that the most severe condition for PA leaching is the thermal cycling condition in Cell 4, with a PA loss rate of 94.2 ng h^{-1} cm^{-2}. Cell 2 operated at the elevated temperature exhibits the second highest PA loss rate. This is considered to be related to the enhanced PA vapor saturation at higher temperatures [139, 145]. These results illustrate that the high temperature is the most significant factor that causes the PA loss in HT-PEFCs. In addition, Cell 5 cycled at high loads shows a higher PA loss rate than that in Cell 1 and Cell 6, which demonstrates that the high load adversely impact the stability of PA in the MEA. One possible explanation relates to the high water production under high loads, resulting in the redistribution of PA from the membrane to the CCL and GDL. Moreover, the increased gas flow rate helps move isolated PA droplets outside the HT-PEFCs [146].

For all the cells, the maximum amount of PA loss over the entire 100 h aging is 9.42 μg cm^{-2} (Cell 4), which accounts for less than one-thousandth of the PADL (15.5 ± 1.0 mg cm^{-2}) in the MEA. Furthermore, according to a previous work from our group, the PA loss rate trends to decrease over time [136]. These results indicate that the PA loss during the aging tests is negligible.

Also, Pt loss during the aging is detected for each cell by the ICP-MS technology. Relatively high standard deviations exist in the Pt detection due to the small Pt concentration in the collected water. Again, Cell 4 under the thermal cycling condition exhibits the highest Pt loss (11 μg m^{-2} during 100 h of operation), which accounts for one-millionth (1.10 ± 0.05 mg cm^{-2}) of the Pt loading in the CCL. The results explicitly demonstrate that Pt moving outside the HT-PEFCs is not the cause for the ECSA loss and performance degradation.

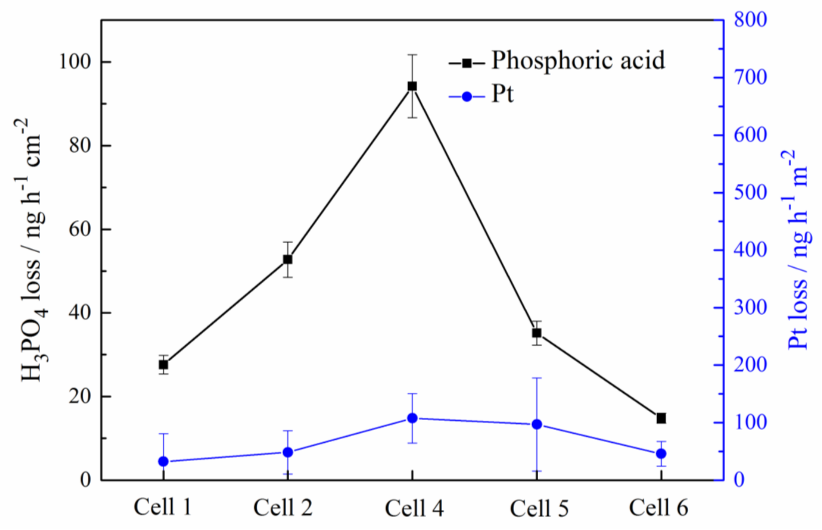

Figure 7.10: PA and Pt loss rates from the cathode side.

7.4. Electrochemical impedance spectroscopy

The EIS measurements were carried out at a current density of 200 mA cm^{-2}, T=160 ℃. The EIS data were fitted by the equivalent circuit model presented in Section 1.3.

Figure 7.11 shows the BOL and EOL ohmic resistances (R_Ω) of the cells. It is clear that there is no obvious difference after the aging test for each cell by comparing the BOL and EOL values. This is because R_Ω is mainly dependent on the PA content in the membrane and often referred to as the membrane resistance [95, 96]. According to the ICP-MS measurements discussed above, the PA leaching is negligible for each stressor, thus leading to a relatively constant R_Ω during the aging test. In addition, except for Cell 3, R_Ω slightly decreases in the cells. This is probably ascribed to the PA redistribution from the membrane to the catalyst layers during the operations, and the removal of excess PA results in a thinner membrane and ultimately a decreased R_Ω [147]. The small increase in R_Ω of Cell 3 is closely related to the membrane degradation due to the formation of harmful radicals during the OCV hold test [148].

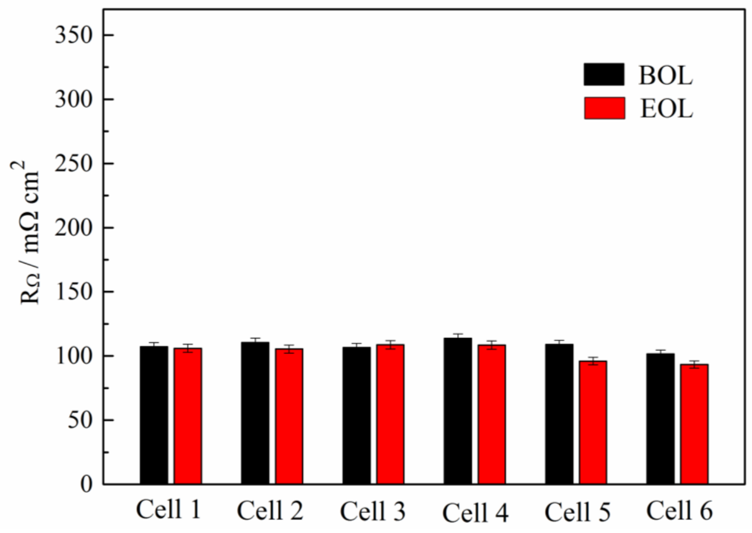

Figure 7.11: BOL and EOL ohmic resistances of each cell determined from the Nyquist plot recorded at 200 mA cm^{-2}, T=160 ℃, fitted by the equivalent circuit model that is presented in Section 1.3.

The BOL and EOL cathode protonic resistances of each cell are presented in Figure 7.12. As discussed in Section 5.4.2, the PADL in the MEA is the most dominant factor in affecting R_p. Similar to the R_Ω, the negligible PA leaching explains the comparable values of the BOL and EOL R_p, which signify that the protonic conductivity at the cathode is not a problem under various operating conditions.

The small difference in R_p before and after aging is caused by the changes in PA concentration and distribution. We can see that Cell 2 shows the greatest increase in R_p. It has been reported that the highest protonic conductivity of PA is in the concentration range of 62-65 wt. (P_2O_5)% at 160 ℃. Thereby, the protonic conductivity decreases as the PA concentration increases/decreases beyond the range [149, 150]. Liu et al. reported that the PA concentration is as high as 70 wt. (P_2O_5)% in the HT-PEFCs run at a current density of 200 mA cm^{-2} at 160 ℃ [150]. Under the higher-temperature operation (180 ℃), the PA concentration can further increase, thus leading to a relatively significant increase in R_p of Cell 2. In addition, there are small increases in R_p of Cell

4 and Cell 5, which can be attributed to the fact that the redistribution of PA leads to isolated PA droplets in the CCL or GDL, thereby reducing both the PA/catalyst interface and the PA content in the catalytic region.

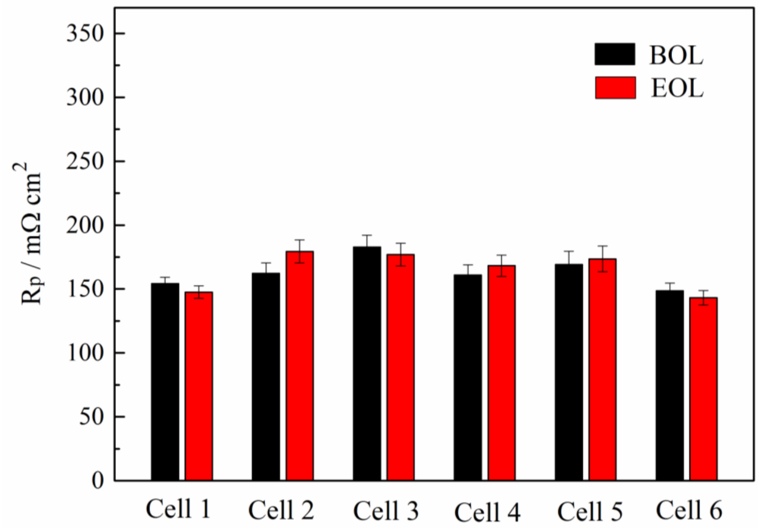

Figure 7.12: BOL and EOL cathode protonic resistances of each cell.

Figure 7.13 shows the BOL and EOL R_m of the cells. As all the cells are prepared by the same materials and method, varying degrees of R_m variation are considered to be independent of the electrode structure, which are determined by the migration and redistribution of PA. We can see from the figure that Cell 3 exhibits the most pronounced increase in R_m. During the OCV hold test, the high potential around 1.0 V at the cathode accelerates carbon corrosion/oxidation, causing the carbon surface to become more hydrophilic, and the CCL with enhanced hydrophilicity is easily impacted by the PA flooding, thus resulting in a remarkable increase in R_m [151]. What is more, there are moderate increases in R_m of Cell 1 and Cell 2 operated under the constant load conditions, which can be explained by the redistribution of PA from the membrane to the CCLs, as described previously, exacerbating the PA flooding effect. The other three cells (4, 5 and 6) aged under the dynamic conditions present the same trend of decreasing R_m. Eberhardt et al. investigated PA redistribution in HT-PEFCs using an in-Operando imaging technique. The results reveal that under dynamic conditions, PA migrates from the membrane and the region close to the membrane to the GDL and the flow field [152]. The PA migration weakens the impact of PA flooding on the gas transport in the CCL, hence leading to the reduced R_m.

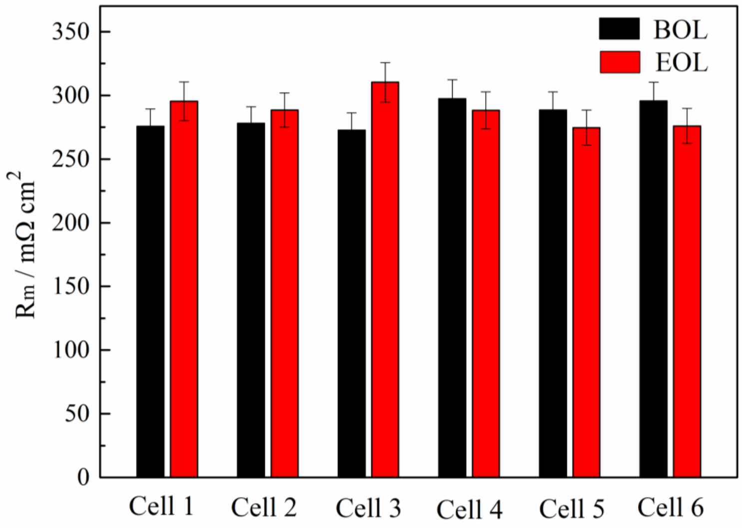

Figure 7.13: BOL and EOL mass transport resistances of each cell.

The charge transfer resistance at the interface between the catalyst and the electrolyte solution (Pt/PA) is inversely proportional to the exchange current density (j_0) for the ORR, which is, in turn, proportional to the number of reaction site, termed the three-phase boundary (TPB) where the Pt particles, PA and oxygen intersect [120, 153]. One previous work from our group reports that a higher PADL results in higher R_m and lower R_{ct} in HT-PEFCs [154], which can be applied to explain the decreases in R_{ct} of Cell 1 and Cell 2 (Figure 7.14). During the constant load tests, the PA electrolyte tends to move from the membranes to CCLs, leading to improvements in the area of the TPB and ultimately decreases in R_{ct}. The increase in R_{ct} of Cell 3 is closely related to the considerable Pt loss into the membrane and Pt agglomeration in the CCL. Under the dynamic conditions, the cells exhibit the same trend of increasing R_{ct}. This is caused by the notable Pt corrosion as well as the formation of isolated PA droplets, which reduce the contact area between the catalytically active Pt nanoparticles and PA electrolyte.

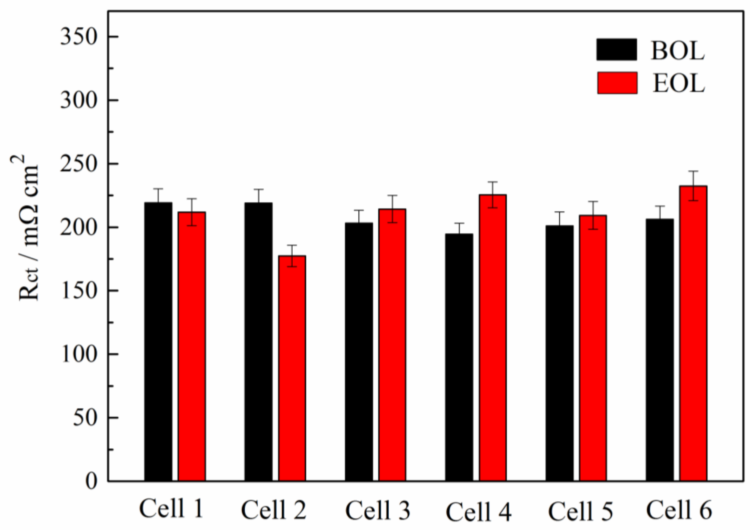

Figure 7.14: BOL and EOL charge transfer resistances of each cell.

Figure 7.15 shows the BOL and EOL cathode double layer capacitances of each cell. In HT-PEFCs, the C_{dl} is determined by the wetting area of the Pt/C catalyst by PA at the cathode [121]. By comparing Figure 7.14 and 7.15, it is noted that in each cell, with the exception of Cell 3, the change in C_{dl} is opposite to that in R_{ct} (i.e., when R_{ct} rises in a cell, C_{dl} decreases, and vice versa). This is because a decrease in R_{ct} means an enhanced exchange current density of ORR, and the larger contact area between the Pt surface and the PA electrolyte leads to an increase in C_{dl}. In Cell 3 aged by the OCV condition, the increase in R_{ct} is discussed above; the increase in C_{dl} shown in Figure 7.15 is presumably explained by the electrochemical oxidation of carbon black catalyst supports at the high potential, resulting in a smaller wetting angle for the carbon surface, and therefore a larger carbon/PA interface [155].

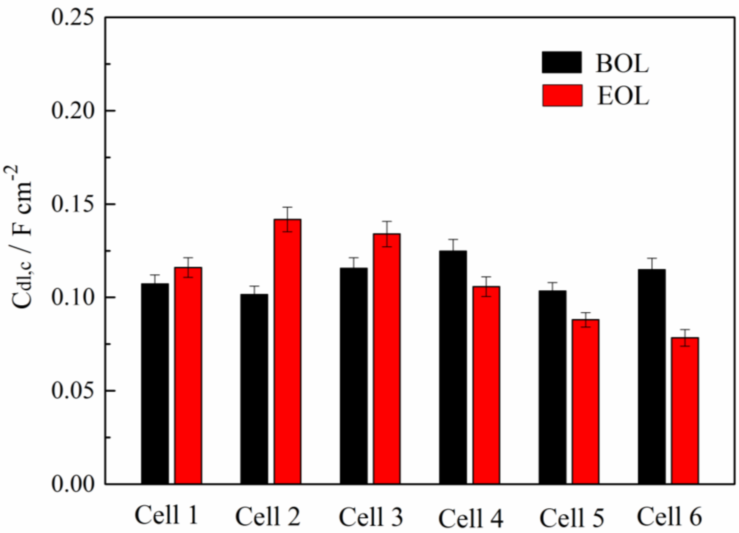

Figure 7.15: BOL and EOL cathode double layer capacitances of each cell.

7.5. Comparison of performance degradation

Figure 7.16 presents the BOL and EOL polarization curves of each cell. It is clear that the BOL and EOL curves of cells 1, 2 and 4 are almost the same and there are obviously different in the curves of cells 3, 5 and 6.

The OCV values were recorded by maintaining at an open-circuit condition for 30 min after the temperature was stable at 160 ℃. It can be seen that Cell 3 and Cell 4 exhibit notable OCV losses (over 15 mV). The relatively large OCV reduction of Cell 3 is ascribed to the accelerated formation rate of radicals under the open-circuit condition, promoting the membrane degradation [156, 157]. During the thermal cycling test, the phosphoric acid hydration and dehydration processes impose mechanical stresses on the membrane, leading to an increase in the hydrogen crossover and hence a lower OCV [128]. Cell 1, 2, 5 and 6 do not show obvious decreases in OCV, which indicates low membrane degradation.

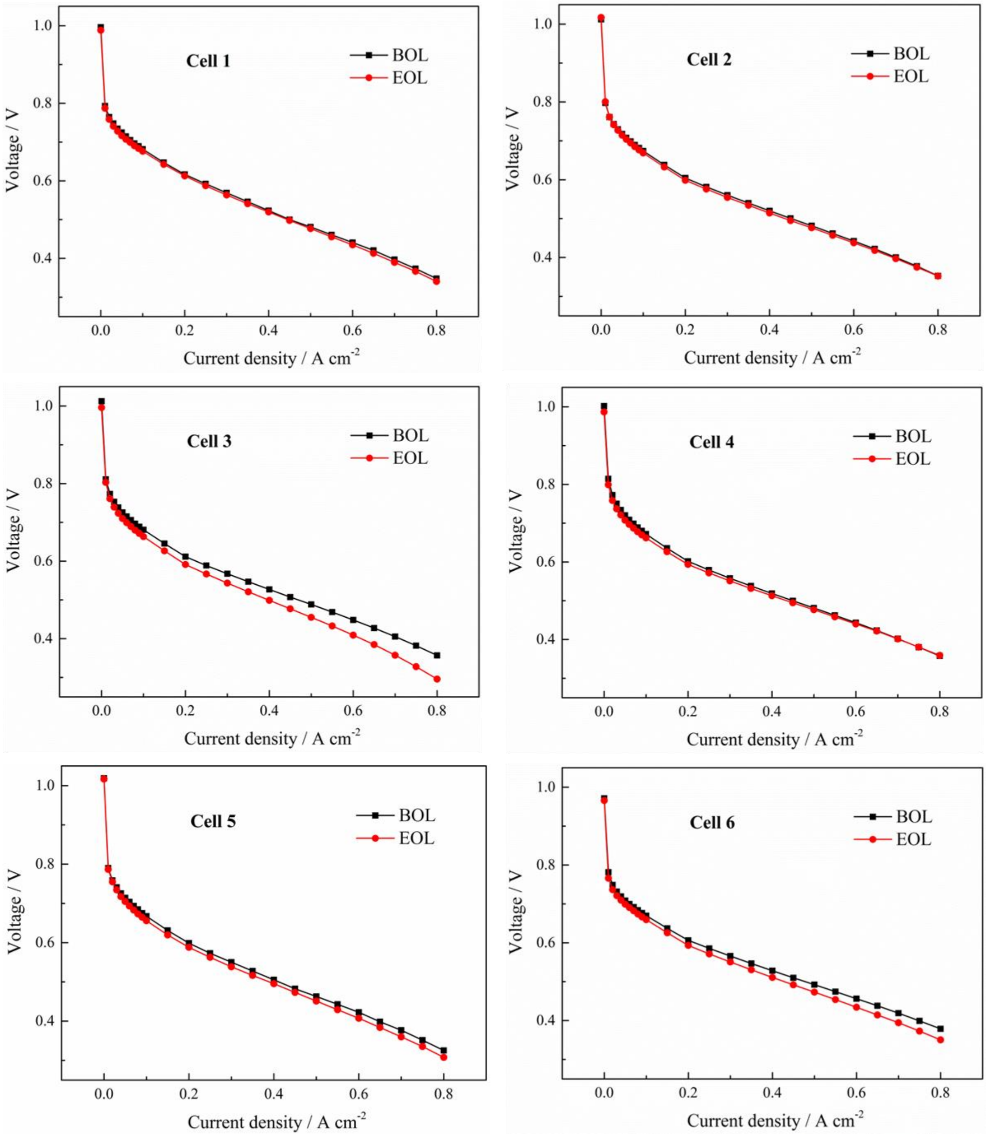

Figure 7.16: BOL and EOL polarization curves of each cell [137].

The performance degradation of each cell was obtained by subtracting the EOL polarization curve from the BOL polarization curve, as shown in Figure 7.17. In the kinetic region, the differences between the six curves are small with the voltage losses at less than 20 mV. This is due to the excess cathode Pt loading (1.10 ± 0.05 mA cm^{-2}) used in the CCL and the short-term operation. In addition, the voltage in this region can be affected by the H_2 crossover. Therefore, the enhanced H_2 crossover in Cell 4 causes a relatively high voltage loss.

At higher current densities, Cell 3 exhibits an approximately exponential degradation, which indicates that a severe gas transport problem occurs during the OCV hold test [65]. This result is consistent with the substantially increased R_m in the EIS results. Cell 6 and Cell 5 exhibit moderate voltage loses, which are approximately linearly related to the current density. The performance degradation of cells 1, 2 and 4 are not obvious due to the relatively low Pt corrosion and negligible PA leaching.

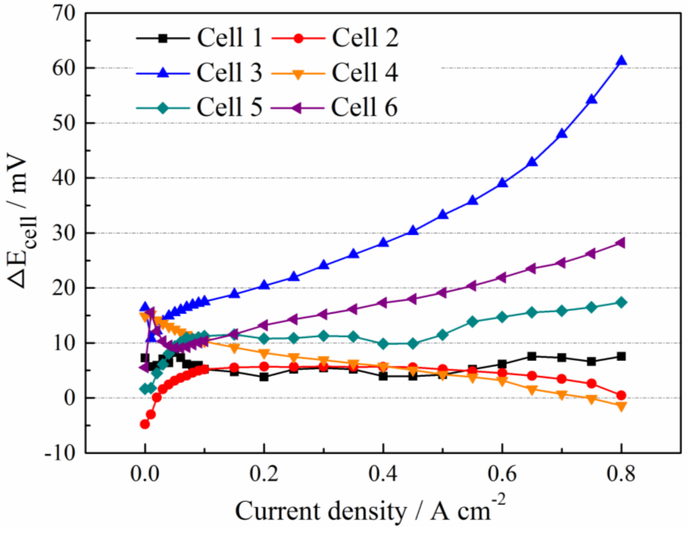

Figure 7.17: Performance degradation of each cell obtained by the difference between BOL and EOL polarization curves [137].

7.6. Summary

A 100 h initial durability test is applied to home-made HT-PEFCs under various operating conditions, including standard condition, high temperature, thermal cycling, OCV, and load cycling, to compare the degradation behaviors and study the degradation mechanism.

During the initial lifetime test, PA leaching is less than one-thousandth of the PADL in the membrane, which is considered to have no effect on the performance degradation of the HT-PEFCs. The thermal cycling is the harshest condition for the PA leaching. Also, high-temperature and high-load conditions can also contribute to the process.

Pt particles do not migrate from the CCL to the outside of HT-PEFCs. The catalyst degradation is attributed to the Pt particles agglomeration in the CCL and Pt precipitation in the membrane. The Pt precipitation phenomenon is explicitly influenced by the operating conditions. Cell 3 operated at OCV and Cell 6 cycled in the high potential range exhibit a larger amount of Pt precipitation than the other cells, suggesting that the cathode potential is the major reason for the Pt dissolution and migration. Furthermore, Cell 3 and Cell 6 demonstrate the most significant performance degradation. By this, the Pt precipitation behavior in the membrane can be used as an important indicator for the catalyst and performance degradation. In addition, high-temperature and load cycling operations are next stressors that accelerate the Pt corrosion.

The resistance and performance differences of the HT-PEFCs during the aging tests are mainly caused by the catalyst degradation and PA redistribution in the CCL. The OCV hold test is found to be the most destructive stressor among the operating conditions due to the considerable increase in R_{ct}, R_m, as well as the membrane degradation (supported by the reduced OCV). The load cycling at the low loads and high loads are indeed effective stressors, which lead to pronounced degradation at higher current densities. In addition to the OCV reduction during the thermal cycling test, the effect of temperature on the performance degradation is not obvious, which is attributed to the PA redistribution and the negligible amount of PA leaching.

8. Overall discussion

The contents of the dissertation can be roughly divided into two parts. One is related to the morphologies and parameters of the home-made MEAs, especially for those in the CCLs. The other part focuses on the degradation investigation on HT-PEFCs.

The binder PTFE plays an important role in the morphology, performance and durability of the CCL. Lee et al. investigated the effect of PTFE content on the electrochemical performance of electrodes. The results demonstrate that the electrode with 20 wt.% PTFE exhibits the best performance [104]. In the MEA prepared by a pressing process, the electrode with 45 wt.% PTFE shows the best performance. This is because the gas transport becomes more easily impacted by the PA flooding in the catalyst layer after the pressing process and a higher PTFE content can help to increase the hydrophobicity, thus alleviating the PA flooding effect [104]. In our cells, the 10 wt.% PTFE electrode presents the best electrochemical performance as discussed in Chapter 3. These results imply that the optimum PTFE content depends on the properties of electrodes that are determined by materials, preparing methods, etc. In the CCL, an excessive PTFE content can negatively impact the cell performance by blocking the porous structure, leading to an enhanced R_m. In Figure 3.13, the R_m notably increases when the PTFE content is over 25 wt.%. Moreover, too much PTFE particles in the CCL can cause a highly hydrophobic Pt/C catalyst surface, and the R_p significantly increases when the PTFE content is larger than 25 wt.%. On the other side, insufficient PTFE content in the CCL has a negative impact on HT-PEFCs’ performance. Firstly, less PTFE in the CCL could lead to a PA flooding effect that increases the R_m. In addition, during the durability test, the Pt corrosion and PA leaching are more severe in the CCL with less PTFE. Based on these discussions, it is advised that under low-load operations, a relatively low PTFE content is used in the CCL due to the low PA leaching and the high possibility of mass transport problem. At high loads, PA leaching becomes a non-negligible issue that influences the long-time durability of HT-PEFCs. In this case, relatively more PTFE is suggested in the CCL, as PA can be held in the PTFE network structure, thus resulting in a reduced PA loss rate.

Similar to the PTFE binder, the content of PA is crucial to HT-PEFCs' performance. The PADL has strong interactions with other parameters, e.g., thickness of the catalyst layer, properties of the catalyst, membrane, and so on. As discussed in Chapter 4, a high PADL in the MEA is explicitly beneficial for the proton transport in the membrane and the catalyst layer. What is more, an increased PADL means a larger area of Pt/PA interface, thereby enhancing the exchange current density for the ORR. However, an excessive PADL could lead to a mass transport problem, and this is the key issue that exists in HT-PEFCs. From my point of view, two methods may be helpful to reduce the PA flooding in the CCL: a) applying the catalyst with a low Pt/C ratio to prepare the catalyst layer. By this, Pt and PA can be better distributed, thus leading to a decreased R_m [117]. One thing should be noted is that a low ratio of Pt/C catalyst means a thicker CCL at the same Pt loading, which, in turn, increases the R_m. Therefore, the interaction between the Pt loading and the thickness should be carefully considered during the preparation process. b) Applying treated carbon supports in CCLs to alleviate the PA flooding, thereby facilitating the gas transport. In addition, PA redistribution during the operations can affect HT-PEFCs' performance. As discussed in Figure 7.1, the PA electrolyte in the membrane tends to migrate towards the CCLs during the break-in process and at the beginning of the constant load operations. Accordingly, the break-in procedure should be extended to around 100 h to reach the balanced distribution of PA. Under the operating temperature of 160 ℃, phosphoric acid (H_3PO_4) and pyrophoric acid ($H_4P_2O_7$) are the main forms that exist in MEAs. The operating temperature and water vapor partial pressure are the two main factors that affect the transformation between these two species. The maximum water vapor partial pressure is 1 bar in running cells, which is in the highest proton conductivity range [158]; therefore, the proton conductivity will consistently increase as the water content in HT-PEFCs increases. The highest conductivity of PA at 160 ℃ is in the concentration range of 62-65 wt.% P_2O_5 or 85-90 vol.% H_3PO_4 [150]. It is reported that the amount of H_3PO_4 at 160 ℃ and high current density ($j = 600$ mA cm^{-2}) is estimated to be 92.5 vol.% and at low current density ($j = 140$ mA cm^{-2}) 95.8 vol.% [159]. This means that the vol.% PA decreases as the current density increases, further leading to an increase in conductivity and a decrease in R_p. However, this statement is inconsistent with the observations of the load cycling test, as shown in Figure 7.12, in which Cell 5 exhibits a slight increase in R_p after the high-load cycling operation. This can be presumably explained by the violent migration of PA in the MEA, leading to the formation of isolated PA droplets, and thus decreased proton conductivity [152].

The degradation in HT-PEFCs has been comprehensively discussed. Among the operating conditions investigated in Chapter 7, the OCV condition is the most destructive stressor that accelerates the degradation in the MEA. Figure 8.1A exhibits the voltage-time curve and changes in the water activity during the 100 h OCV hold test. The OCV can be calculated by the Nernst equation as shown below:

$$E = E_{rev} - \frac{RT}{nF} \cdot ln\left(\frac{X_{H2O}}{X_{H2}X_{O_2}^{0.5}}\right) \tag{8.1}$$

where E is the recorded cell's voltage, E_{rev} is the reversible potential, equating to 1.14 V under our testing conditions [35], R is the universal gas constant, T is the operating temperature, and X_{H2O}, X_{H2} and X_{O2} are the molar fractions of water, hydrogen and oxygen, respectively.

The H_2 and O_2 molar fractions are obtained by Henry's law (Equation 8.2) on the assumption that the Pt/C catalyst is covered by a thin film of the PA electrolyte.

$$X^{liq} = k \cdot X^{gas} \tag{8.2}$$

However, it is not possible to determine the water concentration in the MEA due to the complicated chemical transformations of the PA species. Thereby, water activity is introduced as a theoretical parameter to model the water content. The Nernst equation is modified as below:

$$E = E_{rev} - \frac{RT}{nF} \cdot (ln\, \alpha_{H2O} - ln(k \cdot X_{H2}) - \ln(k \cdot X_{O2}^{0.5})) \tag{8.3}$$

As a reference value, the α_{H2O} is set to 1.0 at the start of the OCV aging test. The changes in α_{H2O} are calculated based on the assumption that Henry's constants for H_2 and O_2 are the same in the water/PA species system. In this case, K = 2.2 $\times 10^{-2}$ is obtained, with 1.14 V used as the reversible potential. We can see in Figure 8.1A that there is a sharp decrease in the α_{H2O} at the beginning of the OCV operation due to the drying of the MEA under the currentless condition, which leads to a drastic increase in E_{OCV}. Then, the OCV value fluctuates until around 7 h, which is probably explained by the changes in H_2 solubility in the PA species, resulting in changes in H_2 crossover. After the balance of the transformations in PA species is approached, the E_{OCV} starts to decrease. This is closely related to the increased hydrogen crossover caused by the membrane degradation (supported by the LSV results in Chapter 7). The cross-leaking hydrogen reacts with oxygen on the cathode side, leading to a smaller oxygen vapor partial pressure and a greater water activity, and therefore a decreased cell voltage. Actually, the OCV aging process can be roughly divided into two parts. From about 7 h to 58 h, the OCV aging rate is higher than that from 58 h to 100 h (174 $\mu V\ h^{-1}$ vs 75 $\mu V\ h^{-1}$). This can be probably explained by that during the OCV operation, considerable Pt particles migrate into the membrane, leading to the formation of Pt bands, as shown in Figure 7.6; the cross-leaking hydrogen and oxygen react at the Pt band, therefore, reducing the amount of hydrogen crossover in the CCL. A similar statement is reported in the work [58] that the Pt band in the membrane may be beneficial for HT-PEFCs' performance.

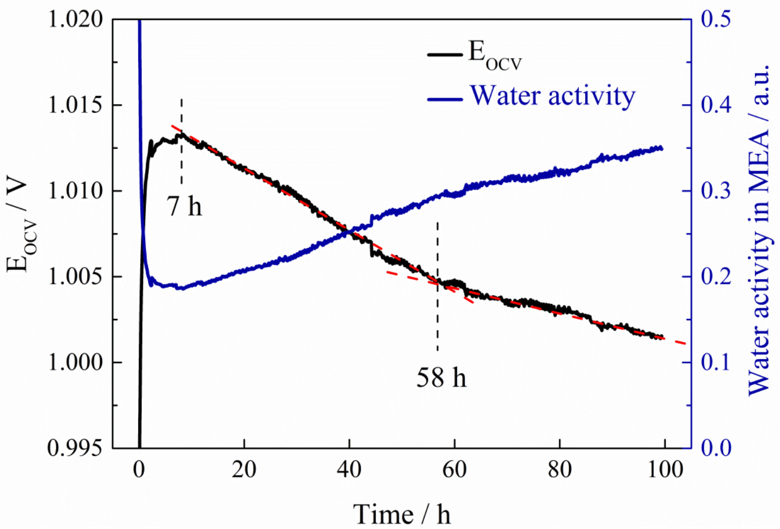

Figure 8.1: Voltage-time curve and water activity in the cell during the 100-hour OCV operation;.

The Pt precipitation as an irreversible degradation process is one of the main research objects in the dissertation. As discussed previously, the Pt band formation is impacted by operating conditions, and the high potential is the most harmful factor. Thereby, low-load operations should be avoided when running HT-PEFCs. In our results, the cell operated at a constant load of 200 mA cm^{-2} shows the least amount of Pt precipitation, with the cell voltage of 0.61 V. Further experiments should be done to visualize the Pt precipitation behavior in cells operated constantly at higher current densities, e.g., 300 mA cm^{-2} and 400 mA cm^{-2}. It is reasonable to suppose that no Pt band is formed under higher constant load conditions, as the Pt corrosion is mainly dependent on the cathode potential.

What is more, the Pt precipitation phenomenon seems to be affected by the catalyst types used in the CCL. Figure 8.2 shows cross-sectional SEM images and the corresponding EDX Pt maps of three MEAs. The only difference in the MEAs is the catalysts used in the CCLs. The Pt loading at the cathodes is the same (1.0 mA cm^{-2}) by using 20 wt.% Pt/C, 40 wt.% Pt/C and 60 wt.% Pt/C catalysts in the MEA 1 and MEA 2 and MEA 3, respectively. After the break-in procedure at 200 mA cm^{-2} for 70 h, the Pt band is only clearly visible in the MEA with 20 wt.% Pt/C used in the CCL. This may be explained by the highest voltage of MEA 1 during the break-in process, as shown in Figure 8.3, enhancing the degradation of Pt catalyst. The lower voltages of MEA 2 and MEA 3 are highly related to the thinner CCLs, resulting in more severe PA flooding. Besides, it is reported that the sizes of Pt particles in the catalysts are different, which may also contribute to the different Pt precipitation behaviors [160].

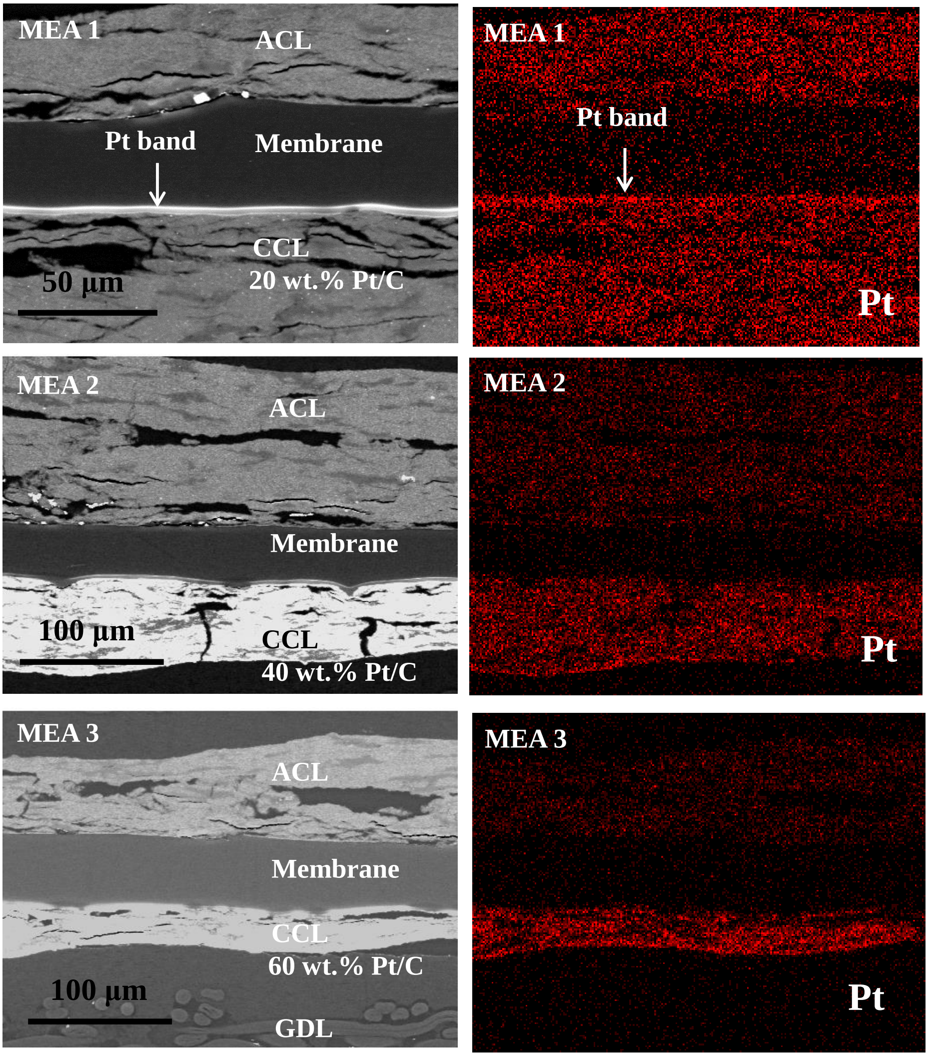

Figure 8.2: Cross-sectional SEM images and the corresponding EDX Pt maps of the MEAs after the break-in process. 20 wt.% Pt/C, 40 wt.% Pt/C and 60 wt.% Pt/C catalysts are used in the cathodes of MEA 1, MEA 2 and MEA 3, respectively.

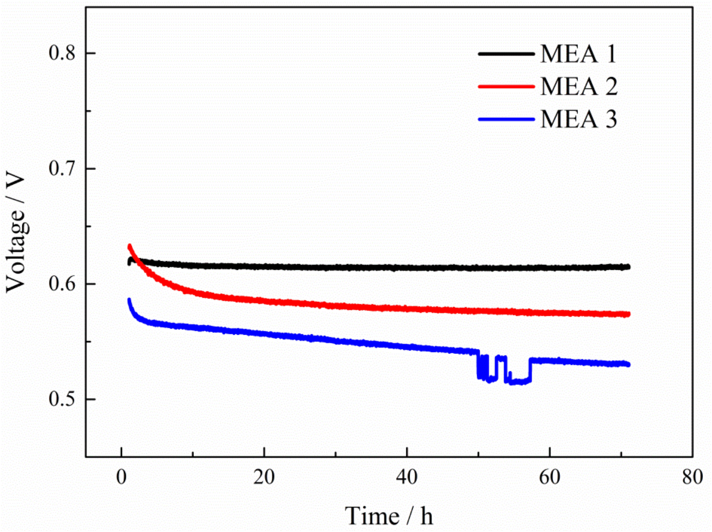

Figure 8.3: Voltage-time curves of the MEAs during the break-in procedure.

During the aging tests, the membrane degradation and PA leaching have limited impacts on the durability of HT-PEFCs, while the dominant factor is the corrosion of the Pt/C catalyst. It would seem that the catalyst degradation is inevitable due to the introduction of PA and the elevated temperatures. A good solution is to replace the PA electrolyte by non-corrosive solvents as the electrolyte in MEAs. Proton-conducting ionic liquids appear to be a suitable choice and it has become a hot topic recently, exhibiting great potential to enhance the performance as well as the durability of HT-PEFCs [161, 162].

9. Conclusion

Extensive characterizations and measurements of home-made HT-PEFCs are performed to evaluate the impacts of CCL morphologies on the electrochemical performance and to analyze and quantify the degradation behaviors under various conditions.

- The CCLs with regular cracks, more porous structures and less PTFE agglomerations show better electrochemical performance.
- The PTFE binder plays an essential role in adjusting PA distribution and maintaining the stability of the Pt/C catalyst in CCLs. According to the performance and durability tests of the HT-PEFCs, it is recommended to prepare GDEs by using 10-25 wt.% PTFE.
- In the MEA with a relatively high PA doping level, the Pt utilization efficiency can be enhanced by using the catalyst with a low Pt/C ratio and high CCL thickness.
- During the break-in process, a Pt band is visualized in the PBI-based membrane, which concretely proves the exacerbated Pt corrosion in HT-PEFCs compared to that in classic PEFCs.
- OCV is the harshest condition for HT-PEFCs; Load-cycling conditions cause moderate performance degradation. In addition, it would seem that the operating temperature does not evidently affect the HT-PEFC durability, which is mainly due to the negligible PA leaching during the 100-hour aging tests.
- The operating temperature is the most dominant factor in affecting the stability of PA in the MEA, and the thermal cycling test causes the highest amount of PA leaching.
- The cells aged under the OCV and thermal cycling conditions show the most severe membrane degradation (supported by the greatest OCV loss).
- The mechanism of Pt precipitation in the membrane is abundantly discussed. The results demonstrate that the location of a Pt band is explicitly influenced by the operating

conditions, e.g., operating load, temperature, thickness of the membrane, and PA distribution.

- The cells held at OCV and cycled at low loads exhibit the most pronounced Pt precipitation in the membrane, indicating that the high potential is the first destructive stressor for the Pt/C catalyst degradation. In addition, compared to the standard condition, load cycling and high-temperature conditions can also accelerate the Pt corrosion.

Nomenclature

Abbreviations

ACL	anode catalyst layer
At%	atom%
BET	Brunauer–Emmett–Teller
BOL	begin of life
CCL	cathode catalyst layer
CE	counter electrode
CPE	constant phase element
CV	cyclic voltammetry
ECSA	electrochemically active surface area
EDX	energy dispersive X-ray
EIS	electrochemical impedance spectroscopy
EOL	end of life
FIB	focused ion beam
GDE	gas diffusion electrode
GDL	gas diffusion layer
HT-PEFCs	high temperature-polymer electrolyte fuel cells

ICP-MS	Inductively coupled plasma-mass spectrometry
LSV	linear sweep voltammetry
MEA	membrane electrode assembly
MPL	micro porous layer
OCV	open circuit voltage
ORR	oxygen reduction reaction
PA	phosphoric acid
PADL	phosphoric acid doping level
PBI	polybenzimidazole
PEFC	polymer electrolyte fuel cell
PTFE	polytetrafluoroethylene
PVDF	polyvinylidene difluoride
RHE	reversible hydrogen electrode
SECM	scanning electrochemical microscope
SEM	scanning electrochemical microscopy
TPB	triple phase boundary
VDR	voltage degradation rate

Latin symbols

A	cm^2	surface area
b	mV per decade	Tafel slope
C	$\mathrm{mol\ mL}^{-1}$	concentration of the redox species
C_{dl}	$\mathrm{Farad\ cm}^{-2}$	cathode double layer capacitance
E	V	cell voltage
E_{rev}	V	reversible potential
F	$96485\ \mathrm{C\ mol}^{-1}$	Faraday’s constant
ΔH	$\mathrm{kJ\ mol}^{-1}$	enthalpy change of a reaction
I	A	current
j	$\mathrm{A\ cm}^{-2}$	current density
$j_{internal\ short}$	$\mathrm{A\ cm}^{-2}$	internal short current density
j_0	$\mathrm{A\ cm}^{-2}$	exchange current density
j_l	$\mathrm{A\ cm}^{-2}$	limiting crossover current density
k		Henry’s constant
K	$\mathrm{mol\ m}^{-1}\,\mathrm{s}^{-1}\,\mathrm{Pa}^{-1}$	membrane gas permeability
K_N	S^{-1}	diffusion coefficient
M_0	mg	weight of a membrane before doping
M_1	mg	weight of a membrane after doping
n		number of electrons involved in a reaction

n		exponent of a CPE
X_{H2}		molar fraction of hydrogen
X_{O2}		molar fraction of oxygen
X_{H2O}		molar fraction of water
Q	$\mathrm{C\ cm^{-2}}$	pre-factor of a CPE
Q	$\mathrm{C\ cm^{-2}}$	hydrogen desorption charge on the cathode
R_{ct}	$\Omega\ \mathrm{cm^2}$	charge transfer resistance
R_{Ω}	$\Omega\ \mathrm{cm^2}$	ohmic resistance
$R_{internal\ short}$	Ω	internal short resistance
R_m	$\Omega\ \mathrm{cm^2}$	mass transport resistance
R_p	$\Omega\ \mathrm{cm^2}$	cathode protonic resistance
R_{total}	$\Omega\ \mathrm{cm^2}$	total resistance
ΔS	$\mathrm{kJ\ mol^{-1}\ k^{-1}}$	entropy change of a reaction
T	K	operating temperature
V	V	voltage
W	$\Omega\ \mathrm{s^{-0.5}}$	Warburg impedance
Z	$\Omega\ \mathrm{cm^2}$	impedance
Z_N	$\Omega\ \mathrm{cm^2}$	diffusion impedance

Greek symbols

α		charge transfer coefficient
α_{H2O}		water activity
η_{act}	V	activation overpotential
η_{ohm}	V	ohmic overpotential
η_{conc}	V	concentration overpotential
δ_{Pt}	μm	location of a Pt band
δ_{m}	μm	thickness of a membrane
ω	rad s^{-1}	angular frequency
θ	degrees	phase angle
λ		gas stoichiometry

Bibliography

[1] C. Wannek, W. Lehnert, J. Mergel, Membrane electrode assemblies for high-temperature polymer electrolyte fuel cells based on poly (2, 5-benzimidazole) membranes with phosphoric acid impregnation via the catalyst layers, Journal of Power Sources 192 (2009) 258-266.

[2] V. Di Noto, E. Negro, J.-Y. Sanchez, C. Iojoiu, Structure-relaxation interplay of a new nanostructured membrane based on tetraethylammonium trifluoromethanesulfonate ionic liquid and neutralized nafion 117 for high-temperature fuel cells, Journal of America Chemistry Society 132 (2010) 2183-2195.

[3] C. Zhang, L. Zhang, W. Zhou, Y. Wang, S.H. Chan, Investigation of water transport and its effect on performance of high-temperature PEM fuel cells, Electrochimica Acta 149 (2014) 271-277.

[4] S.S. Araya, F. Zhou, V. Liso, S.L. Sahlin, J.R. Vang, S. Thomas, X. Gao, C. Jeppesen, S.K. Kær, A comprehensive review of PBI-based high temperature PEM fuel cells, Int. J. Hydrogen Energy 41 (2016) 21310–21344.

[5] J. Walkowiak-Kulikowska, J. Wolska, H. Koroniak, Polymers application in proton exchange membranes for fuel cells (PEMFCs), Physical Sciences Reviews 2 (2017).

[6] P. Chippar, H. Ju, Three-dimensional non-isothermal modeling of a phosphoric acid-doped polybenzimidazole (PBI) membrane fuel cell, Solid State Ionics 225 (2012) 30-39.

[7] R. He, Q. Li, J.O. Jensen, N.J. Bjerrum, Doping phosphoric acid in polybenzimidazole membranes for high temperature proton exchange membrane fuel cells, Journal of Polymer Science Part A: Polymer Chemistry 45 (2007) 2989-2997.

[8] D. Malko, T. Lopes, E. Symianakis, A. Kucernak, The intriguing poison tolerance of non-precious metal oxygen reduction reaction (ORR) catalysts, Journal of Materials Chemistry A 4 (2016) 142-152.

[9] K. Miyazaki, T. Abe, K. Nishio, H. Nakanishi, Z. Ogumi, Use of layered double hydroxides to improve the triple phase boundary in anion-exchange membrane fuel cells, Journal of Power Sources 195 (2010) 6500-6503.

[10] L. Cindrella, A.M. Kannan, J.F. Lin, K. Saminathan, Y. Ho, C.W. Lin, J. Wertz, Gas diffusion layer for proton exchange membrane fuel cells—A review, Journal of Power Sources 194 (2009) 146-160.

[11] J.T. Gostick, M.A. Ioannidis, M.W. Fowler, M.D. Pritzker, On the role of the microporous layer in PEMFC operation, Electrochemistry Communications 11 (2009) 576-579.

[12] J. Lobato, P. Cañizares, M.A. Rodrigo, D. Úbeda, F.J. Pinar, J.J. Linares, Optimisation of the Microporous Layer for a Polybenzimidazole-Based High Temperature PEMFC - Effect of Carbon Content, Fuel Cells 10 (2010) 770-777.

[13] M. Busch, M.D. Wodrich, C. Corminboeuf, Improving the Thermodynamic Profiles of Prospective Suzuki–Miyaura Cross-Coupling Catalysts by Altering the Electrophilic Coupling Component, ChemCatChem 10 (2018) 1592-1597.

[14] P. Quaino, F. Juarez, E. Santos, W. Schmickler, Volcano plots in hydrogen electrocatalysis–uses and abuses, Beilstein journal of nanotechnology 5 (2014) 846-854.

[15] J. Stacy, Y.N. Regmi, B. Leonard, M. Fan, The recent progress and future of oxygen reduction reaction catalysis: a review, Renewable and Sustainable Energy Reviews 69 (2017) 401-414.

[16] B.G. Pollet, P.M. Sakkas, Sonoelectrochemical Production of Fuel Cell Nanomaterials, in: K.I. Ozoemena, S. Chen, (Eds.), Nanomaterials for Fuel Cell Catalysis, Springer International Publishing, Cham, 2016, pp. 409-433.

[17] A. Schenk, C. Grimmer, M. Perchthaler, S. Weinberger, B. Pichler, C. Heinzl, C. Scheu, F.-A. Mautner, B. Bitschnau, V. Hacker, Platinum–cobalt catalysts for the oxygen reduction reaction in high temperature proton exchange membrane fuel cells – Long term behavior under ex-situ and in-situ conditions, Journal of Power Sources 266 (2014) 313-322.

[18] Q. Li, G. Wu, D.A. Cullen, K.L. More, N.H. Mack, H.T. Chung, P. Zelenay, Phosphate-Tolerant Oxygen Reduction Catalysts, ACS Catalysis 4 (2014) 3193-3200.

[19] J. Parrondo, F. Mijangos, B. Rambabu, Platinum/tin oxide/carbon cathode catalyst for high temperature PEM fuel cell, Journal of Power Sources 195 (2010) 3977-3983.

[20] Y.-J. Wang, D.P. Wilkinson, A. Guest, V. Neburchilov, R. Baker, F. Nan, G.A. Botton, J. Zhang, Synthesis of Pd and Nb–doped TiO2 composite supports and their corresponding Pt–Pd alloy catalysts by a two-step procedure for the oxygen reduction reaction, Journal of Power Sources 221 (2013) 232-241.

[21] S. Martin, P.L. Garcia-Ybarra, J.L. Castillo, Ten-fold reduction from the state-of-the-art platinum loading of electrodes prepared by electrospraying for high temperature proton exchange membrane fuel cells, Electrochemistry Communications 93 (2018) 57-61.

[22] C. Felix, T.-C. Jao, S. Pasupathi, B.G. Pollet, Optimisation of electrophoretic deposition parameters for gas diffusion electrodes in high temperature polymer electrolyte membrane fuel cells, Journal of Power Sources 243 (2013) 40-47.

[23] H.-Y. Du, C.-H. Wang, C.-S. Yang, H.-C. Hsu, S.-T. Chang, H.-C. Huang, S.-W. Lai, J.-C. Chen, T.L. Yu, L.-C. Chen, K.-H. Chen, A high performance polybenzimidazole–CNT hybrid electrode for high-temperature proton exchange membrane fuel cells, Journal of Materials Chemistry A 2 (2014) 7015-7019.

[24] S.-Y. Huang, P. Ganesan, S. Park, B.N. Popov, Development of a Titanium Dioxide-Supported Platinum Catalyst with Ultrahigh Stability for Polymer Electrolyte Membrane Fuel Cell Applications, Journal of the American Chemical Society 131 (2009) 13898-13899.

[25] P. Musto, F. Karasz, W. MacKnight, Fourier transform infra-red spectroscopy on the thermo-oxidative degradation of polybenzimidazole and of a polybenzimidazole/polyetherimide blend, Polymer 34 (1993) 2934-2945.

[26] F. Seland, T. Berning, B. Børresen, R. Tunold, Improving the performance of high-temperature PEM fuel cells based on PBI electrolyte, Journal of Power Sources 160 (2006) 27-36.

[27] M. Mamlouk, K. Scott, Phosphoric acid‐doped electrodes for a PBI polymer membrane fuel cell, International Journal of Energy Research 35 (2011) 507-519.

[28] M. Yusof, A. Jalil, A. Ahmad, S. Triwahyono, M. Othman, T. Abdullah, M. Firmansyah, H. Setiabudi, A. Johari, W. Nabgan, Effect of Pt–Pd/C coupled catalyst loading and polybenzimidazole ionomer binder on oxygen reduction reaction in high-temperature PEMFC, International Journal of Hydrogen Energy (2018).

[29] H. Su, S. Pasupathi, B. Bladergroen, V. Linkov, B.G. Pollet, Optimization of gas diffusion electrode for polybenzimidazole-based high temperature proton exchange membrane fuel cell: evaluation of polymer binders in catalyst layer, International Journal of Hydrogen Energy 38 (2013) 11370-11378.

[30] P. Mazúr, J. Soukup, M. Paidar, K. Bouzek, Gas diffusion electrodes for high temperature PEM-type fuel cells: role of a polymer binder and method of the catalyst layer deposition, Journal of Applied Electrochemistry 41 (2011) 1013-1019.

[31] J. Park, K. Kwon, M. Cho, S.-G. Hong, T. Kim, D. Yoo, Role of binders in high temperature PEMFC electrode, Journal of The Electrochemical Society 158 (2011) B675-B681.

[32] H. Su, S. Pasupathi, B.J. Bladergroen, V. Linkov, B.G. Pollet, Enhanced performance of polybenzimidazole-based high temperature proton exchange membrane fuel cell with gas diffusion electrodes prepared by automatic catalyst spraying under irradiation technique, Journal of Power Sources 242 (2013) 510-519.

[33] F. Mack, T. Morawietz, R. Hiesgen, D. Kramer, V. Gogel, R. Zeis, Influence of the polytetrafluoroethylene content on the performance of high-temperature polymer electrolyte membrane fuel cell electrodes, International Journal of Hydrogen Energy 41 (2016) 7475-7483.

[34] J. Lobato, P. Canizares, M. Rodrigo, C. Ruiz-López, J. Linares, Influence of the Teflon loading in the gas diffusion layer of PBI-based PEM fuel cells, Journal of Applied Electrochemistry 38 (2008) 793-802.

[35] H. Su, T.-C. Jao, S. Pasupathi, B.J. Bladergroen, V. Linkov, B.G. Pollet, A novel dual catalyst layer structured gas diffusion electrode for enhanced performance of high temperature proton exchange membrane fuel cell, Journal of Power Sources 246 (2014) 63-67.

[36] G. Jeong, M. Kim, J. Han, H.-J. Kim, Y.-G. Shul, E. Cho, High-performance membrane-electrode assembly with an optimal polytetrafluoroethylene content for high-temperature polymer electrolyte membrane fuel cells, Journal of Power Sources 323 (2016) 142-146.

[37] G.S. Avcioglu, B. Ficicilar, I. Eroglu, Effect of PTFE nanoparticles in catalyst layer with high Pt loading on PEM fuel cell performance, International Journal of Hydrogen Energy 41 (2016) 10010-10020.

[38] S. Martin, Q. Li, T. Steenberg, J.O. Jensen, Binderless electrodes for high-temperature polymer electrolyte membrane fuel cells, Journal of Power Sources 272 (2014) 559-566.

[39] D. Yao, T.-C. Jao, W. Zhang, L. Xu, L. Xing, Q. Ma, Q. Xu, H. Li, S. Pasupathi, H. Su, In-situ diagnosis on performance degradation of high temperature polymer electrolyte membrane fuel cell by examining its electrochemical properties under operation, International Journal of Hydrogen Energy 43 (2018) 21006-21016.

[40] F. Valle, N. Zuliani, B. Marmiroli, H. Amenitsch, R. Taccani, SAXS analysis of catalyst degradation in high temperature PEM fuel cells subjected to accelerated ageing tests, Fuel Cells 14 (2014) 938–944.

[41] X. Yu, S. Ye, Recent advances in activity and durability enhancement of Pt/C catalytic cathode in PEMFC: Part II: Degradation mechanism and durability enhancement of carbon supported platinum catalyst, Journal of Power Sources 172 (2007) 145-154.

[42] H.-S. Oh, J.-H. Lee, H. Kim, Electrochemical carbon corrosion in high temperature proton exchange membrane fuel cells, International Journal of Hydrogen Energy 37 (2012) 10844-10849.

[43] V. Bandlamudi, P. Bujlo, C. Sita, S. Pasupathi, Study on electrode carbon corrosion of high temperature proton exchange membrane fuel cell, Materials Today: Proceedings 5 (2018) 10602-10610.

[44] A. Chandan, M. Hattenberger, A. El-Kharouf, S. Du, A. Dhir, V. Self, B.G. Pollet, A. Ingram, W. Bujalski, High temperature (HT) polymer electrolyte membrane fuel cells (PEMFC)–A review, Journal of Power Sources 231 (2013) 264-278.

[45] Y.H. Jeong, K. Oh, S. Ahn, N.Y. Kim, A. Byeon, H.-Y. Park, S.Y. Lee, H.S. Park, S.J. Yoo, J.H. Jang, Investigation of electrolyte leaching in the performance degradation of phosphoric acid-doped polybenzimidazole membrane-based high temperature fuel cells, Journal of Power Sources 363 (2017) 365-374.

[46] S. Chevalier, M. Fazeli, F. Mack, S. Galbiati, I. Manke, A. Bazylak, R. Zeis, Role of the microporous layer in the redistribution of phosphoric acid in high temperature PEM fuel cell gas diffusion electrodes, Electrochimica Acta 212 (2016) 187-194.

[47] J. Zhang, D. Aili, J. Bradley, H. Kuang, C. Pan, R. De Marco, Q. Li, S.P. Jiang, In situ formed phosphoric acid/phosphosilicate nanoclusters in the exceptional enhancement of durability of polybenzimidazole membrane fuel cells at elevated high temperatures, Journal of The Electrochemical Society 164 (2017) F1615-F1625.

[48] M. Chandesris, R. Vincent, L. Guetaz, J.S. Roch, D. Thoby, M. Quinaud, Membrane degradation in PEM fuel cells: From experimental results to semi-empirical degradation laws, International Journal of Hydrogen Energy 42 (2017) 8139-8149.

[49] S. Mitsushima, Y. Koizumi, S. Uzuka, K.-I. Ota, Dissolution of platinum in acidic media, Electrochimica Acta 54 (2008) 455-460.

[50] R.M. Darling, J.P. Meyers, Kinetic model of platinum dissolution in PEMFCs, Journal of The Electrochemical Society 150 (2003) A1523-A1527.

[51] Y. Hashimasa, Y. Matsuda, T. Shimizu, Comparison of carbon corrosion test methods for polymer electrolyte fuel cell, Electrochimica Acta 179 (2015) 119-125.

[52] A. Ohma, S. Suga, S. Yamamoto, K. Shinohara, Membrane degradation behavior during open-circuit voltage hold test, Journal of The Electrochemical Society 154 (2007) B757-B760.

[53] T. Yoda, H. Uchida, M. Watanabe, Effects of operating potential and temperature on degradation of electrocatalyst layer for PEFCs, Electrochimica Acta 52 (2007) 5997-6005.

[54] W. Bi, G.E. Gray, T.F. Fuller, PEM fuel cell Pt／ C dissolution and deposition in nafion electrolyte, Electrochemical and Solid-State Letters 10 (2007) B101-B104.

[55] N. Macauley, L. Ghassemzadeh, C. Lim, M. Watson, J. Kolodziej, M. Lauritzen, S. Holdcroft, E. Kjeang, Pt band formation enhances the stability of fuel cell membranes, ECS Electrochemistry Letters 2 (2013) F33-F35.

[56] J. Zhang, B.A. Litteer, W. Gu, H. Liu, H.A. Gasteiger, Effect of hydrogen and oxygen partial pressure on Pt precipitation within the membrane of PEMFCs, Journal of The Electrochemical Society 154 (2007) B1006-B1011.

[57] M. Rau, A. Niedergesäß, C. Cremers, S. Alfaro, T. Steenberg, H. Hjuler, Characterization of Membrane Electrode Assemblies for High‐Temperature PEM Fuel Cells, Fuel Cells 16 (2016) 577-583.

[58] K. Hengge, C. Heinzl, M. Perchthaler, D. Varley, T. Lochner, C. Scheu, Unraveling micro-and nanoscale degradation processes during operation of high-temperature polymer-electrolyte-membrane fuel cells, Journal of Power Sources 364 (2017) 437-448.

[59] S. Liu, M. Rasinski, Y. Lin, K. Wippermann, A. Everwand, W. Lehnert, Effects of constant load operations on platinum bands formation and cathode degradation in high-temperature polymer electrolyte fuel cells, Electrochimica Acta 289 (2018) 354-362.

[60] D. Aili, L.N. Cleemann, Q. Li, J.O. Jensen, E. Christensen, N.J. Bjerrum, Thermal curing of PBI membranes for high temperature PEM fuel cells, Journal of Materials Chemistry 22 (2012) 5444-5453.

[61] C. Chen, T.F. Fuller, Modeling of H2O2 formation in PEMFCs, Electrochimica Acta 54 (2009) 3984-3995.

[62] T.H. Yu, Y. Sha, W.-G. Liu, B.V. Merinov, P. Shirvanian, W.A. Goddard III, Mechanism for degradation of Nafion in PEM fuel cells from quantum mechanics calculations, Journal of the American Chemical Society 133 (2011) 19857-19863.

[63] N. Ohguri, A.Y. Nosaka, Y. Nosaka, Detection of OH radicals as the effect of Pt particles in the membrane of polymer electrolyte fuel cells, Journal of Power Sources 195 (2010) 4647-4652.

[64] Y. Oono, A. Sounai, M. Hori, Long-term cell degradation mechanism in high-temperature proton exchange membrane fuel cells, Journal of Power Sources 210 (2012) 366-373.

[65] T. Søndergaard, L.N. Cleemann, H. Becker, D. Aili, T. Steenberg, H.A. Hjuler, L. Seerup, Q. Li, J.O. Jensen, Long-term durability of HT-PEM fuel cells based on thermally cross-linked polybenzimidazole, Journal of Power Sources 342 (2017) 570-578.

[66] J. Halter, S. Thomas, S.K. Kær, T.J. Schmidt, F.N. Büchi, The influence of phosphoric acid migration on the performance of high temperature polymer electrolyte fuel cells, Journal of Power Sources 399 (2018) 151-156.

[67] C.-Y. Chen, W.-H. Lai, Effects of temperature and humidity on the cell performance and resistance of a phosphoric acid doped polybenzimidazole fuel cell, Journal of Power Sources 195 (2010) 7152-7159.

[68] S. Galbiati, A. Baricci, A. Casalegno, R. Marchesi, Degradation in phosphoric acid doped polymer fuel cells: A 6000 h parametric investigation, International Journal of Hydrogen Energy 38 (2013) 6469-6480.

[69] N. Pilinski, M. Rastedt, P. Wagner, Investigation of Phosphoric Acid Distribution in PBI Based HT-PEM Fuel Cells, ECS Transactions 69 (2015) 323-335.

[70] S. Thomas, C. Jeppesen, T. Steenberg, S.S. Araya, J.R. Vang, S.K. Kær, New load cycling strategy for enhanced durability of high temperature proton exchange membrane fuel cell, International Journal of Hydrogen Energy 42 (2017) 27230-27240.

[71] J.A. Kerres, Blended and Cross-Linked Ionomer Membranes for Application in Membrane Fuel Cells, Fuel Cells 5 (2005) 230-247.

[72] S. Yu, L. Xiao, B. Benicewicz, Durability studies of PBI‐based high temperature PEMFCs, Fuel Cells 8 (2008) 165-174.

[73] A. Modestov, M. Tarasevich, V.Y. Filimonov, N. Zagudaeva, Degradation of high temperature MEA with PBI-H3PO4 membrane in a life test, Electrochimica Acta 54 (2009) 7121-7127.

[74] M. Zhao, W. Shi, B. Wu, W. Liu, J. Liu, D. Xing, Y. Yao, Z. Hou, P. Ming, Z. Zou, Influence of Membrane Thickness on Membrane Degradation and Platinum Agglomeration under Long-term Open Circuit Voltage Conditions, Electrochimica Acta 153 (2015) 254-262.

[75] H. Su, H. Liang, B.J. Bladergroen, V. Linkov, B.G. Pollet, S. Pasupathi, Effect of platinum distribution in dual catalyst layer structured gas diffusion electrode on the performance of high temperature PEMFC, Journal of The Electrochemical Society 161 (2014) F506-F512.

[76] M. Gasik, Materials for fuel cells, Elsevier, 2008.

[77] S.H. Frensch, A.C. Olesen, S.S. Araya, S.K. Kær, Model-supported characterization of a PEM water electrolysis cell for the effect of compression, Electrochimica Acta 263 (2018) 228-236.

[78] A. Unnikrishnan, N. Rajalakshmi, V.M. Janardhanan, Kinetics of electrochemical charge transfer in HT-PEM fuel cells, Electrochimica Acta 293 (2019) 128-140.

[79] S. Didierjean, O. Lottin, G. Maranzana, T. Geneston, PEM fuel cell voltage transient response to a thermal perturbation, Electrochimica Acta 53 (2008) 7313-7320.

[80] U. Reimer, W. Lehnert, Y. Holade, B. Kokoh, Irreversible losses in fuel cells, Fuel Cells and Hydrogen, Elsevier, 2018, pp. 15-40.

[81] H. Liang, H. Su, B.G. Pollet, V. Linkov, S. Pasupathi, Membrane electrode assembly with enhanced platinum utilization for high temperature proton exchange membrane fuel cell prepared by catalyst coating membrane method, Journal of Power Sources 266 (2014) 107-113.

[82] S. Liu, Y. Rahim, K. Wippermann, H. Janßen, W. Lehnert, D. Stolten, Study of Cathode Catalyst Layer Parameters for HT-PEMFC Using Electrochemical Impedance Spectroscopy, ECS Transactions 80 (2017) 27-36.

[83] B. Winther-Jensen, D.R. MacFarlane, New generation, metal-free electrocatalysts for fuel cells, solar cells and water splitting, Energy & Environmental Science 4 (2011) 2790-2798.

[84] F. Barbir, PEM fuel cells, Fuel Cell Technology, Springer, 2006, pp. 27-51.

[85] X.-Z.R. Yuan, C. Song, H. Wang, J. Zhang, Electrochemical impedance spectroscopy in PEM fuel cells: fundamentals and applications, Springer Science & Business Media, 2009.

[86] M.A. Danzer, E.P. Hofer, Analysis of the electrochemical behaviour of polymer electrolyte fuel cells using simple impedance models, Journal of Power Sources 190 (2009) 25-33.

[87] M.R. Shoar Abouzari, F. Berkemeier, G. Schmitz, D. Wilmer, On the physical interpretation of constant phase elements, Solid State Ionics 180 (2009) 922-927.

[88] R. Taccani, T. Chinese, M. Boaro, Effect of accelerated ageing tests on PBI HTPEM fuel cells performance degradation, International Journal of Hydrogen Energy 42 (2017) 1875-1883.

[89] R. Alipour Moghadam Esfahani, R.B. Moghaddam, I.I. Ebralidze, E.B. Easton, A hydrothermal approach to access active and durable sulfonated silica-ceramic carbon electrodes for PEM fuel cell applications, Applied Catalysis B: Environmental 239 (2018) 125-132.

[90] S. Kaserer, K.M. Caldwell, D.E. Ramaker, C. Roth, Analyzing the Influence of H3PO4 as Catalyst Poison in High Temperature PEM Fuel Cells Using in-operando X-ray Absorption Spectroscopy, The Journal of Physical Chemistry C 117 (2013) 6210-6217.

[91] Q. He, X. Yang, W. Chen, S. Mukerjee, B. Koel, S. Chen, Influence of phosphate anion adsorption on the kinetics of oxygen electroreduction on low index Pt(hkl) single crystals, Physical Chemistry Chemical Physics 12 (2010) 12544-12555.

[92] Y. Zhou, H. Zhang, L. Liu, C. Li, Z. Chang, X. Zhu, B. Ye, M. Xu, Fabrication of an antibody-aptamer sandwich assay for electrochemical evaluation of levels of β-amyloid oligomers, Scientific reports 6 (2016) 35186.

[93] P. Dhanasekaran, S. Vinod Selvaganesh, A. Shukla, N. Nagaraju, S.D. Bhat, Boosting Pt oxygen reduction reaction activity and durability by carbon semi-coated titania nanorods for proton exchange membrane fuel cells, Electrochimica Acta 263 (2018) 596-609.

[94] S. Wasterlain, D. Candusso, F. Harel, D. Hissel, X. François, Development of new test instruments and protocols for the diagnostic of fuel cell stacks, Journal of Power Sources 196 (2011) 5325-5333.

[95] G. Tjarks, A. Gibelhaus, F. Lanzerath, M. Müller, A. Bardow, D. Stolten, Energetically-optimal PEM electrolyzer pressure in power-to-gas plants, Applied Energy 218 (2018) 192-198.

[96] J.L. Jespersen, E. Schaltz, S.K. Kær, Electrochemical characterization of a polybenzimidazole-based high temperature proton exchange membrane unit cell, Journal of Power Sources 191 (2009) 289-296.

[97] W. Schulte, S. Liu, I. Plettenberg, S. Kuhri, W. Lüke, W. Lehnert, G. Wittstock, Local Evaluation of Processed Membrane Electrode Assemblies by Scanning Electrochemical Microscopy, Journal of The Electrochemical Society 164 (2017) F873-F878.

[98] A. Lesch, D. Momotenko, F. Cortés-Salazar, F. Roelfs, H.H. Girault, G. Wittstock, High-throughput scanning electrochemical microscopy brushing of strongly tilted and curved surfaces, Electrochimica Acta 110 (2013) 30-41.

[99] K. Cooper, M. Smith, Electrical test methods for on-line fuel cell ohmic resistance measurement, Journal of Power Sources 160 (2006) 1088-1095.

[100] M. Kim, C. Kim, Y. Sohn, Application of Metal Foam as a Flow Field for PEM Fuel Cell Stack, Fuel Cells 18 (2018) 123-128.

[101] H. Yang, Y. Tang, S. Zou, Electrochemical removal of surfactants from Pt nanocubes, Electrochemistry Communications 38 (2014) 134-137.

[102] X. Cheng, B. Yi, M. Han, J. Zhang, Y. Qiao, J. Yu, Investigation of platinum utilization and morphology in catalyst layer of polymer electrolyte fuel cells, Journal of Power Sources 79 (1999) 75-81.

[103] R. Friedmann, T. Van Nguyen, Optimization of the microstructure of the cathode catalyst layer of a PEMFC for two-phase flow, Journal of The Electrochemical Society 157 (2010) B260-B265.

[104] J. Lee, J. Jung, J.Y. Han, H.-J. Kim, J.H. Jang, H.-J. Lee, E.A. Cho, D. Henkensmeier, J.Y. Kim, S.J. Yoo, Effect of membrane electrode assembly fabrication method on the single cell performances of polybenzimidazole-based high temperature polymer electrolyte membrane fuel cells, Macromolecular Research 22 (2014) 1214-1220.

[105] K. Wippermann, C. Wannek, H.-F. Oetjen, J. Mergel, W. Lehnert, Cell resistances of poly (2, 5-benzimidazole)-based high temperature polymer membrane fuel cell membrane electrode assemblies: time dependence and influence of operating parameters, Journal of Power Sources 195 (2010) 2806-2809.

[106] A. Atifi, H. Mounir, A. El Marjani, Effect of internal current, fuel crossover, and membrane thickness on a PEMFC performance, 2014 International Renewable and Sustainable Energy Conference (IRSEC), IEEE, 2014, pp. 907-912.

[107] G. Liu, H. Zhang, J. Hu, Y. Zhai, D. Xu, Z.-g. Shao, Studies of performance degradation of a high temperature PEMFC based on H3PO4-doped PBI, Journal of Power Sources 162 (2006) 547-552.

[108] U. Reimer, B. Schumacher, W. Lehnert, Accelerated degradation of high-temperature polymer electrolyte fuel cells: discussion and empirical modeling, Journal of The Electrochemical Society 162 (2015) F153-F164.

[109] J. Lobato, H. Zamora, J. Plaza, P. Cañizares, M.A. Rodrigo, Enhancement of high temperature PEMFC stability using catalysts based on Pt supported on SiC based materials, Applied Catalysis B: Environmental 198 (2016) 516-524.

[110] M. Kim, G. Jeong, K. Eom, E. Cho, J. Ryu, H.-J. Kim, H. Kwon, Effects of heat treatment time on electrochemical properties and electrode structure of polytetrafluoroethylene-bonded membrane electrode assemblies for polybenzimidazole-based high-temperature proton exchange membrane fuel cells, International Journal of Hydrogen Energy 38 (2013) 12335-12342.

[111] S. Zhang, X.-Z. Yuan, J.N.C. Hin, H. Wang, J. Wu, K.A. Friedrich, M. Schulze, Effects of open-circuit operation on membrane and catalyst layer degradation in proton exchange membrane fuel cells, Journal of Power Sources 195 (2010) 1142-1148.

[112] S. Sugawara, T. Maruyama, Y. Nagahara, S.S. Kocha, K. Shinohra, K. Tsujita, S. Mitsushima, K.-i. Ota, Performance decay of proton-exchange membrane fuel cells under

open circuit conditions induced by membrane decomposition, Journal of Power Sources 187 (2009) 324-331.

[113] M. Tenci, S. Rossi, M.C. Bonferoni, G. Sandri, I. Mentori, C. Boselli, A.I. Cornaglia, M. Daglia, A. Marchese, C. Caramella, Application of DoE approach in the development of mini-capsules, based on biopolymers and manuka honey polar fraction, as powder formulation for the treatment of skin ulcers, International journal of pharmaceutics 516 (2017) 266-277.

[114] J.R. Corpas-Martínez, A. Pérez, C. Amor-Castillo, R. Navarro-Domínguez, M. Martín-Lara, M. Calero, Optimal Depressants and Collector Dosage in Fluorite Flotation Process Based on DoE Methodology, Applied Sciences 9 (2019) 366.

[115] Y. Rahim, H. Janßen, W. Lehnert, Characterizing membrane electrode assemblies for high temperature polymer electrolyte membrane fuel cells using design of experiments, International Journal of Hydrogen Energy 42 (2017) 1189-1202.

[116] D.v.B.K. Siebertz, T. Hochkirchen, D. van Bebber, Statistische versuchsplanung, Springer, 2010.

[117] S. Martin, Q. Li, J.O. Jensen, Lowering the platinum loading of high temperature polymer electrolyte membrane fuel cells with acid doped polybenzimidazole membranes, Journal of Power Sources 293 (2015) 51-56.

[118] J.-P. Melchior, K.-D. Kreuer, J. Maier, Proton conduction mechanisms in the phosphoric acid–water system (H 4 P 2 O 7–H 3 PO 4· 2H 2 O): a 1 H, 31 P and 17 O PFG-NMR and conductivity study, Physical Chemistry Chemical Physics 19 (2017) 587-600.

[119] L. Vilčiauskas, M.E. Tuckerman, G. Bester, S.J. Paddison, K.-D. Kreuer, The mechanism of proton conduction in phosphoric acid, Nature chemistry 4 (2012) 461.

[120] J. Zhao, A. Manthiram, In Situ Electrochemical Characterization of Proton Exchange Membrane Fuel Cells Fabricated with Pd–Pt–Ni Cathode Catalysts, Journal of The Electrochemical Society 158 (2011) B208-B214.

[121] J.-R. Kim, S.Y. Jung, T.-W. Song, Investigation of degradation mechanisms of a high-temperature polymer-electrolyte-membrane fuel cell stack by electrochemical impedance spectroscopy, Journal of Power Sources 220 (2012) 54-64.

[122] S.V. Venkatesan, M. Dutta, E. Kjeang, Mesoscopic degradation effects of voltage cycled cathode catalyst layers in polymer electrolyte fuel cells, Electrochemistry Communications 72 (2016) 15-18.

[123] M.F. Mathias, R. Makharia, H.A. Gasteiger, J.J. Conley, T.J. Fuller, C.J. Gittleman, S.S. Kocha, D.P. Miller, C.K. Mittelsteadt, T. Xie, S.G. Van, P.T. Yu, Two fuel cell cars in every garage?, Electrochemical Society Interface 14 (2005) 24-35.

[124] S. Abbou, J. Dillet, G. Maranzana, S. Didierjean, O. Lottin, Local potential evolutions during proton exchange membrane fuel cell operation with dead-ended anode–Part II: Aging mitigation strategies based on water management and nitrogen crossover, Journal of Power Sources 340 (2017) 419-427.

[125] L. Gubler, S.M. Dockheer, W.H. Koppenol, Radical (HO•, H• and HOO•) formation and ionomer degradation in polymer electrolyte fuel cells, Journal of The Electrochemical Society 158 (2011) B755-B769.

[126] H. Tang, S. Peikang, S.P. Jiang, F. Wang, M. Pan, A degradation study of Nafion proton exchange membrane of PEM fuel cells, Journal of Power Sources 170 (2007) 85-92.

[127] J. Aragane, H. Urushibata, T. Murahashi, Effect of operational potential on performance decay rate in a phosphoric acid fuel cell, Journal of Applied Electrochemistry 26 (1996) 147-152.

[128] J. Lobato, P. Canizares, M.A. Rodrigo, J.J. Linares, PBI-based polymer electrolyte membranes fuel cells: temperature effects on cell performance and catalyst stability, Electrochimica Acta 52 (2007) 3910-3920.

[129] S. Wasterlain, D. Candusso, D. Hissel, F. Harel, P. Bergman, P. Menard, M. Anwar, Study of temperature, air dew point temperature and reactant flow effects on proton

exchange membrane fuel cell performances using electrochemical spectroscopy and voltammetry techniques, Journal of Power Sources 195 (2010) 984-993.

[130] V. Ramani, H.R. Kunz, J.M. Fenton, Stabilized heteropolyacid/Nafion® composite membranes for elevated temperature/low relative humidity PEFC operation, Electrochimica Acta 50 (2005) 1181-1187.

[131] B.T. Huang, Y. Chatillon, C. Bonnet, F. Lapicque, S. Leclerc, M. Hinaje, S. Raël, Experimental investigation of pinhole effect on MEA/cell aging in PEMFC, International Journal of Hydrogen Energy 38 (2013) 543-550.

[132] K. Strickland, R. Pavlicek, E. Miner, Q. Jia, I. Zoller, S. Ghoshal, W. Liang, S. Mukerjee, Anion Resistant Oxygen Reduction Electrocatalyst in Phosphoric Acid Fuel Cell, ACS Catalysis 8 (2018) 3833–3843.

[133] M. Prokop, T. Bystron, M. Paidar, K. Bouzek, H3PO3 electrochemical behaviour on a bulk Pt electrode: adsorption and oxidation kinetics, Electrochimica Acta 212 (2016) 465-472.

[134] M. Prokop, T. Bystron, K. Bouzek, Electrochemistry of Phosphorous and Hypophosphorous Acid on a Pt electrode, Electrochimica Acta 160 (2015) 214-218.

[135] H. Su, T.-C. Jao, O. Barron, B.G. Pollet, S. Pasupathi, Low platinum loading for high temperature proton exchange membrane fuel cell developed by ultrasonic spray coating technique, Journal of Power Sources 267 (2014) 155-159.

[136] C. Wannek, B. Kohnen, H.F. Oetjen, H. Lippert, J. Mergel, Durability of ABPBI - based MEAs for High Temperature PEMFCs at Different Operating Conditions, Fuel Cells 8 (2008) 87–95.

[137] S. Liu, M. Rasinski, Y. Rahim, S. Zhang, K. Wippermann, U. Reimer, W. Lehnert, Influence of operating conditions on the degradation mechanism in high-temperature polymer electrolyte fuel cells, Journal of Power Sources 439 (2019) 227090.

[138] C. Zhang, W. Zhou, M.M. Ehteshami, Y. Wang, S.H. Chan, Determination of the optimal operating temperature range for high temperature PEM fuel cell considering its performance, CO tolerance and degradation, Energy conversion and management 105 (2015) 433-441.

[139] T. Søndergaard, L.N. Cleemann, H. Becker, T. Steenberg, H.A. Hjuler, L. Seerup, Q. Li, J.O. Jensen, Long-term durability of PBI-based HT-PEM fuel cells: effect of operating parameters, Journal of The Electrochemical Society 165 (2018) F3053-F3062.

[140] C.A. Reiser, L. Bregoli, T.W. Patterson, S.Y. Jung, J.D. Yang, M.L. Perry, T.D. Jarvi, A reverse-current decay mechanism for fuel cells, Electrochemical and Solid-State Letters 8 (2005) A273-A276.

[141] W. Maier, T. Arlt, C. Wannek, I. Manke, H. Riesemeier, P. Krüger, J. Scholta, W. Lehnert, J. Banhart, D. Stolten, In-situ synchrotron X-ray radiography on high temperature polymer electrolyte fuel cells, Electrochemistry Communications 12 (2010) 1436-1438.

[142] Q. Li, J.O. Jensen, R.F. Savinell, N.J. Bjerrum, High temperature proton exchange membranes based on polybenzimidazoles for fuel cells, Progress in polymer science 34 (2009) 449-477.

[143] D. Ramaker, A. Korovina, V. Croze, J. Melke, C. Roth, Following ORR intermediates adsorbed on a Pt cathode catalyst during break-in of a PEM fuel cell by in operando X-ray absorption spectroscopy, Physical Chemistry Chemical Physics 16 (2014) 13645-13653.

[144] M. Zhao, W. Shi, B. Wu, W. Liu, J. Liu, D. Xing, Y. Yao, Z. Hou, P. Ming, J. Gu, Z. Zou, Analysis of carbon-supported platinum through potential cycling and potential-static holding, International Journal of Hydrogen Energy 39 (2014) 13725-13737.

[145] S. Eberhardt, T. Lochner, F. Büchi, T.J. Schmidt, Correlating electrolyte inventory and lifetime of HT-PEFC by accelerated stress testing, Journal of The Electrochemical Society 162 (2015) F1367-F1372.

[146] D. Schonvogel, M. Rastedt, P. Wagner, M. Wark, A. Dyck, Impact of accelerated stress tests on high temperature PEMFC degradation, Fuel Cells 16 (2016) 480–489.

[147] F.J. Pinar, P. Cañizares, M.A. Rodrigo, D. Úbeda, J. Lobato, Long-term testing of a high-temperature proton exchange membrane fuel cell short stack operated with improved polybenzimidazole-based composite membranes, Journal of Power Sources 274 (2015) 177-185.

[148] M. Haque, A.B. Sulong, E. Majlan, K. Loh, T. Husaini, R. Rosli, Physiochemical Characteristics of Solid Electrolyte Membranes for High-Temperature PEM Fuel Cell, International Journal of Electrochemical Science 14 (2019) 371-386.

[149] D.-T. Chin, H.H. Chang, On the conductivity of phosphoric acid electrolyte, Journal of Applied Electrochemistry 19 (1989) 95-99.

[150] F. Liu, Interaction of phosphoric acid with cell components in high temperature polymer electrolyte fuel cells, Elektrochemische Verfahrenstechnik, 2014.

[151] Z. Qi, S. Buelte, Effect of open circuit voltage on performance and degradation of high temperature PBI–H3PO4 fuel cells, Journal of Power Sources 161 (2006) 1126-1132.

[152] S. Eberhardt, M. Toulec, F. Marone, M. Stampanoni, F. Büchi, T.J. Schmidt, Dynamic operation of HT-PEFC: in-operando imaging of phosphoric acid profiles and (re) distribution, Journal of The Electrochemical Society 162 (2015) F310-F316.

[153] R. O’Hayre, D.M. Barnett, F.B. Prinz, The triple phase boundary a mathematical model and experimental investigations for fuel cells, Journal of The Electrochemical Society 152 (2005) A439-A444.

[154] F. Liu, S. Mohajeri, Y. Di, K. Wippermann, W. Lehnert, Influence of the Interaction Between Phosphoric Acid and Catalyst Layers on the Properties of HT‐PEFCs, Fuel Cells 14 (2014) 750-757.

[155] L.-Z. Fan, S. Qiao, W. Song, M. Wu, X. He, X. Qu, Effects of the functional groups on the electrochemical properties of ordered porous carbon for supercapacitors, Electrochimica Acta 105 (2013) 299-304.

[156] R. Shimizu, J. Tsuji, N. Sato, J. Takano, S. Itami, M. Kusakabe, K. Miyatake, A. Iiyama, M. Uchida, Durability and degradation analysis of hydrocarbon ionomer membranes in polymer electrolyte fuel cells accelerated stress evaluation, Journal of Power Sources 367 (2017) 63-71.

[157] S. Kundu, M. Fowler, L.C. Simon, R. Abouatallah, Reversible and irreversible degradation in fuel cells during open circuit voltage durability testing, Journal of Power Sources 182 (2008) 254-258.

[158] D. Stolten, B. Emonts, Fuel Cell Science and Engineering, 2 Volume Set: Materials, Processes, Systems and Technology, John Wiley & Sons, 2012.

[159] W. Maier, Phosphorsäureverteilung in Membran-Elektroden-Einheiten dynamisch betriebener Hochtemperatur-Polymerelektrolyt-Brennstoffzellen, Forschungszentrum Jülich, Zentralbibliothek, 2012.

[160] M. Khaneft, O. Holderer, O. Ivanova, W. Lüke, E. Kentzinger, M. Appavou, R. Zorn, W. Lehnert, Structure and Proton Dynamics in Catalytic Layer of HT‐PEFC, Fuel Cells 16 (2016) 406-413.

[161] S. Maity, S. Singha, T. Jana, Low acid leaching PEM for fuel cell based on polybenzimidazole nanocomposites with protic ionic liquid modified silica, Polymer 66 (2015) 76-85.

[162] K. Wippermann, J. Wackerl, W. Lehnert, B. Huber, C. Korte, 2-Sulfoethylammonium trifluoromethanesulfonate as an ionic liquid for high temperature PEM fuel cells, Journal of The Electrochemical Society 163 (2016) F25-F37.

List of Figures

List of Tables

Publications

[1] **S. Liu**, M. Rasinski, Y. Rahim, S. Zhang, K. Wippermann, U. Reimer, W. Lehnert, Influence of operating conditions on the degradation mechanism in high-temperature polymer electrolyte fuel cells, Journal of Power Sources 439 (2019) 227090.

[2] **S. Liu**, M. Rasinski, Y. Lin, K. Wippermann, A. Everwand, W. Lehnert, Effects of constant load operations on platinum bands formation and cathode degradation in high-temperature polymer electrolyte fuel cells, Electrochimica Acta 289 (2018) 354-362.

[3] **S. Liu**, Y. Rahim, K. Wippermann, H. Janßen, W. Lehnert, D. Stolten, Study of Cathode Catalyst Layer Parameters for HT-PEMFC Using Electrochemical Impedance Spectroscopy, ECS Transactions 80 (2017) 27-36.

[4] M. Khaneft, **S. Liu**, Y. Lin, H. Janßen, W. Lüke, R. Zorn, O. Ivanova, A. Radulescu, O. Holderer, W. Lehnert, Proton dynamics of phosphoric acid in HT-PEFCs: Towards "operando" experiments, AIP Conference Proceedings, AIP Publishing, 2018, pp. 030003.

[5] W. Schulte, **S. Liu**, I. Plettenberg, S. Kuhri, W. Lüke, W. Lehnert, G. Wittstock, Local Evaluation of Processed Membrane Electrode Assemblies by Scanning Electrochemical Microscopy, Journal of The Electrochemical Society 164 (2017) F873-F878.

[6] O. Holderer, M. Khaneft, Y. Lin, **S. Liu**, A. Feoktystov, M. Kruteva, R. Zorn, W. Lehnert, Nanostructure of HT-PEFC Electrodes Investigated with Scattering Methods, ECS Transactions 80 (2017) 19-25.

Acknowledgments

Good time always goes very fast and the four-year doctoral study has come to an end. During the busy study process, I have a lot of pleasant recollections of the time I spent with my wonderful friends and colleagues. Also, I have ever encountered many difficulties. But with the help of them, I overcome the difficulties and finally finish my dissertation.

First of all, I would like to thank my supervisor Prof. Lehnert. Thank you for giving me a chance to work at Forschungszentrum Juelich and for providing me with a great working environment. I still remember at the beginning of my doctoral study, the experiment progress was not very smooth, since I did not adapt well to the research environment. Instead of giving me pressure, Prof. Lehnert patiently guided me and kindly helped me out of difficulties. Under the supervision of Prof. Lehnert, I continue to make progress and achieve several valuable experimental results. More importantly, I complete writing my PhD dissertation and become a PhD candidate. Thank you for everything you have done for my doctoral study.

Secondly, I want to appreciate the colleagues who give me helps during the study process. I want to say thank you to Dr. Klaus Wippermann, Dr. Uwe Reimer, Dr. Holger Janßen, Ms. Birgit Schumacher and Mr. Andreas Everwand. They give me a number of help when I have problems during the research process. Their patience and profound knowledge are admirable, which benefit a lot for my dissertation as well as my future career.

I am very grateful to the colleagues who cooperate with me in the work. Dr. Yasser Rahim, Dr. Marcin Rasinski, Dr. Yu Lin, Mr. Shidong Zhang, Dr. Marina Khaneft and Dr. Olaf Holderer leave me tons of good memories together. What is more, Dr. Michael Höh, Dr. Qing Cao, Dr. Junliang Yu, Dr. Yulin Yan, Dr. Diankai Qiu, Prof. Xu, Prof. Ni, Dr. Jürgen Giffin, Katja Klafki, Christopher Wood, Daniel Holtz, Ruiyu Li, Yun Cai, Philipp Irmscher, Olha Panchenko, Yuan

Wang, Yan Shi, Wei Zou, Eugen Hoppe, Jingjing Lin, Chang Liu, Yanpeng Suo, Lei Wu and Javier Jaime Solis Leon give me numerous help and suggestions for my work and life. I want to express my deepest thanks to all the outstanding colleagues working at IEK-3.

Also, I would like to appreciate the China Scholarship Council (CSC) for the financial support during my four-year PhD study (grant number 201506890023).

Finally, I want to thank my parents, my wife and my son for their help in my daily life and mental supports at different stages of the PhD study, which is essential for me to finally complete the dissertation.

Band / Volume 465
IEK-3 Report 2019
Maßgeschneiderte Energieumwandlung für nachhaltige Kraftstoffe
D. Stolten, B. Emonts (Eds.) (2019), 171 pp
ISBN: 978-3-95806-410-2

Band / Volume 466
Initialinfrastruktur für Wasserstoffmobilität auf Basis von Flotten
F. Grüger (2019), V, 209 pp
ISBN: 978-3-95806-413-3

Band / Volume 467
Techno-ökonomische Analyse alternativer Wasserstoffinfrastruktur
M. E. Reuß (2019), 205 pp
ISBN: 978-3-95806-414-0

Band / Volume 468
Study on a miniaturized satellite payload
for atmospheric temperature measurements
J. Liu (2019), 153 pp
ISBN: 978-3-95806-415-7

Band / Volume 469
Partitioning Water Vapor Fluxes by the Use of Their Water Stable Isotopologues: From the Lab to the Field
M. E. Quade (2019), XVI, 113 pp
ISBN: 978-3-95806-417-1

Band / Volume 470
Entwicklung von Reparaturmethoden für Nickel-Superlegierungen mittels thermischer Spritzverfahren
T. Kalfhaus (2019), VI, 126, XXX pp
ISBN: 978-3-95806-418-8

Band / Volume 471
Entwicklung von korrosionsstabilen Schutzschichten für oxidische Faserverbundwerkstoffe
C. S. Gatzen (2019), II, 143 pp
ISBN: 978-3-95806-422-5

Band / Volume 472
Coatings for Metallic Bipolar Plates in High-Temperature
Polymer Electrolyte Fuel Cells
R. Li (2019), II, 119 pp
ISBN: 978-3-95806-425-6

Schriften des Forschungszentrums Jülich
Reihe Energie & Umwelt / Energy & Environment

Band / Volume 473
Thermochemische Eigenschaften von kombinierten Katalysator- und Sauerstoffträgersystemen für die partielle Oxidation von Teeren aus der Biomassevergasung
M. Ma (2019), VII, 157 pp
ISBN: 978-3-95806-426-3

Band / Volume 474
Einfluss der klimatischen Fertigungsumgebung auf die Mechanik und Rissstrukturierung der elektrodenbeschichteten Membran einer PEM-Brennstoffzelle
B. Wienk-Borgert (2019), IV, 141 pp
ISBN: 978-3-95806-428-7

Band / Volume 475
Reversible wasserstoffbetriebene Festoxidzellensysteme
M. H. Frank (2019), 187 pp
ISBN: 978-3-95806-430-0

Band / Volume 476
Partitioning of carbon dioxide exchange
in rapidly and slowly changing ecosystems
P. Ney (2019), xvi, 95 pp
ISBN: 978-3-95806-431-7

Band / Volume 477
Massentransportphänomene in Schichtsystemen eines Elektrolyseurs
U. Panchenko (2019), 107 pp
ISBN: 978-3-95806-433-1

Band / Volume 478
Mechanische Eigenschaften von Polymer-Elektrolyt-Membran-Brennstoffzellen
P. Irmscher (2019), vii, 177 pp
ISBN: 978-3-95806-435-5

Band / Volume 479
Morphology and Degradation of High Temperature
Polymer Electrolyte Fuel Cell Electrodes
S. Liu (2019), III, 162 pp
ISBN: 978-3-95806-436-2

Weitere ***Schriften des Verlags im Forschungszentrum Jülich*** unter
http://wwwzb1.fz-juelich.de/verlagextern1/index.asp

Energie & Umwelt / Energy & Environment
Band / Volume 479
ISBN 978-3-95806-436-2

Mitglied der Helmholtz-Gemeinschaft

JÜLICH
Forschungszentrum